2009

This is to certify that the
thesis entitled

MASS SPECTROMETRIC CHARACTERIZATION OF ZINC ACTIVATED PROINSULIN C-PEPTIDE AND C-PEPTIDE MUTANTS

presented by

ZACHARY KELTNER

has been accepted towards fulfillment
of the requirements for the

M.S. degree in Chemistry

Major Professor's Signature

January 22nd, 2009

Date

MASS SPECTROMETRIC CHARACTERIZATION OF ZINC ACTIVATED PROINSULIN C-PEPTIDE AND C-PEPTIDE MUTANTS

By

Zachary Keltner

A THESIS

Submitted to
Michigan State University
in partial fulfillment of the requirements
for the degree of

MASTER OF SCIENCE

Chemistry

2009

ABSTRACT

MASS SPECTROMETRIC CHARACTERIZATION OF ZINC ACTIVATED PROINSULIN C-PEPTIDE AND C-PEPTIDE MUTANTS

By

Zachary Keltner

Proinsulin C-peptide has recently been demonstrated to ameliorate some chronic complications caused by diabetes. Recent experiments have shown that this activity is dependent upon activation with certain metals, such as Fe(II), Cr(III) or Zn(II). In an effort to gain a greater understanding of the peptide-metal interactions responsible for this activity, "top-down" tandem mass spectrometry characterization of proinsulin C-peptide and various C-peptide mutants in the presence or absence of Zn^{2+} was carried out. Gas-phase fragmentation of various protonated precursor ion charge states of C-peptide, as well as Zn-activated C-peptide, yielded extensive sequence coverage. These results indicate multiple sites for Zn binding, making it difficult to localize the Zn to a specific residue within the peptide sequence. However, certain product ions indicated a likely role for acidic residues in Zn binding. Five single-amino acid C-peptide mutants were synthesized, by substitution of each acidic residue with alanine. These mutants did not significantly affect the fragmentation behavior for either the unbound or Zn bound precursor ions, suggesting that any one acidic residue is not critical for binding. However, a 50% decrease in the relative Zn binding for the mutants was observed compared to the wild type sequence. Additional studies on a C-terminal pentapeptide sequence EGSLQ, as well as an alanine substituted mutant, AGSLQ, were also performed. Substitution of the Glu residue in this peptide was found to affect both the binding and activity, implicating a role for the Glu27 residue.

ACKNOWLEDGMENTS

Throughout the time I have spent compiling my research, several people have helped and supported me. Without them, this would not have been possible. I would first like to acknowledge my research advisor, Dr. Gavin Reid. His guidance and support was invaluable to my development as a scientist. He has been there from day one, and has always provided much needed direction. I would like to thank the members of my committee, Dr. Gary Blanchard, Dr. David Weliky, and Dr. Daniel Jones for their help and guidance. I would also like to thank Ms. Jennifer Meyer and Dr. Dana Spence for their help in conducting the ATP release experiments, as well as for providing sound advice when it was needed most. Mr. Matt Ruiz has been an invaluable resource for his assistance in acquiring MALDI spectra. In addition, I would like to thank the other members of my research group, namely Ms. Amanda Palumbo and Dr. Jennifer Cox for helping me throughout my time here and listening to my questions, all while becoming good friends along the way. My friends outside of the Chemistry program have served as a great support system to me through the entire process. Finally, I would like to acknowledge my family who has been a great asset in this and everything in my life. Their patience in helping me deal with my frustration and stress throughout my graduate career is much appreciated.

TABLE OF CONTENTS

LIST OF TABLES vi

LIST OF FIGURES vii

1. CHAPTER ONE: A Biological Role for Proinsulin C-peptide? 1
   - 1.1 Diabetes Mellitus and its Complications 1
   - 1.2 Insulin and its Roles in Diabetes 2
   - 1.3 Proinsulin C-peptide 5
   - 1.4 Metals and their Roles in Diabetes 10
   - 1.5 Metal-Activated C-peptide 13
   - 1.6 Metal-Binding Analysis by Mass Spectrometry 17
   - 1.7 Aims of This Thesis 20

2. CHAPTER TWO: Strategies for the Synthesis and Characterization of Proinsulin C-peptide, its Mutants, and Metal-Binding 21
   - 2.1 Solid-Phase Peptide Synthesis (SPPS) of the C-peptide Mutants 21
     - 2.1.1 Materials 21
     - 2.1.2 Synthesis 22
       - 2.1.2.1 Deprotection 23
       - 2.1.2.2 Coupling 23
       - 2.1.2.3 Ninhydrin Test 23
       - 2.1.2.4 Final Deprotection/Cleavage 24
       - 2.1.2.5 Workup/Extraction 25
   - 2.2 High Performance Liquid Chromatography (HPLC) for the Purification of C-peptide and its Mutants 25
   - 2.3 Mass Spectrometry for the Analysis of Peptides and Proteins 27
     - 2.3.1 Introduction 27
     - 2.3.2 Ionization Sources 27
       - 2.3.2.1 Electrospray Ionization (ESI) 28
       - 2.3.2.2 Matrix-Assisted Laser Desorption-Ionization (MALDI) 30
     - 2.3.3 Mass analyzers 31
       - 2.3.3.1 Quadrupole Mass Analyzer 32
       - 2.3.3.2 Quadrupole Ion Trap 37
       - 2.3.3.3 Tandem Mass Spectrometry 44
       - 2.3.3.4 Linear Ion Trap (LIT) 45
     - 2.3.4 Peptide Fragmentation Nomenclature 47
     - 2.3.5 Instrumentation 48
       - 2.3.4.1 MALDI-LIT analysis 48
       - 2.3.4.2 ESI-LIT analysis 49

3. CHAPTER THREE: Characterization of Proinsulin C-peptide, its Mutants, and Binding with Zn^{2+} 51
3.1 Top-down Characterization of Proinsulin C-peptide 51
3.1.1 Bottom-up and Top-down Proteomics 51
3.1.2 Characterization of Proinsulin C-peptide 53
3.2 Characterization of Proinsulin C-peptide Bound to Zn^{2+} 60
3.3 Top-down Characterization of the Proinsulin C-peptide Mutants 67
3.4 Characterization of the Zn^{2+}-bound C-peptide Mutants 70
3.5 Effect of Amino Acid Mutation on the Relative Binding of Zn^{2+} to C-Peptide 78
3.6 Characterization and Activity Studes of the C-terminal Pentapeptide of C-peptide 81
3.7 Conclusions and Future Directions 88

SUPPORTING INFORMATION 89

REFERENCES 130

LIST OF TABLES

TABLE **PAGE**

2.1 Sequences of the single amino acid mutants of C-peptide that were synthesized, along with their respective abbreviations. Locations of the alanine substitutions are labeled in bold and underlined on the sequences.....22

2.2 HPLC gradient used for the purification of proinsulin C-peptide mutants 26

LIST OF FIGURES

FIGURE **PAGE**

1.1 Structure of proinsulin, showing locations of cleavage into insulin and C-peptide. Sequences of the A) A-chain, B) B-chain and C) C-peptide are shown below the structure. 3

1.2 Sequence homology of C-peptide for 20 mammalian species. The sequence of human C-peptide is given in the top line, and upper-case letters below represent sequence conservation in more than one species, while lower-case letters represent conservation in one species. Letters in boxes indicate conservation in all or all but one species, while dashes represent gaps in the sequence. 6

2.1 Representation of droplet formation in ESI. 29

2.2 Schematic of a quadrupole mass spectrometer, showing applied AC potential (Φ_0) 33

2.3 Stability diagram for a quadrupole mass analyzer. 37

2.4 Schematic of a quadrupole ion trap 38

2.5 Mathieu stability diagram for a 3D ion trap showing stability of ions of different m/z values. Larger balls indicate larger m/z values 40

2.6 Diagram of Dehmelt pseudopotential well in a 3D ion trap. E_{RE} is the energy where resonance ejection typically is carried out. 42

2.7 Nomenclature for peptide fragmentation. 48

3.1 ESI mass spectrum of 10 μM proinsulin C-peptide in water. 54

3.2 CID MS/MS spectrum of the $[M+2H^+]^{2+}$ charge state (m/z = 1543.3) of C-peptide from Figure 3.1. 58

3.3 Product ion and sequence coverage summaries obtained from the CID spectra of the A) $[M+H^+]^+$, B) $[M+2H^+]^{2+}$, C) $[M+3H^+]^{3+}$, D) $[M+4H^+]^{4+}$, and E) combined product ion and sequence coverage summary for all charge states observed for C-peptide. The $[M+H^+]^+$ were acquired using MALDI while all others were acquired using ESI. Ions with a relative abundance greater than 25% are labeled on the summary. 59

3.4 A) Mass spectrum of 10 μM C-peptide and 10 μM $ZnCl_2$ B) High resolution UltraZoom scan of the $[M+H^{+}+Zn^{2+}]^{3+}$ charge state C) High resolution UltraZoom scan of the $[M+Zn^{2+}]^{2+}$ charge state. 61

3.5 CID MS/MS Spectrum of the $[M+Zn^{2+}]^{2+}$ charge state (m/z = 1542.7) of C-peptide from Figure 4A. Ions observed to have Zn bound are labeled with † in bold.. 65

3.6 Product ion and sequence coverage summaries obtained from the CID spectra of the A) $[M+Zn^{2+}]^{2+}$, B) $[M+Zn^{2+}+H^{+}]^{3+}$, C) $[M+Zn^{2+}+2H^{+}]^{4}$ charge states of C-peptide as well as D) the overall product ion and sequence coverage summary. ╲ indicates an unbound b or y ion, ╲ indicates only the Zn-bound fragment was found, and ╲ indicates that both bound and unbound ions were identified.. 66

3.7 CID MS/MS Spectrum of the $[M+2H^{+}]^{2+}$ charge state (m/z = 1482.6) of E27A.... 68

3.8 Product ion and sequence coverage summaries obtained from the CID spectra of the $[M+2H^{+}]^{2+}$ charge state of A) E27A, B) E11A, C) D4A, D) E3A, and E) E1A mutants of C-peptide. Ions with relative abundance greater than 25% are labelled on the summary. 69

3.9 ESI mass spectra of 10 μM $ZnCl_2$ and 10 μM A) E27A, B) E11A, C) D4A in H_2O 73

3.10 ESI mass spectra of 10 μM $ZnCl_2$ and 10 μM A) E3A, B) E1A in H_2O 74

3.11 CID MS/MS Spectrum of the $[M+Zn^{2+}]^{2+}$ charge state (m/z = 1514.44) of the E27A mutant of C-peptide from Figure 9A. 75

3.12 Product ion and sequence coverage summaries obtained from the CID spectra of the A) $[M+Zn^{2+}]^{2+}$, B) $[M+Zn^{2+}+H^{+}]^{3+}$, C) $[M+Zn^{2+}+2H^{+}]^{4}$ charge states of E27A as well as D) the overall product ion and sequence coverage summary. ╲ indicates an unbound b or y ion, ╲ indicates only the Zn-bound fragment was found, and ╲ indicates that both bound and unbound ions were identified. 76

3.13 Product ion and sequence coverage summaries obtained from the CID spectra of the $[M+Zn^{2+}]^{2+}$ charge state of A) E27A, B) E11A, C) D4A, D) E3A, and E) E1A mutants of C-peptide. ╲ indicates an unbound b or y ion,

\ indicates only the Zn-bound fragment was found, and \\ indicates that both bound and unbound ions were identified.. 77

3.14 Plot showing binding ratios of the $[M+Zn^{2+}+nH^{+}]^{(n+2)+}$ to $[M+nH]^{n+}$ for C-peptide and the 5 mutants A) Accounting for $[M+Na]^{+}$ $[M+K]^{+}$ adducts and B) not accounting for the salt adducts. Intensities for the 2+, 3+, and 4+ charge states were summed. Standard deviations for the triplicate measurements are shown on the plot. 80

3.15 ESI mass spectra for 10 μM Zn^{2+} and 10 μM A) EGSLQ and B) AGSLQ.. 82

3.16 CID-MS/MS spectra of the $[M+Zn^{2+}]^{2+}$ precursor ions of A) EGSLQ and B) AGSLQ....86

3.17 Bar graph showing normalized ATP release in erythrocytes for C-peptide as well as the EGSLQ pentapeptide and the AGSLQ mutant. Measurements were taken with n = 7, and error bars are plotted as the standard error of the mean. A * indicates a statistically significant difference was calculated using a single sided students t-test (p = 0.025). 87

S1 MALDI CID MS/MS Spectrum of the $[M+H^{+}]^{+}$ charge state (m/z = 3021.3) of C-peptide....90

S2 CID MS/MS Spectrum of the $[M+3H^{+}]^{3+}$ charge state (m/z = 1007.6) of C-peptide 91

S3 CID MS/MS Spectrum of the $[M+4H^{+}]^{4+}$ charge state (m/z = 756.0) of C-peptide. 92

S4 CID MS/MS Spectrum of the $[M+Zn^{2+}+H^{+}]^{3+}$ charge state (m/z = 1007.6) of C-peptide. 93

S5 CID MS/MS Spectrum of the $[M+2H^{+}+Zn^{2}]^{4+}$ charge state (m/z = 772.0) of C-peptide. 94

S6 MALDI CID MS/MS Spectrum of the $[M+H^{+}]^{+}$ charge state (m/z = 2962.3) of E27A 95

S7 CID MS/MS Spectrum of the $[M+3H^{+}]^{3+}$ charge state (m/z = 988.6) of E27A....96

S8 CID MS/MS Spectrum of the $[M+4H^+]^{4+}$ charge state (m/z = 741.5) of E27A.....97

S9 MALDI CID MS/MS Spectrum of the $[M+H^+]^+$ charge state (m/z = 2962.5) of E11A. 98

S10 CID MS/MS Spectrum of the $[M+2H^+]^{2+}$ charge state (m/z = 1482.6) of E11A.....99

S11 CID MS/MS Spectrum of the $[M+3H^+]^{3+}$ charge state (m/z = 988.6) of E11A.....100

S12 CID MS/MS Spectrum of the $[M+4H^+]^{4+}$ charge state (m/z = 741.5) of E11A.....101

S13 MALDI CID MS/MS Spectrum of the $[M+H^+]^+$ charge state (m/z = 2976) of D4A 102

S14 CID MS/MS Spectrum of the $[M+2H^+]^{2+}$ charge state (m/z = 1489.5) of D4A. 103

S15 CID MS/MS Spectrum of the $[M+3H^+]^{3+}$ charge state (m/z = 993.5) of D4A. 104

S16 CID MS/MS Spectrum of the $[M+4H^+]^{4+}$ charge state (m/z = 745.5) of D4A. 105

S17 MALDI CID MS/MS Spectrum of the $[M+H^+]^+$ charge state (m/z = 2962.3) of E3A 106

S18 CID MS/MS Spectrum of the $[M+2H^+]^{2+}$ charge state (m/z = 1488.5) of E3A.....107

S19 CID MS/MS Spectrum of the $[M+3H^+]^{3+}$ charge state (m/z = 988.5) of E3A ...108

S20 CID MS/MS Spectrum of the $[M+4H^+]^{4+}$ charge state (m/z = 741.6) of E3A ...109

S21 MALDI CID MS/MS Spectrum of the $[M+H^+]^+$ charge state (m/z = 2962.4) of E1A. 110

S22 CID MS/MS Spectrum of the $[M+2H^+]^{2+}$ charge state (m/z = 1488.5) of E1A.....111

S23 CID MS/MS Spectrum of the $[M+3H^+]^{3+}$ charge state (m/z = 988.5) of E1A.....112

S24 CID MS/MS Spectrum of the $[M+4H^+]^{4+}$ charge state (m/z = 741.5) of E1A.....113

S25 Overall product ion and sequence coverage summaries of the $[M+H^+]^+$, $[M+2H^+]^{2+}$, $[M+3H^+]^{3+}$, and $[M+4H^+]^{4+}$ charge states of the A)E27A, B) E11A, C) D4A, D) E3A, and E) E1A mutants of C-peptide.....114

S26 CID MS/MS Spectrum of the $[M+Zn^{2+}+H^+]^{3+}$ charge state (m/z = 1008.9) of E27A. 115

S27 CID MS/MS Spectrum of the $[M+Zn^{2+}+2H^+]^{4+}$ charge state (m/z = 758.0) of E27A 116

S28 CID MS/MS Spectrum of the $[M+Zn^{2+}]^{2+}$ charge state (m/z = 1514.4) of E11A.....117

S29 CID MS/MS Spectrum of the $[M+H^++Zn^{2+}]^{3+}$ charge state (m/z = 1008.9) of E11A 118

S30 CID MS/MS Spectrum of the $[M+2H^++Zn^{2+}]^{4+}$ charge state (m/z = 758.0) of E11A. 119

S31 CID MS/MS Spectrum of the $[M+Zn^{2+}]^{2+}$ charge state (m/z = 1521.6) of D4A. 120

S32 CID MS/MS Spectrum of the $[M+H^++Zn^{2+}]^{3+}$ charge state (m/z = 1014.0) of D4A. 121

S33 CID MS/MS Spectrum of the $[M+2H^++Zn^{2+}]^{4+}$ charge state (m/z = 760.7) of D4A. 122

S34 CID MS/MS Spectrum of the $[M+Zn^{2+}]^{2+}$ charge state (m/z = 1513.6) of E3A.....123

S35 CID MS/MS Spectrum of the $[M+H^{+}+Zn^{2+}]^{3+}$ charge state (m/z = 1008.9) of E3A. 124

S36 CID MS/MS Spectrum of the $[M+2H^{+}+Zn^{2+}]^{4+}$ charge state (m/z = 757.0) of E3A. 125

S37 CID MS/MS Spectrum of the $[M+Zn^{2+}]^{2+}$ charge state (m/z = 1513.38) of E1A. 126

S38 CID MS/MS Spectrum of the $[M+H^{+}+Zn^{2+}]^{3+}$ charge state (m/z = 1009.9) of E1A 127

S39 CID MS/MS Spectrum of the $[M+2H^{+}+Zn^{2+}]^{4+}$ charge state (m/z = 757.8) of E1A 128

S40 Overall product ion and sequence coverage summaries obtained from the CID spectra of the $[M+Zn^{2+}]^{2+}$, $[M+H^{+}+Zn^{2+}]^{3+}$, and $[M+2H^{+}+Zn^{2+}]^{4+}$ charge states of A) E11A, B) D4A, C) E3A, D) E1A, mutants of C-peptide. \ indicates an unbound b or y ion, \ indicates only the Zn-bound fragment was found, and \ indicates that both bound and unbound ions were identified 129

CHAPTER ONE

A biological role for proinsulin C-peptide?

1.1 Diabetes Mellitus and Diabetic Complications

Diabetes mellitus is a disease that affects an estimated 180 million people worldwide, with this number projected to double by the year 2030 (World Health Organization). In 2005, an estimated 1.1 million deaths were reported from this disease. Diabetes is characterized by deregulation of glucose in the body causing hyperglycemia, i.e., elevated blood glucose levels, due to either a lack of insulin production in the β-cells of the pancreas or a bodily resistance to the insulin being produced. Diabetes is generally classified based on the means by which hyperglycemia is caused.

Type 1 diabetes, also called juvenile diabetes or insulin-dependent diabetes, is characterized by a lack of insulin production due to auto-immune destruction of the β-cells. This type of diabetes can become fatal but is managed by regular insulin injections. Type 2 diabetes, also called adult-onset diabetes, results from an inability of the body to effectively use the insulin that is produced. This form of diabetes is largely diagnosed in middle-aged adults, but recently has been also found in overweight children. Key factors associated with the onset of type 2 diabetes are obesity and lack of exercise. This form of diabetes may largely be managed by diet and exercise. The third category of diabetes is gestational diabetes which is characterized by hyperglycemia similar to type 2 diabetes during pregnancy. This form usually ends after pregnancy.

Although the disease may be managed using the methods stated above, there is no cure for diabetes. Additionally, many chronic complications may arise even with proper treatment. Elevated blood glucose levels lead to glycation of lipids and proteins by an irreversible Amadori reaction, leading to advanced glycation endproducts (AGEs). It has been shown that type 2 diabetic patients exhibit elevated levels of AGEs,[1] which act to deregulate normal enzyme functions. These AGEs are also a key source of free radicals which act to increase oxidative stress in diabetic patients.[2]

Macrovascular complications, including heart disease and stroke, are another serious category of complications associated with diabetes. In fact, it has been estimated that 50% of diabetic patients die of cardiovascular diseases (World Health Organization). Hypertension, caused by a constriction of the blood vessels which leads to high blood pressure, can lead to many of these complications.

Diabetic patients are also subject to several microvascular complications, which can result in vision disorders (retinopathy), kidney failure (nephropathy) and nerve damage (neuropathy). Diabetic retinopathy is the leading cause of blindness in adults, and affects 80% of long term (>20 years) diabetic patients. Diabetic nephropathy is one of the leading causes of kidney failure, and an estimated 10-20 % of diabetic patients die of kidney failure. Nerve damage due to neuropathy is caused by lack of blood flow to the extremities, which results in a high rate of foot amputations among diabetic patients.

1.2 Insulin and its Role in Diabetes

Proinsulin is a prohormone that is produced in the β-cells of the Islets of Langerhans in the pancreas. Its structure has been well-defined[3], and it consists of 3

subunits, the A and B chains of insulin, and C-peptide, which connects the A and B chains. The structure and sequence of human proinsulin is shown in Figure 1.1. Once produced, disulfide bonds between the A and B chains of insulin are formed, which locks the structure of insulin into place. Proinsulin is then cleaved by two different proteases to form C-peptide and insulin in equimolar amounts.

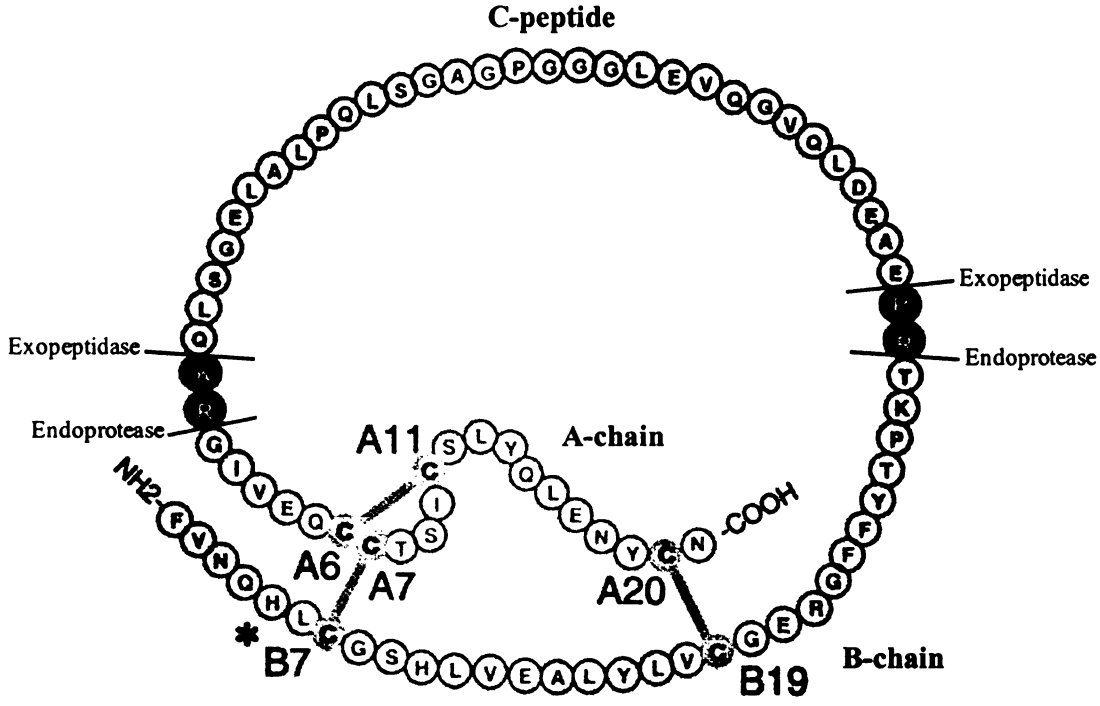

A G I V D Q C C T S S I C S L Y Q L E N Y C E
B F V E Q H L C G S H L V N A L Y L V S G N R G F F Y T P K T
C E A E D L Q V G Q V E L G G G P G A G S L Q P L A L E G S L Q

Figure 1.1: Structure of proinsulin, showing locations of cleavage into insulin and c-peptide. Sequences of the A) A-chain, B) B-chain and C) C-peptide are shown below the structure. (Adapted and modified from Reference 4)

One protease behaves as an endoprotease and cleaves at the basic residues on each end of the C-peptide sequence, and another acts as an exopeptidase to remove the basic residues

at the ends of the peptide. The cleavage sites of the proteases are also shown in Figure 1.1. Once insulin is formed, it is stored in secretory vesicles. Upon an increase in glucose concentration, insulin is released from the β-cells through ATP dependant K^+ channel and Ca^{2+} channels. Upon release of Ca^{2+}, insulin is released from the secretory vesicles into the blood stream.

Insulin's main function is to aid in the transport of plasma glucose into cells, where it is then used as fuel when needed, or stored as glycogen. This acts to regulate the concentration of glucose in the blood stream when glucose levels are high. Glucose transport operates mainly through 2 glucose transporters, GLUT1 and GLUT4.[5] GLUT1 is a ubiquitous carrier that is located in erythrocytes and endothelial cells. It is a large transmembrane protein that transports glucose and other molecules such as Vitamin C by undergoing conformational changes.[6] GLUT4 is an insulin-sensitive transporter found in muscle and adipose tissue, and is located in intracellular vesicles. Insulin binds to the insulin receptor on the muscle or fat cells, which translocates the GLUT4 transporter to the cell membrane, where glucose is then transported inside the cell. Once in the cell, glucose is phosphorylated to glucose-6-phosphate where it undergoes glycolysis.[7]

In type 1 diabetes, the absence of β-cells does not allow for the production of insulin, such that glucose transport is inhibited. Type 2 patients suffer from insulin resistance, where the produced insulin is not used effectively, causing the β-cells to produce even more insulin in response to increased blood glucose levels.

Along with glucose transport, insulin has also been shown to play a role in endothelium-derived nitric oxide (NO) production.[8] NO is produced by endothelial nitric

oxide synthase (eNOS) in response to increased blood flow and has been shown to promote vasodilation within cells. Insulin has been shown to play a role in the activation of eNOS, resulting in an increased production of NO, via phosphorylation at the Ser1179 residue of eNOS.[9] Under hyperglycemic conditions, where insulin is either not present or not effective, NO production is hindered not allowing the endothelial cells to respond to an increase in the shear stress within the cells. Both type 1 and type 2 diabetic patients have been shown to have decreased availability of NO,[10] causing complications such as hypertension and atherosclerosis.

1.3 Proinsulin C-peptide

While the effects and mechanisms of insulin on diabetes are fairly well-understood, recent attention has shifted towards the other by-product of proinsulin cleavage, i.e., C-peptide. As mentioned above, C-peptide is a variable-length peptide that bridges the A and B-chains of insulin. Since its sequencing in 1971,[11] it has been thought to aid only the correct folding of insulin, and have no biological activity.[12] Because it is secreted in equimolar amounts along with insulin, detection of C-peptide has been used as a diagnostic marker for diabetes.[13] Evidence supporting a lack of activity for C-peptide has been provided by the lack of primary structure conservation among different species, while both the A and B chains of insulin are highly conserved.[14] A summary of the sequence homology of C-peptide from 20 mammalian species, is shown in Figure 1.2. The human C-peptide sequence is listed at the top, while variable

amino acids are listed below. Capitalized letters represent sequence variants observed in more than one species, while lower-case letters represent sequence variants observed in only a single species. Letters in boxes indicate conservation in all, or all but one, of the mammalian species. Dashes indicate possible gaps in the sequences.

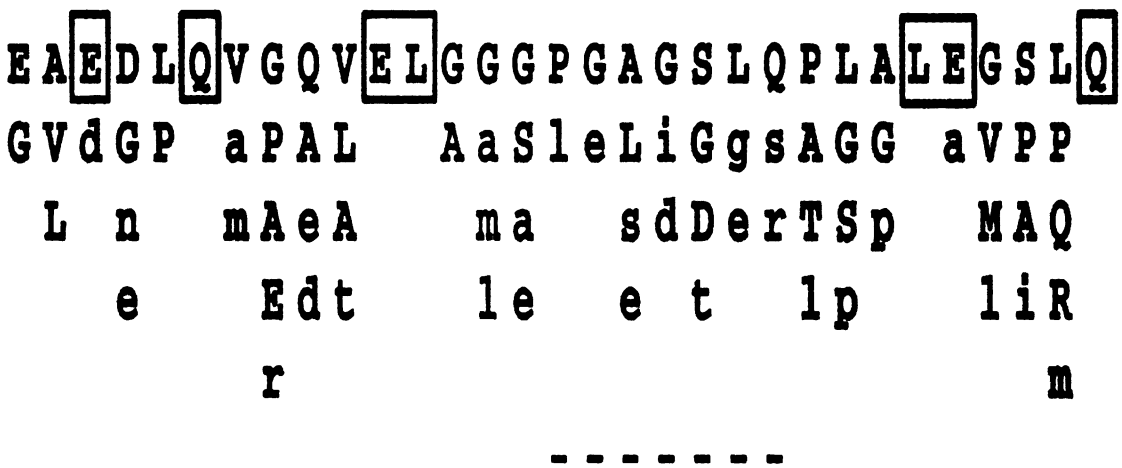

Figure 1.2: Sequence homology of C-peptide from 20 mammalian species. (Adapted and modified from reference 14)

It can be seen from Figure 1.2 that very few amino acids are conserved, while deletions are present in the internal segments of some species. It has also been demonstrated that human C-peptide lacks any secondary structure under physiological conditions or in lipid environments,[15] further supporting the contention that C-peptide plays no biological role in diabetes.

Despite the lack of sequence conservation and secondary structure, recent experiments have shown that C-peptide exerts favorable effects among patients with type 1 diabetes. *In vivo* experiments have shown that administration of C-peptide can improve red blood cell deformability,[16] renal and nerve function,[17-21] as well as improve

microvascular blood flow.[22, 23] Other *in vitro* studies have shown that C-peptide can activate mitogen-activated protein kinases (MAPK)[24, 25] as well as stimulate eNOS.[22] As mentioned before, eNOS plays a key role in chronic diabetic complications such as hypertension. C-peptide has also been observed to specifically bind G protein-coupled receptors on human cell membranes[26], demonstrating a basis for the activity of C-peptide.

While it has been shown that C-peptide has the ability to bind to cell membranes, the fate of the bound peptide was not known. Recently, an experiment conducted by Lindhal *et. al.*[27] using labeled C-peptide demonstrated that C-peptide is internalized within the cytosol of mouse fibroblast cells as well as human embryonic kidney cells. This study gives yet more evidence to the biological activity of C-peptide, giving evidence for intracellular activity.

C-peptide appears to be an unusual case of a peptide which lacks sequence conservation yet exhibits biological activity. When looking at the C-peptide sequences for various species, only 7 residues are highly conserved across mammalian species.[14] These residues mainly consist of Glu and Gln residues, and cover both the N-terminal and C-terminal regions of the peptide. This may suggest some significance to these residues. Thus, several studies have been conducted to relate structural elements of C-peptide to specific biological activities.[14, 18, 24-26, 28-31] These experiments have resulted in conflicting viewpoints about which part of the peptide is active. One experiment studied different segments of rat C-peptide and their ability to stimulate Na^+,

K^+-ATPase activity.[30] Na^+, K^+-ATPase is involved in the regulation of Na^+ and K^+ transport into and out of skeletal cells, and is the cause of some muscular dysfunctions in diabetic patients.[32] This study found that the C-terminal portion of the peptide was active, with the fragments EVARQ (residues 27-31) and VARQ residues (28-31) showing 103% and 92% activity over the full length peptide, respectively. The remaining N-terminal portion of the peptide sequence only showed 2% activity, while segments in the middle showed between 3 and 80% activity, with the section consisting of residues 11-19 returning the most activity.

Another study examined the regions of human C-peptide and its ability to displace human membrane-bound full length C-peptide.[31] This study found that the C-terminal pentapeptide (EGSLQ) could fully displace the membrane bound peptide, while the C-terminal tetrapeptide (GLSQ) had no effect on the displacement. Free Glu showed about 50% displacement, while the pentapeptide EVARQ corresponding to the pentapeptide of rat C-peptide was not able to displace human C-peptide. The middle segment (residues 11-19) which showed some activity in rat C-peptide showed no activity for the human case. The results from this study led to a suggestion that the Glu27 residue is key in receptor binding,[31] which is also consistent with the previous experiment showing that the C-terminal pentapeptide is crucial to Na^+,K^+-ATPase activity.[31]

A conflicting study conducted by Ido *et. al.* [18] examined albumin permeation upon addition of insulin and C-peptide. Increased albumin permeation among diabetic patients leads to vascular dysfunction. It was found that albumin permeation decreased

60-70% in the aorta, uvea, retina and nerves upon administration of both C-peptide and insulin. It was also found that administration of retro C-peptide (i.e., a reversed sequence) retained almost full activity, as did rat C-peptide. However, a scrambled full-length C-peptide was found to be inactive, suggesting that the sequence, but not direction of the amino acids is critical. C-peptide fragments were also analyzed, and it was found that fragments containing the N-terminal residues of the peptide were critical for activity, while the C-terminal region was not necessary. This result is in stark contrast to the previous results described above that showed the C-terminal pentapeptide was the active region of the peptide.

Secondary structure analysis was also conducted on human C-peptide by Henriksson *et. al.*[14] which demonstrated that secondary structure can be induced in C-peptide upon addition of a high concentration (80%) of 2,2,2-trifluoroethanol (TFE), though the peptide retains no secondary structure in aqueous solution. Circular dichroism (CD) was used to identify the secondary structure present. In these experiments it was found that the N-terminal portion of the peptide (residues 1-11) formed an α-helical structure. The propensity for helical formation further increased when a tetra-alanine mutant (D4A/V7A/G8A/V10A) was examined. Activity was also demonstrated using MAPK phosphorylation, and it was found that substitution of the 3 highly conserved glutamic acid residues with alanine resulted in a dramatic decrease in the MAPK phosphorylation. It was also demonstrated that inducing structure in the peptide also increased MAPK phosphorylation, which increased further with the tetra-alanine mutant, suggesting that secondary structure is crucial to its activity. Note that while secondary

structure may be induced in C-peptide, the extremely high concentrations of TFE required are far from physiological conditions.

Other conflicting secondary structure analyses using molecular dynamics[33] and CD[18] have shown that the C-terminal region of the peptide exists as a turn-like structure upon addition of high concentrations of TFE. These studies, compared to the previous experiment discussed above,[14] also indicate differing percentages of α-helical formation in the N-terminal region of the peptide. The middle segment of the peptide has been shown to adopt hairpin secondary structure upon addition of TFE. However, consistent with previous reports, C-peptide adopted no secondary structure under physiological conditions.

From these studies, it can be seen that C-peptide can have several beneficial effects on the chronic complications caused by diabetes. However, no clear relationship has been drawn between the structure of C-peptide and its biological function. Although several reports show that the C-terminus of the peptide is the active region, other conflicting studies show that the N-terminus or middle segments of the peptide can be active for certain experiments.

1.4 Metals and their Roles in Diabetes

Metals and regulation of their levels in the body plays a crucial role in many bodily processes.[34] One of the most important roles that metals play is to regulate the levels of reactive oxygen species which increase oxidative stress. As mentioned before advanced glycation endproducts are one cause of oxidative stress among diabetic

patients, which has been shown to decrease insulin secretion levels as well as being a factor in increased insulin resistance. A variety of metals may act as antioxidants; however iron, chromium and zinc have proven to be very important.[34] Although their effects are well known, including in diabetes, the mechanisms by which these effects occur has not yet been fully characterized for some of these metals.

Iron is a metal whose effects on the body have been well established. An increase in the absorption of iron by the body, called hemochromatosis, has been implicated in diabetes.[35] It was found that diabetes developed in 63% of patients who had hemochromatosis. Furthermore, 22% of these patients developed diabetic complications such as nephropathy and neuropathy, as well as retinopathy.[35]

The mechanism by which diabetes caused by iron overload occurs is not yet understood. However, studies have been conducted to demonstrate that treatment with chelation or blood donation results in increased insulin sensitivity and insulin secretion.[36] Iron has also been linked to cardiovascular disease, a key complication of diabetes. Diabetic patients exhibiting high iron levels have been shown to have an increased risk of developing cardiovascular disease.[37] Again, some of the cardiovascular ailments may be relieved through Fe^{2+} chelation or blood donation.

Chromium is another essential element whose commercial use has been extensively promoted as being beneficial to diabetes. As mentioned above, diabetic patients exhibit decreased glucose uptake into cells either because of lack of insulin

production or resistance to insulin. Experiments on rats have shown stimulation of glucose uptake upon addition of Cr^{3+}.[38]

In experiments performed by Schwarz and co-workers in the 1950s, it was found that rats fed with a certain diet consisting of chromium-deficient Torula yeast developed impaired glucose tolerance in response to exogenous glucose.[39] This led to the discovery of a new compound termed the glucose tolerance factor, which aided in proper glucose metabolism. The structure of this factor has not been defined, but it has been determined that Cr^{3+} is essential to its function.[40]

When investigating the mechanism by which chromium plays a role in diabetes, the existence of a small chromium-binding molecule, termed chromodulin, was reported in the 1980's.[41] Chromodulin is a peptide consisting of only four types of amino acids, namely glycine, cysteine, glutamic acid and aspartic acid, with a molecular weight of 1500 Da.[42] Chromodulin has the ability to bind up to four Cr^{3+} ions, even though it has such a small molecular weight. Its mechanism has been investigated, and it is believed to play a role in increasing the efficacy of the conversion of glucose to carbon dioxide or lipid in rat adipocyte cells.[38, 43] This process is essential to cellular respiration. Chromodulin has also been shown to be active in the processes of signal transduction, as well as insulin signaling.

Zinc is another important metal whose link to diabetes and insulin has been long established. It has been shown that Zn^{2+} exists in the β-cells along with proinsulin in millimolar concentrations. Once proinsulin is cleaved to form mature insulin and C-

peptide, the mature insulin exists as a hexamer which is bound to two Zn^{2+} ions.[44] Zn^{2+} enters the secretory vesicle through a transmembrane protein called ZnT-8,[45] where it binds and forms the insulin hexamer. The vesicles then reach the membrane of the β-cell, where insulin, C-peptide, and Zn^{2+} are all released.

Along with the conformational role played by Zn^{2+} in the organization of the insulin hexamer, it has also been found that patients with diabetes exhibit elevated levels of Zn in urine,[46] indicating that the Zn is not being used properly within the secretory vesicles. Destruction of β-cells in type 1 diabetes results in a lack of Zn to perform other functions, such as reducing oxidative stress. As mentioned before, oxidative stress is a key problem associated with tissue damage in diabetic patients.

Metals play a key role in the development and progression of diabetes and diabetic complications. As shown above, metals such as Zn are in high concentrations in the pancreas where insulin is produced and secreted, and other metals such as chromium have shown to interact with insulin and facilitate glucose metabolism. As C-peptide is secreted along with insulin, it would be reasonable to hypothesize that C-peptide could have an ability to interact with these metals, which may help explain some of the inconsistencies obtained from the C-peptide experiments.

1.5 Metal-Activated C-peptide

Recently, Meyer *et. al.*[47] demonstrated that human C-peptide has the ability to release ATP from rabbit erythrocytes. ATP is a known stimulant of endothelium-derived

nitric oxide, and it has been shown that erythrocytes have the ability to release ATP in response to different stimuli. It has also been shown that diabetic erythrocytes release 50% ATP with respect to non-diabetic erythrocytes. It was shown that ATP release was increased three-fold over a period of 8 hours when C-peptide was added to a sample of erythrocytes. From these results, it was also demonstrated that upon addition of C-peptide, ATP levels in human patients with type 2 diabetes could be restored to those observed in healthy control patients.

It was observed however, that the increased ATP release was time dependent. After 25-36 hours following preparation of C-peptide in water, ATP release was dramatically decreased to baseline levels compared to erythrocyte controls. Following analysis of the C-peptide sample using electrospray ionization (ESI) mass spectrometry, it was observed that the peptide was intact and no degradation products were found. However, in a freshly prepared solution of C-peptide, adducts formed with Fe^{2+}, as well as K^{+} and Na^{+}, were observed. Solutions of HPLC purified C-peptide and water were then spiked with Fe^{2+} solutions and it was found that a major Fe^{2+} adduct was formed, indicating a preferential binding of C-peptide to Fe^{2+}.

ATP release experiments revealed that upon addition of fresh solutions of Fe^{2+} to solutions of C-peptide, ATP release was increased. As a control, a peptide solution which had been stored for 30 days was incubated with erythrocytes and demonstrated no activity. C-peptide purified by HPLC also showed not activity. Solutions of Fe^{2+} were then added to previously inactive C-peptide samples, and the activity was restored. The

effect of the oxidation state of iron was studied by incubating the erythrocytes with samples of C-peptide and Fe^{3+}, which displayed no increase in ATP release. These samples were subjected to ESI-MS analysis where it was found that minimal Fe^{3+} adduct was formed. It was determined that upon exchange of Fe^{2+} with ions such as Na^{+} and K^{+} in solution over time, or oxidation of Fe^{2+} to Fe^{3+}, the ATP release was observed to decrease. Thus, the increase in ATP release was due to the presence of an Fe^{2+} 'activated' C-peptide.

To determine whether other metals could 'activate' C-peptide with respect to an increase in ATP release from erythrocytes, the effect of Cr^{3+} was also examined by Meyer *et. al.* Following addition of Cr^{3+} to a C-peptide sample, a dominant Cr^{3+} adduct with C-peptide was observed by mass spectrometry analysis. Furthermore, an increase in ATP release was observed for a period of 72 hours for the Cr^{3+} activated sample, as opposed to 24 hours for that of Fe^{2+}. Again, inactive C-peptide samples, where fresh Cr^{3+} was added displayed an increase in the ATP release. The same results were obtained when applied to glucose uptake measurements. There was a 31% increase in the amount of glucose entering the erythrocytes upon incubation of C-peptide and Cr^{3+}.

These results were significant in that this was the first demonstration of metal interactions with C-peptide, and that metal interactions with C-peptide are responsible for a specific biological activity. As mentioned before, various metals play integral roles in the body as well as complications due to diabetes. Zn is an extremely important metal

and is observed in high concentrations (mM) within the pancreas, so it is not unreasonable to believe that C-peptide-metal interactions could occur with Zn. Thus, ATP release and glucose uptake experiments were conducted with C-peptide activated with Zn^{2+}.[48] It was found that ATP release increased by 31% over control levels (i.e., erythrocytes alone) upon addition of Zn^{2+} activated C-peptide, while C-peptide addition without added metal or the addition of Zn only did not produce any increase in ATP release. Similar results were obtained for glucose uptake measurements, measured using ^{14}C-labeled glucose, where it was found that glucose transport into diabetic rabbit erythrocytes increased by 36%, although this was a smaller effect than that of control non-diabetic rabbit erythrocytes, which increased transport by 64%.

It is clear from these studies that C-peptide activated with certain metals plays a crucial role in certain biological activities. When attempting to gain a complete understanding of a biological molecule, both its function and structure must be understood. The functional significance of metal activated C-peptide has now been established, as described above. However, a greater understanding of the specific metal-C-peptide interactions that give rise to these functions remains to be determined. Examination of which residues in the C-peptide sequence are involved in metal binding and the relative binding strength of these residues needs to be understood. Such studies may also aid interpretation of the multiple conflicting prior studies described above that suggested different regions of the C-peptide sequence were important to activity. One technique that has been successful in these type of analyses is mass spectrometry.

1.6 Metal-Binding Analysis by Mass Spectrometry

Early studies on peptide-metal associations were performed using fast atom bombardment (FAB) ionization which produced singly charged peptide-metal complexes.[49-55] The more recent development of electrospray ionization (ESI) has subsequently enabled the analysis of peptide- or protein-metal complexes involving much larger biomolecules.[53, 56-59] Many different transition metal-peptide or protein complexes have been investigated by ESI-MS. However, to obtain information regarding the site of binding on the peptide or protein, collision-induced dissociation tandem mass spectrometry (CID-MS/MS) is typically used to fragment the ion along the peptide backbone while maintaining the non-covalent metal-peptide interaction. The details of this process will be discussed in the next chapter. These studies allow for the binding interactions of complexes to be determined, and have been investigated with alkali,[49, 50] alkaline earth,[51, 52] as well as transition metal elements.[53, 54] Generally, the site of the metal interaction has a strong influence on directing the fragmentation reactions. For example, abundant $[b_{n-1}+Cat+OH]^+$ product ions from monovalent alkali-containing peptide ions are observed due to coordination of the metal to two amide carbonyl groups.[50] Other reports have demonstrated alkali metals binding to the carboxylate terminus of the peptide.[55] The binding of transition metals such as Ca^{2+} have been shown to occur at deprotonated carboxylate groups of acidic amino acids.[53] It was

determined by Yu *et. al.*[56] that the gas-phase complexes are similar to their solution-phase counterparts.

One study on the binding properties of angiotensin peptides with Zn^{2+} showed that CID-MS/MS of the doubly protonated precursor ions of both angiotensin I and II resulted in extensive b- and y-type sequence ions,[60, 61] while CID-MS/MS of the $[M+Zn^{2+}]^{2+}$ precursor ions showed abundant Zn-bound fragment ions of the form $[M+aZn^{2+}+(c-2a)H^{+}]^{c+}$.[57] This allowed localization of the Zn^{2+} to the His6 and His9 residues.

Another more recent experiment explored the Zn^{2+}-binding properties of the amyloid fragment Aβ(1-16).[58] ESI-MS/MS was used to locate the Zn binding sites to 3 histidine and 1 arginine residues which are known to direct the peptide into a hairpin conformation. Zn has also been shown to bind to cysteine as well as acidic residues such as glutamic acid and aspartic acid.[62]

The binding properties of Cr^{3+} to the synthetic acidic peptides AAADA, EAAAG, AGGAAAA, GGDDAA, AAGEEAA, DGDAAA, EAEAAA, DAADAA, EAAEAA, EAAAEA, EAAAE, EEE, DDDD, AND EEEEEEE have also been explored.[59] These peptides are similar to C-peptide in that C-peptide has 5 acidic residues and no histidine or cysteine residues. This study determined that the Cr^{3+} was binding to the carboxylate groups of the acidic amino acids. Sequential losses of water from the Cr^{3+} bound molecular ion indicated that not all acidic residues within the

peptide are involved in the binding. It was also found that a peptide such as AGGAAAA-OCH_3 which contains no acidic residues was still able to bind Cr^{3+}, even though this occurred at low abundances. This suggests that carboxylate groups may not necessarily be the only groups involved in binding.

Aims of This Thesis:

As described above, MS and MS/MS methods have been shown to be useful tools for the analysis of non-covalent peptide-metal complexes when ESI is used as the ionization source. Therefore, in order to obtain further insights into the binding interactions of metal ions to proinsulin C-peptide, the following specific aims were formulated.

1. Characterization of proinsulin C-peptide using 'top down' MS/MS
2. Characterization of Zn^{2+} binding sites within activated proinsulin C-peptide
3. Characterization of proinsulin C-peptide mutants formed by single amino acid substitution using 'top down' MS/MS
4. Characterization of Zn^{2+} binding sites within proinsulin C-peptide mutants formed by single amino acid substitution using 'top down' MS/MS
5. Determination of the effect of single amino acid substitutions or C-peptide segments on the relative binding of Zn^{2+} to proinsulin C-peptide.
6. Characterization of the Zn^{2+} binding sites of the C-terminal pentapeptide of C-peptide (EGSLQ) and its mutant AGSLQ, and examination of their biological activity.

CHAPTER TWO:

Strategies for the Synthesis and Characterization of Proinsulin C-peptide, its Mutants and Metal Binding

2.1 Solid Phase Peptide Synthesis (SPPS) of the C-peptide Mutants

2.1.1 Materials

Synthesis was conducted from the C- to N-terminus on a Wang resin preloaded with an N-α-Fmoc protected glutamine residue purchased from EMD Biosciences (San Diego, CA). N-α-Fmoc protected amino acid building blocks Fmoc-Gln(Trt), Fmoc-Leu, Fmoc-Ser(tBu), Fmoc-Gly, Fmoc-Glu(OtBu), Fmoc-Ala, Fmoc-Pro, Fmoc-Val, Fmoc-Asp(OtBu) were purchased from EMD Biosciences (San Diego, Ca) as well. Sequenal grade trifluoroacetic acid (TFA) was purchased from Pierce (Rockford, Il). Reagent grade dimethyl formamide (DMF) was purchased from Jade Scientific (Canton, MI) and dried under 3Å molecular sieves (Spectrum Chemicals, Gardena, CA). Reagent grade O-(Benzotriazol-1-yl)-N,N,N',N'-tetramethyluronium tetrafluoroborate (TBTU) and 1-Hydroxybenzotriazole hydrate (HOBt) were purchased from Peptides International (Louisville, KY). Reagent grade piperidine, diisopropylethylamine (DIPEA), phenol, potassium cyanide, ninhydrin, ethanedithiol (EDT), triisopropylsilane (TIS) and pyridine were purchased from Sigma Aldrich (St. Louis, MO).

Resins were weighed into 5 mL Toriq fritted-syringes (Fisher Scientific, Pittsburgh, PA) fitted with a 3-way stopcock (VWR, West Chester, PA). Washing was

achieved using a Vac-Man laboratory vacuum manifold (Promega, Madison, WI), which also allowed multiple syntheses to be conducted at once.

2.1.2 Synthesis

SPPS was achieved through a stepwise procedure consisting of two steps. The first step is deprotection of the Fmoc protecting group from the N-terminal end of the resin bound amino acid. The second step involves activation of the next amino acid followed by coupling to the resin. The final step, carried out after the sequence is completed, involves final deprotection of the N-α protecting group at the N-terminus, followed by cleavage of the peptide from the resin as well as any orthogonal protecting groups on the side chains of any amino acids. These steps will be outlined below. The sequences of the C-peptide mutants and C-peptide segments that were prepared in this study are listed below in Table 2.1

Sequence	Abbreviation
EAEDLQVGQVELGGGPGAGSLQPLAL**A**GSLQ	**E27A**
EAEDLQVGQV**A**LGGGPGAGSLQPLALEGSLQ	**E11A**
EAE**A**LQVGQVELGGGPGAGSLQPLALEGSLQ	**D4A**
EA**A**DLQVGQVELGGGPGAGSLQPLALEGSLQ	**E3A**
AAEDLQVGQVELGGGPGAGSLQPLALEGSLQ	**E1A**

Table 2.1: Sequences of the single amino acid mutants of C-peptide that were synthesized, along with their respective abbreviations. Locations of the alanine substitutions are labeled in bold and underlined on the sequences.

Synthesis of the E27A mutant was performed on a 0.15 mmol scale. Synthesis of the E1A, E3A, D4A, E11A mutants, the C-terminal peptide segment EGSLQ and the alanine substituted C-terminal peptide segment AGSLQ, were performed on a 0.1 mmol scale.

2.1.2.1 Deprotection

After swelling the resin in 3 mL DMF for 15 minutes, the resin was then washed once with 30% piperidine in anhydrous DMF. 3 mL of the piperidine solution was then added and the resin was thoroughly mixed for 25 minutes. The resin was then filtered and washed resin 8 times with 5 mL DMF until the pH was < 8.

2.1.2.2 Coupling

For each coupling step, at least a 5:1 excess of amino acid to resin was used. The amino acid was pre-activated by dissolving in 1.5 ml activator solution (0.5 M TBTU, 0.5 M HOBt in DMF) and 300 μL of DIPEA. The solution was vortexed to completely dissolve the amino acid, then added to the resin. The resin was then mixed for 15 minutes, filtered and washed 5x with 5mL of DMF.

2.1.2.3 Ninhydrin Test

To determine if the coupling reaction was successful, a ninhydrin color test was used.[63] Ninhydrin reacts with primary amines to form a deep blue color. Therefore, in the event of an incomplete coupling, deprotected primary amines will be present on the residual N-terminus of the initial peptide, which will cause the resin to turn blue when the

test is conducted. If the coupling is successful, all resin-bound peptide will be coupled with a protected amino acid.

This test was performed by taking a small amount of resin (2 mg) from the syringe and placing it in a glass test tube. The resin was then washed with 2 mL of ethanol. Then, 150 μL each of 0.28 M ninhydrin in ethanol, 42.5 M phenol in ethanol, and 20 μM (aq) KCN in pyridine were added to the resin, and the solution was mixed thoroughly. After incubation at 100 °C for 10 minutes, the color was inspected. If the solution and resin were blue in color, the coupling process was repeated using the same amino acid as described above. If the solution was yellow, the synthesis was continued.

During the synthesis, it was observed that for particular residues, such as glutamine, more than two coupling events were required in order to completely couple the amino acid. In this event, a 10:1 excess of amino acid: resin was used and the coupling time was increased from 15 to 20 minutes. The dissolved amino acid was also left to activate in solution for 5 minutes prior to addition to the syringe.

2.1.2.4 Final Deprotection/Cleavage

Once the target amino acid sequence was completed, a final round of deprotection was performed. After the deprotection, the resin was then washed with 5 x 5 mL of ethanol and allowed to dry. The resin was observed to shrink as the methanol evaporated. A cleavage solution containing 95% TFA, 0.5% water, and 0.5% TIS was freshly prepared, then added to the resin. The stopcock of the syringes were removed and replaced with a cap, and the solution was left to mix thoroughly for 3 hours.

2.1.2.5 Work up/Extraction

Once the cleavage was completed, the contents of the syringe were emptied into a 100 mL round-bottom flask, and then washed with 2 mL of TFA. The TFA was then evaporated under nitrogen until about 100 μL of solution remained. The crude peptide was then precipitated by adding 10 mL of cold ether. The precipitate was then vacuum-filtered over a 30 mL Buchner funnel attached to a 125 mL side-arm flask. The precipitate was then put into another 100 ml round-bottom flask and reconstituted in water and, if necessary, a minimal amount of 25% acetic acid solution. The peptides were then lyophilized overnight.

2.2 High Performance Liquid Chromatography (HPLC) Purification of C-peptide and its Synthetic Mutants

All peptides were purified by Reverse Phase-High Performance Liquid Chromatography (RP-HPLC) using a Shimadzu (Columbia, MD) LC-20AB solvent delivery system coupled with a SPD-20AV UV/VIS detection system. Samples were dissolved with vortexing in a minimal amount of water, and up to 20% ACN was added in cases where the peptide was not completely soluble. Samples were injected using a Rheodyne model 9215 injection valve (Oak Harbor, WA) and a 2 mL stainless steel sample loop onto a Vydac C18 Protein and Peptide column purchased from Grace (Deerfield, IL). For purification of human proinsulin C-peptide (Genscript, Piscataway, NJ), a linear gradient from 100% buffer A to 100% buffer B over 60 minutes was used. A variety of gradient conditions were evaluated to achieve optimal separation of the

synthesized C-peptide mutant peptides. Ultimately, peptides were eluted using the non-linear gradient conditions shown in Table 2.2

Solvent A consisted of 0.1% HPLC-grade TFA (Pierce, Rockford, IL) in water purified using a Nanopure Diamond filtration system from Barnstead (Dubuque, IA) with a resistance of 18.2 MΩ. Solvent B consisted of 60% HPLC-grade acetonitrile (ACN) purchased from EMD biosciences (Gibbstown, NJ), containing 0.089% HPLC-grade TFA. Solvents were sparged with helium for 15 minutes prior to running the HPLC. Peptides were monitored at 215 nm and individual fractions were collected into 15 mL centrifuge tubes. The purity of these fractions were then determined by mass spectrometry analysis. Pure fractions containing the desired peptide were pooled and lyophilized overnight.

Time (min)	% A	% B
0	100	0
20	66	34
100	33	67
120	0	100
125	0	100
127	100	0
135	Stop	Stop

Table 2.2: Gradient used for C31 mutant purification

2.3 Mass Spectrometric Analysis

2.3.1 Introduction

Mass spectrometry involves the formation of gas-phase ions that are then separated by various mass analyzers on the basis of their individual mass to charge (m/z) ratios. The separated ions are then detected and a spectrum is output as a function of both the m/z and the abundance of the ions present in the sample. Additionally, selected ions may be isolated and subjected to dissociation, followed by mass analysis of the resultant product ions, to allow for structural information to be obtained. The two crucial components of a mass spectrometer are the ionization source and the mass analyzer. An in-depth discussion of the theory behind the mass spectrometry methods employed in the studies performed in this thesis is given below.

2.3.2 Ionization Sources

A variety of ionization methods have been developed over the years, including electron impact ionization (EI), chemical ionization (CI), fast atom bombardment (FAB), electrospray ionization (ESI) and matrix-assisted laser desorption-ionization (MALDI). Both ESI and MALDI have gained wide use in the analysis of biological molecules because of their ability to transfer these large molecules intact into the gas-phase. Both MALDI and ESI were used in examination of the structure and binding of proinsulin C-peptide and its mutants, and these ionization methods are described in more detail below.

2.3.2.1 Electrospray Ionization (ESI)

ESI is an atmospheric pressure ionization technique that was introduced by John Fenn and coworkers in the 1980's [64]. This is in contrast to previous ionization methods such as CI and EI where the ions were required to be formed under vacuum. Formation of ions under higher pressures allows for "soft" ion formation, where the ion is formed with minimal internal energy, thereby undergoing minimal fragmentation. ESI also produces multiply-charged ions, which allow for the analysis of very large biological molecules in mass analyzers with a limited m/z range. The dissociation of different multiply charged ions often results in different fragmentation pathways, often giving rise to different structural information for each charge state.

In ESI, the sample is dissolved in a solution typically consisting of methanol, acetic acid and water. The sample is pumped through a narrow (100 μm i.d.) silica capillary tubing, with the tip of the capillary placed near the entrance to the mass spectrometer (~2 cm). A schematic of a typical ESI interface is shown in Figure 2.1. The tip of the capillary is maintained at atmospheric pressure. A high voltage (3-5 kV) is applied to the capillary with respect to ground which is normally the entrance to the mass spectrometer, and the solution is pumped at flow rates in the 1-10 μL/min range. The high voltage in combination with the short distance from the counter electrode creates a large electric field, resulting in charge buildup at the tip of the capillary. The exiting solvent therefore forms a Taylor cone at the tip to alleviate the charge density. When the charge density on the Taylor cone becomes too great, a continuous series of electrostatic droplets form, which then undergo a series of coulombic fission events whereby solvent

is evaporated from the droplet to form the ions. Figure 2.1 also shows a schematic of droplet formation and evaporation.

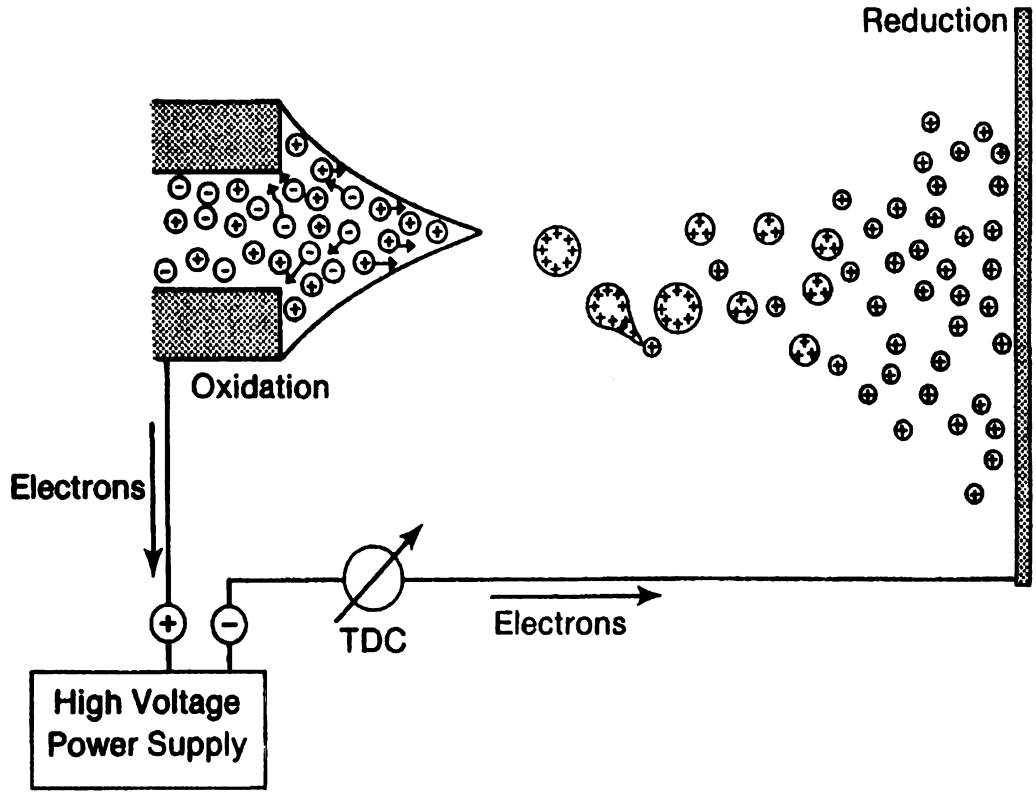

Figure 2.1: Representation of droplet formation in ESI. (Adapted from reference 65)

The mechanism for the formation of ions by ESI has been a subject of debate over many years. Two main theories have been proposed: the charge residue model (CRM) [66] and the ion evaporation model (IEM) [67,68]. The CRM mechanism proposes that as the droplets lose solvent molecules through evaporation, Coulombic fission occurs when the surface charge density on the droplet becomes greater than the surface tension of the

liquid. This will occur when the charge is greater than a limiting value, termed the Rayleigh Limit, and is given by Equation (1)

$$q^2 = 8\pi^2 \varepsilon_0 \gamma D^3 \quad (1)$$

where q is the charge on the droplet, γ is the surface tension, and D is the diameter of the spherical drop. When this limit is reached, the droplet will explode into smaller droplets, and will continue until a droplet is formed with only a single analyte molecule. As the remaining solvent evaporates, a gas-phase ion is formed. The IEM suggests that the droplet undergoes a series of Rayleigh breakdowns similar to the CRM to form successively smaller droplets. However, in contrast to the CRM, the IEM proposes that ions are evaporated directly from the surface of the droplet as the electric field increases due to solvent evaporation. Once the electric field becomes stronger than the solvation forces, the ion will be evaporated directly into the gas phase. Even though both theories offer competing views for gas-phase ion formation, it has been shown [67] that ions can be formed by either mechanism, where smaller molecules are formed by IEM, and larger biological molecules are formed by CRM.

2.3.2.2 Matrix-Assisted Laser Desorption Ionization (MALDI)

Matrix-assisted laser desorption ionization is a technique developed by Karas and co-workers in the late 1980's [69] for the analysis of large molecular weight biomolecules. This ionization method involves the use of a laser for desorption of the analyte as well as for ionization. In this technique, the sample is dissolved (typically in water and organic

solvents such as acetonitrile (ACN), along with small amounts of trifluroacetic acid (TFA)), and is then mixed on a sample stage with a matrix compound containing a UV-absorbing chromophore. The sample is then allowed to evaporate, co-crystallizing the analyte and matrix together. The selection of the matrix component is crucial to a MALDI experiment, in that the compound must absorb at the wavelength of the laser to be used, and it also must have a low vapor pressure that it will not evaporate once inserted into the vacuum chamber. The sample is then inserted into the source region of the mass spectrometer, which is maintained at vacuum. The laser is then pulsed onto the sample, and the matrix will absorb the laser radiation. The ionization process of MALDI is still not well understood[70, 71], but both analyte and matrix ions are formed. This causes interference ions due to clusters of matrix ions in the low-mass region of the spectrum.

MALDI has become a very effective technique for analyzing large molecular-weight and polar molecules, such as biomolecules. Because this process forms primarily singly-charged ions, the ranges of mass analyzers that are effective for this technique are limited. Typically, TOF mass analyzers are used as they have the advantage of unlimited mass range. However, in the experiments conducted, due to the relatively low mass of the C-peptide and its mutants, MALDI was able to be used to obtain tandem mass spectra for the singly protonated $[M+H^+]^+$ ions of C-peptide and its mutants, using a linear quadrupole mass analyzer.

2.3.3 Mass Analyzers

In order to obtain a mass spectrum, the gas-phase ions that have been formed must be separated according to their m/z values. Ion formation allows for manipulation of the ions using various fields. A number of mass analyzers have been developed over the years including magnetic sector, time of flight (TOF), quadrupole (Q), quadrupole ion trap (QIT) (including both 3D and linear configurations) and Fourier transform ion cyclotron resonance (FT-ICR). In the experiments conducted here, quadrupole ion trap and linear ion trap mass analyzers were used. Ion traps, coupled with ionization methods such as ESI are particularly attractive for use in the analysis of both small and large biomolecules, as they are capable of multiple stages of tandem mass spectrometry (MS^n) to obtain structural information.

2.3.3.1 Quadrupole Mass Analyzer

Ideally, a quadrupole mass analyzer consists of 4 hyperbolic-shaped rods aligned parallel to one another as shown below in Figure 2.2. However, cylindrical rods are typically used for cost effectiveness and practicality. Ions entering through the z-dimension of the mass analyzer experience a quadrupole electric field which consists of an alternating current (AC) signal and a direct current (DC) signal. The DC signals on one opposing pair of rods is of opposite sign with respect to the other pair, while the AC signal on each pair of rods are 180 degrees out of phase with respect to each other. When positive ions enter the trap, they are attracted to a pair of rods when a net negative potential is observed and repelled from a pair of rods (i.e., focused toward the center of the assembly) when a net positive potential is observed. Because an AC signal is applied,

the polarities on the rods will change rapidly, which will focus the ions to the center of the quadrupole as the ions are passing through along the z-axis.

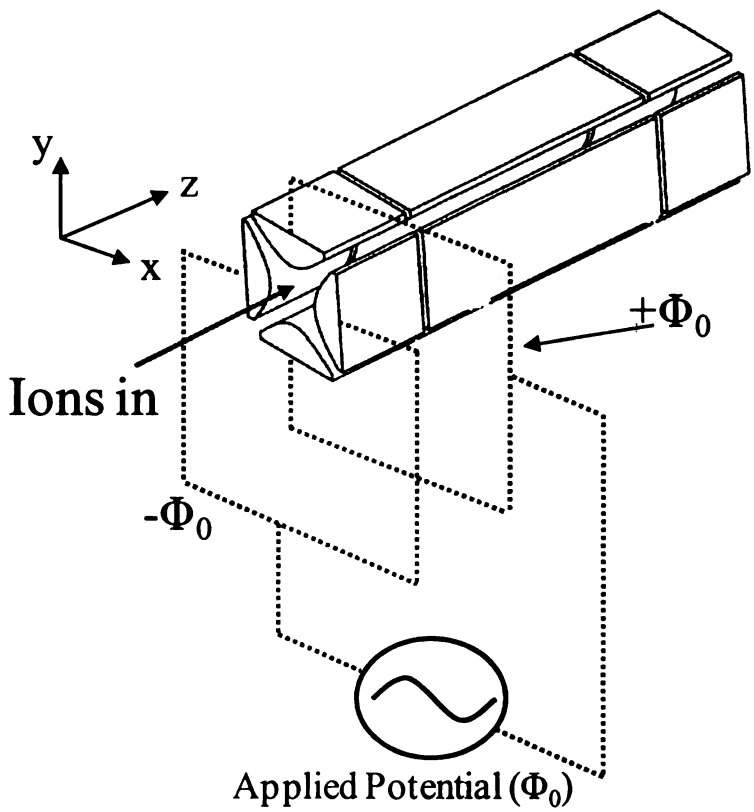

Figure 2.2: Schematic of a quadrupole mass spectrometer, showing applied AC and DC potentials (Φ_0).

The applied potential is given the symbol Φ_0, and is described by the following equations

$$\Phi_0 = +(U\text{-}V\cos\omega t) \quad \text{and} \quad -\Phi_0 = -(U\text{-}V\cos\omega t) \qquad (2)$$

where U is the applied DC signal, V is the zero-to-peak amplitude of the AC signal in the RF region, and ω is the angular frequency, which can be given in terms of the applied RF frequency, f ($\omega = 2\pi f$). Ions entering the quadrupole assembly along the z-axis experience forces in the x and y directions. These forces can be expressed by equations (3) and (4) below

$$F_x = m\frac{d^2x}{dt^2} = -ze\frac{\partial \Phi}{\partial x} \tag{3}$$

$$Fy = m\frac{d^2y}{dt^2} = -ze\frac{\partial \Phi}{\partial y} \tag{4}$$

where Φ is a function of both x and y and can be written in terms of Φ_0

$$\Phi_{xy} = \Phi_0(x^2 - y^2)/{r_0}^2 = \frac{(x^2 - y^2)(U - V\cos\omega t)}{{r_0}^2} \tag{5}$$

Equation (5) can be differentiated and rearranged to achieve the equations of ion motion in the x and y directions, given by equations (6) and (7) respectively

$$\frac{d^2x}{dt^2} + \frac{2ze}{m{r_0}^2}(U - V\cos\omega t)x = 0 \tag{6}$$

$$\frac{d^2y}{dt^2} - \frac{2ze}{mr_0^2}(U - V\cos\omega t)y = 0 \qquad (7)$$

When comparing these equations to the equation solved by Mathieu[72] given below in equation (8), the working equations for the quadrupole mass analyzer can be determined

$$\frac{d^2u}{d\xi^2} + (a_u - 2q_u\cos 2\xi)u = 0 \qquad (8)$$

In equation (7), u represents motion in either the x or y direction, and $\xi = \omega t/2$. The variables a and q are dimensionless parameters. When equations (6) and (7) are rearranged in terms of the parameters a and q, the working equations of ion motion in the quadrupole are obtained as shown in equations (9) and (10).

$$a_u = a_x = -a_y = \frac{8zeU}{m\omega^2 r_0^2} \qquad (9)$$

$$q_u = q_x = -q_y = \frac{4zeV}{m\omega^2 r_0^2} \qquad (10)$$

These equations state that ions of a given mass-to-charge ratio in the quadrupolar field will pass through the assembly as long as the motion along the x and y directions does not exceed the value of r_0 (the distance between the center of the quadrupole and the

rods). It can be noted that equations (9) and (10) are a function of both m/z, the applied DC amplitude U, and the applied RF amplitude V. For a given experiment, r_0 and ω are fixed, and e is the elementary charge (1.602×10^{-19} C) which remains constant. Therefore, the stability of an ion is determined as a function of the amplitudes of the RF and DC potentials applied to the rods. Equations (9) and (10) can be rearranged to solve for U and V, respectively, giving equations (11) and (12).

$$U = a_u \frac{m\omega^2 r_0^2}{8ze} \tag{11}$$

$$V = q_u \frac{m\omega^2 r_0^2}{4ze} \tag{12}$$

A stability diagram plotting the a vs. q parameters can be constructed which will show values of a and q, and therefore values of U and V, where the ions in the quadrupole will be stable and pass through the trap. This is shown in Figure 2.3. In this figure, the area under the curve represents where ions will pass through the instrument. Because a and q are dependent upon m/z, U, and V, fixed values of U and V will result in differing different a and q values for ions of various m/z. The apex of the curve occurring at $a = 0.237$ and $q = 0.706$ represents the point where only one m/z value will remain stable, creating a mass filter. By adjusting the parameters U and V over time so ions of increasing m/z will successively pass through the apex of the diagram, the quadrupole may be operated as a mass analyzer.

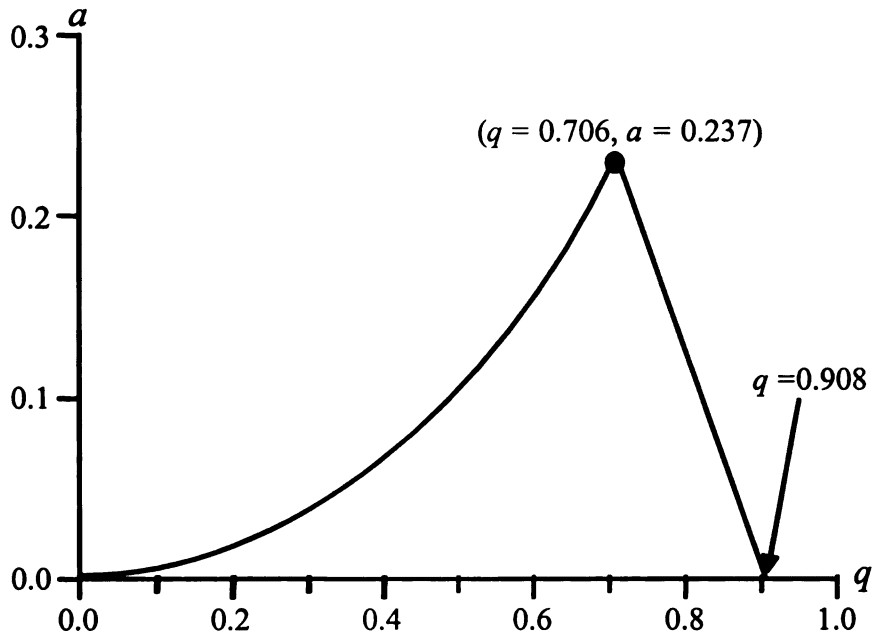

Figure 2.3: Stability diagram for a quadrupole mass analyzer.

In contrast, by not applying a DC potential (i.e., $a = 0$) to the quadrupole, ions will lie along the x-axis of Figure 2.3, where many different m/z values may be passed through the assembly, only being limited by a low-mass-cutoff imposed by the RF amplitude which results in ions with q values higher than 0.908 being unstable. The application of this will be discussed in more detail in the next section in terms of the quadrupole being used as an ion trap as opposed to a mass filter.

2.3.3.2 Quadrupole Ion Trap Mass Analyzer

A quadrupole ion trap consists of a hyperbolic-shaped ring electrode capped by two hyperbolic end cap electrodes. Each end cap electrode has a hole drilled in the center for ion injection/ejection. A schematic of a quadrupole ion trap is shown in Figure 2.4,

where r_0 is the distance from the center of the trap to the ring electrode and z_0 is the distance from the center of the trap to the end cap electrodes.

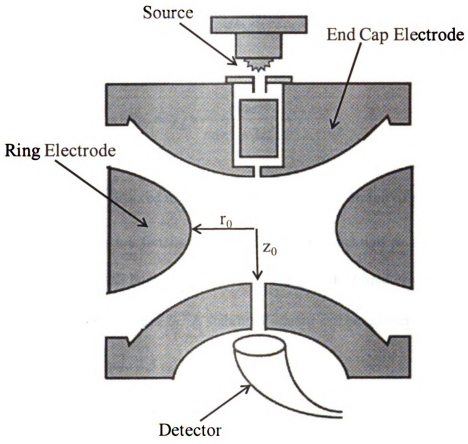

Figure 2.4: Schematic of a quadrupole ion trap (Adapted and modified from Reference 72)

A variable-amplitude radio frequency (RF) is applied to the ring electrode which follows the same relationship as equation (1). The end cap electrodes are typically held at ground.

Ions entering the trap will experience the RF potential in three dimensions (r and z), and stable ions will be bound inside the trap. Much like the quadrupole, the working

equations for ion motion in the trap may be derived using the Mathieu equation (8), to obtain equations (13) and (14)

$$a_u = a_z = -2a_r = \frac{-16zeU}{m(r_0^2 + 2z_0^2)\omega^2} \tag{13}$$

$$q_u = -2q_r = q_z = \frac{8zeV}{m(r_0^2 + 2z_0^2)\omega^2} \tag{14}$$

Again, r_0, z_0, and ω are all fixed for a given instrument. For an ion of a given m/z ratio, the parameters a and q are a function of the RF and DC potentials as in the quadrupole mass analyzer. An ion will be stable in the trap as long as the trajectories along the r and z dimensions do not equal r_0 and z_0. A stability diagram can be constructed by plotting a vs. q, and is shown in Figure 2.5

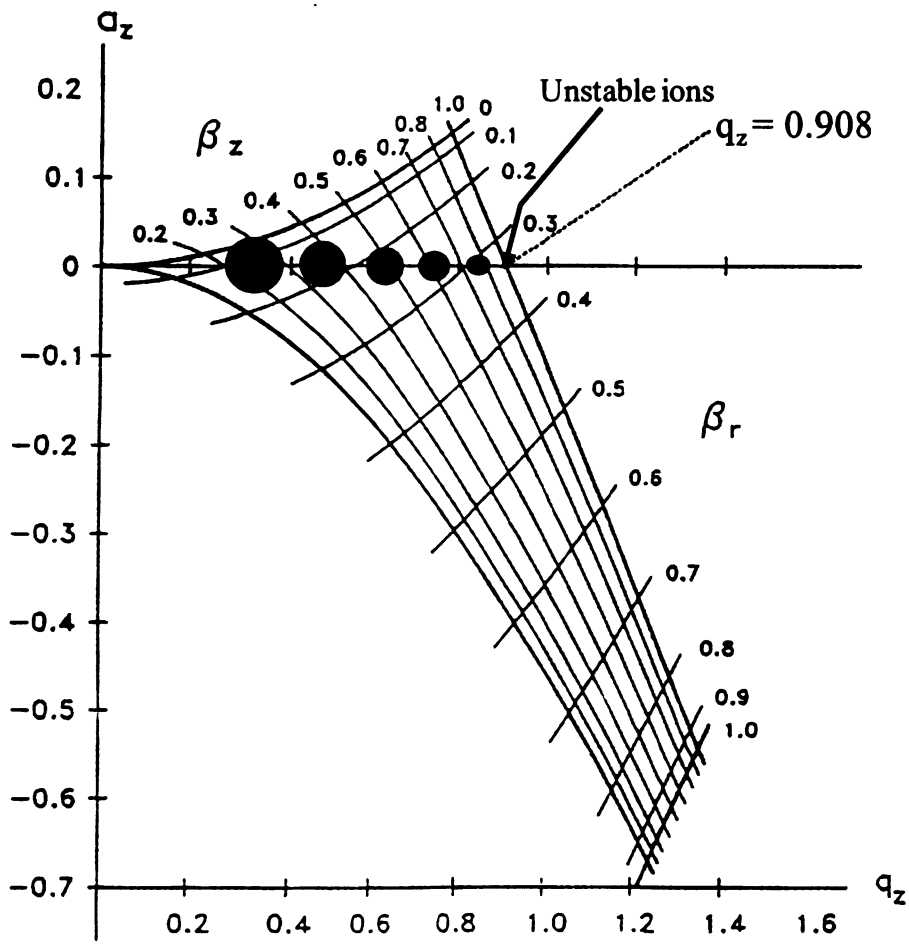

Figure 2.5: Mathiew stability diagram for a 3D ion trap showing stability of ions of different m/z values. Larger balls indicate larger m/z values. (Adapted and modified from Reference 72)

β is a fundamental stability parameter and will be discussed in more detail later. This diagram shows the regions of a and q, and therefore the values of U and V where ions will be stable in the trap. In commercial instruments, no DC potentials are applied, therefore $a = 0$ and ions will be aligned along the x-axis of the diagram. The boundary of the diagram where $\beta = 1$ is at $q = 0.908$. This means that an ion having a q-value approaching 0.908 will become unstable and travel farther than z_0. This point is termed

the stability limit. Looking at equation (14), the value of q is proportional to the amplitude of the applied RF potential, and inversely proportional to the m/z ratio of the ion. Therefore, ions of higher m/z will have a lower q-value, and ions of small m/z will have a larger q-value, bringing them closer to the stability limit. This imposes a low-mass-cutoff value for the ion trap.

Ions are injected into the trap, where they encounter an inert bath gas, typically helium. This gas is held at a constant pressure of 1 mTorr, and ions will collide with the gas and transfer kinetic energy to the Helium. This "collisional cooling" focuses the ions into the center of the trap, which improves the trapping efficiency. Another factor in the trapping efficiency of the ions is the Dehmelt pseudopotential well, which is given by equation (15)

$$\overline{D_z} = q_z \frac{V}{8} = \frac{zeV^2}{m(r_0^2 + 2z_0^2)\omega^2} \tag{15}$$

A graphical representation of equation (15) is shown below as a function of q in Figure 2.6. The potential well is a measure of how stable the ion is in the trap. Ions that lie in the q region around 0.8 are held at the lowest potential and are therefore most stable.

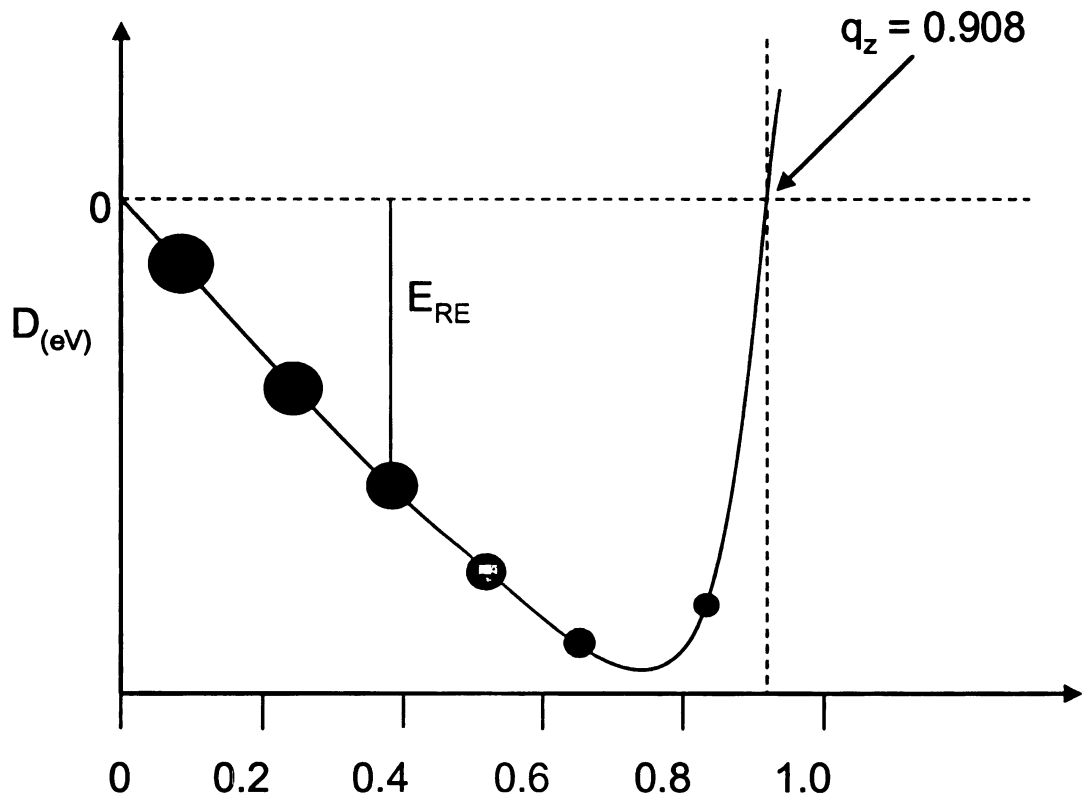

Figure 2.6: Diagram of Dehmelt pseudopotential well in a 3D ion trap. E_{RE} is the energy where resonance ejection typically is carried out. (Adapted from Reference 73)

To acquire a mass spectrum, the RF amplitude is increased, which brings the ions closer and closer to the stability limit. As an ion approaches a q value of 0.908, its motion along the z-axis will increase and the ion will travel farther than the dimension z_0. When doing this, the ion will pass through a hole in the end cap electrode where it will strike the detector. Thus, as the RF potential is ramped, ions of increasing m/z will reach the stability limit and become ejected from the trap through the z-axis. This method is termed ejection at the stability lim[illegible] This, however, is not the most effective way of

acquiring a mass spectrum. The pseudopotential well depth near the stability limit becomes very steep, which can cause more than one m/z value to be ejected at a certain RF potential. This results in a loss of resolution in the mass spectrum.

Another method called resonance ejection is used instead. In this method, a high amplitude RF potential is applied to the end-cap electrodes, termed the supplemental voltage, with a frequency that corresponds to a $q \sim 0.8$. As mentioned before, ions at this q value are in the deepest part of the potential well. Due to intertia, ions in the trap will be oscillating at a secular frequency, f, which is less than the frequency, v, of the RF field applied to the ring electrode. The relationship between the applied frequency and the secular frequency is shown in equation (16)

$$f_z = \frac{\beta_z v}{2} \tag{16}$$

where β_z is the stability parameter mentioned above, and is related to a and q by equation (17), when $q < 0.4$.

$$\beta_z = \left[a_z + \left(\frac{q_z^2}{2} \right) \right]^{1/2} \tag{17}$$

As shown in Figure 4, β will have a maximum value of 1 at $q = 0.908$, the stability boundary. Therefore, ions will be oscillating in the trap at a maximum of one-half the fundamental frequency. As the RF potential on the ring electrode is ramped, the secular frequencies of the ions in the trap will approach that of a supplemental frequency that can

be applied to the end caps. When the ions become in resonance with this supplemental frequency, their kinetic energy will increase and they will begin to move farther along the z-axis until they exit the trap and reach the detector. The main benefit of resonance ejection is an increase in resolution. Ions of the same m/z coming into resonance with the supplemental frequency will become coherent, resulting in a "packet" of ions which allows for the ions of same m/z to be ejected in a smaller range of RF potentials. Resolution is inversely proportional to the rate at which the RF potential is increased, called the scan rate. Therefore, greater resolution may be obtained at the cost of analysis time.

2.3.3.3 Tandem Mass Spectrometry (MS/MS)

One of the main benefits of ion trap instruments is their ability to perform multi-stage mass spectrometry. This consists of consecutive steps of trapping ions, isolation of a desired precursor ion, fragmentation of the precursor ion resulting in a series of product ions, followed by mass analysis. A single fragmentation event is termed tandem-mass spectrometry, or an MS/MS experiment. Multiple stages of isolation and fragmentation can be conducted, and are called MS^n experiments.

The process of ion injection and storage was discussed previously. Once ions have been trapped, a precursor ion must be selected for isolation. This is done by applying a high amplitude "notched" broadband supplemental RF potential to the end cap electrodes. This potential will ideally contain all frequencies except for that of the desired ion. Application of this potential will excite all other ions and eject them out of the trap, leaving only the desired ion. This ion is then subjected to fragmentation by the

application of a low amplitude supplemental RF potential corresponding to the secular frequency of the isolated ion stored at a particular q value. The ion will become translationally excited, and collide with the helium bath gas, whereby translational energy is converted to vibrational energy, causing the ion to fragment. Newly-formed product ions will fall out of resonance with the supplemental RF signal as they will have new secular frequencies. These ions will become focused in the center of the trap through 'cooling' collisions with the background gas, following which mass analysis by resonance ejection can be performed. If the fragmentation is conducted at a high q-value, many of the low-mass fragment ions may be below the low-mass cutoff and will not remain in the trap. To circumvent this, ion activation is performed at a lower q-value, (typically $q = 0.25$) to ensure that fragment ions remain in the trap while allowing enough energy to be input into larger molecules to allow them to fragment without ejecting them.

2.3.3.4 Linear Ion trap

While quadrupole ion traps have their advantages, a few disadvantages arise due to their design. First, as mentioned above, ions entering the trap experience the quadrupolar field in all three dimensions. Positively charged ions entering the trap during the positive cycle of the applied RF potential, when the amplitude is high, will be repelled away from the trap and be lost. During high negative amplitudes, positively charged ions will be accelerated in the z-dimension and pass through the trap undetected. Only a small range of RF values will therefore allow ions to be stably trapped. This property is termed ion injection efficiency and is a major limit to sensitivity in ion trap MS.

Another disadvantage arises from the ability to eject ions out of the trap, termed ejection efficiency. In 3D traps, ions are excited along the z-axis in both directions. Therefore, when performing resonance excitation, half the ions will be ejected out of the entrance endcap electrode trap in the direction opposite to the detector. To overcome this, a positive potential barrier can be applied to the source-end of the ion trap which will repel ions out to the detector, thereby increasing ejection efficiencies and therefore sensitivity.

The third disadvantage that 3D ion traps exhibit arises from the number of ions that the trap can store. Ions are stored at the center of the trap. Therefore, as the number of ions in the trap increases, positively charged ions of the same m/z that are oscillating with the same frequency will repel one another, causing the distribution of frequencies to increase, which causes peak broadening and a loss of resolution. This phenomenon is termed space-charge.

To overcome each of these limitations, a 2-dimensional linear ion trap[74, 75] may be used. This instrument employs a normal quadrupole mass analyzer as shown in Figure 2.2 operated in RF only mode to trap ions in the x- and y-dimensions. A positive DC potential is applied to electrodes positioned at the ends of the quadrupole, which effectively traps ions in the z-dimension. In the linear ion trap, ions are stored along the z-axis of the trap, which decreases space-charge effects and allows for greater ion storage capacity. Also, the ions feel very little of the applied quadrupolar field in the z-axis, which greatly increases ion injection efficiencies. For mass analysis, ions are ejected radially in the x dimension, through holes cut into the rods, by resonance ejection similar to that in the 3D ion trap. Dual detectors placed on each side of the trap allow for greater

detection efficiencies. Linear ion traps therefore allow for much better sensitivities and are capable of higher resolutions than 3D ion traps. Therefore, the linear ion trap was employed for experiments requiring high resolution, such as resolving isotopic distributions of precursor and product ions.

2.3.4 Peptide Fragmentation Nomenclature

Peptides or proteins subjected to CID-MS/MS will proceed to fragment along various bonds within the peptide backbone. Cleavage at the same bond on succesive amino acids will result in the loss of the mass of the amino acid. These are called sequence ions, and comparing ions formed due to sucessive cleavages along the peptide or protein will allow the sequence to be determined. Depending on whether the charge is retained on the N- or C-terminus along with the location of the cleavage will result in different different sequence ions. A summary of the nomenclature for peptide fragmentation is shown in Figure 2.7. Peptides or proteins subjected to CID will typically undergo fragmentation at the amide bond, forming b- and y- type ions. When the charge is retained on the C-terminus, a y_n –type ion is formed, where n represents the number of amino acids contained in the ion. If the charge is retained on the N-terminus, a b_n-type ion is formed.

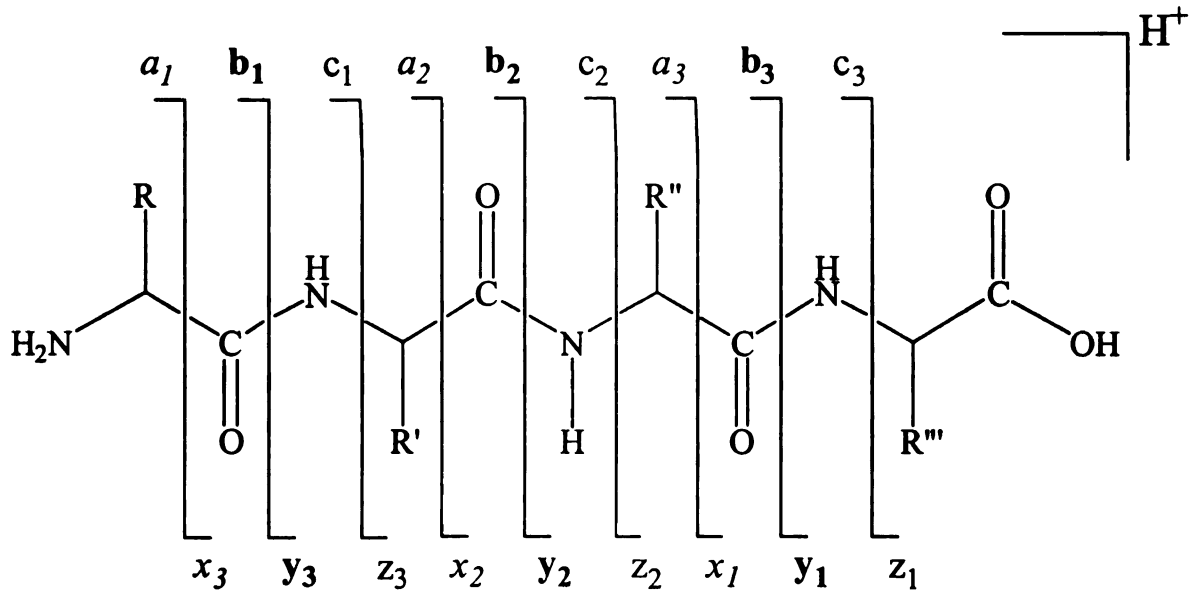

Figure 2.7: Nomenclature for peptide fragmentation

2.3.5 Instrumentation

Two different mass spectrometers were used in the current study; i) a Thermo Fisher Scientific (San Jose, CA) model LTQ linear ion trap equipped with nanospray (nanoESI) ionization, and ii) a Thermo Fisher Scientific (San Jose, CA) model vMALDI LTQ XL linear ion trap equipped with a MALDI ionization source.

2.3.5.1 MALDI-LIT Analysis

For MALDI experiments, 1 μM peptide samples were prepared in milli-Q water, as well as 50 mg/mL solutions of DHB matrix in 50% acetonitrile and 0.5% TFA. 0.5 μL each of the peptide and matrix solutions were spotted onto a stainless steel 96-well MALDI plate from Thermo (Waltham, MA), and allowed to crystallize. The plate was

then inserted into the instrument, and the correct spot was located. The laser power was adjusted to achieve maximum signal, but still obtain optimal resolution. This was found to be 40%. For MS spectra, 15 scans were acquired and averaged. Singly protonated ($[M+H]^+$) precursor ions were isolated using a window of 4 mass units to ensure that the entire isotopic distribution was isolated. The peptide was then fragmented using a normalized collision energy of 25% for a period of 30 msec at an activation q value of 0.2, and 200 scans were collected to achieve maximum signal to noise. As the sample was being ablated, the signal began to drop, so the laser spot was relocated to an area where more signal was obtained.

2.3.5.1 ESI-LIT Analysis

For MS and MS/MS analysis of C-peptide, C-peptide mutants or segments, samples were prepared in water by dilution from 33.7 μM (0.1 mg/ mL) peptide stock solutions. In order to reduce the observation of alkali metal adducts, the Barnstead water purification system was left to run for thirty minutes before making any solutions. Then, all samples were prepared using centrifuge tubes that had been thoroughly washed before filling to remove any excess salts from the tubes. For examination of Zn-activated C-peptide, C-peptide mutants or segments, samples of 10 μM C-peptide, C-peptide mutants or segments containing 10 μM $ZnCl_2$ were prepared by dilution from 1 mM $ZnCl_2$ and 33.7 μM (0.1 mg/ mL) peptide stock solutions. Samples were injected using a 250 μL syringe (SGE, Ringwood, Australia) into a nESI source using a silica capillary transfer tubing (360 μm O.D. x 100 μm I.D.) purchased from Polymicro Technologies (Tuscon, AZ). For Zn-binding experiments, 250 μL of a 10 μM $ZnCl_2$ solution was first flushed

through the lines in order to minimize the observation of sodium and potassium adducts in the mass spectra. This was done both at the beginning of the experiment as well as between samples. The sample was then pumped through a PicoTip emitter purchased from New Objective (Woburn, MA) with a tip diameter of 30 μm at a flow rate of 0.5 μL/min where it entered the mass spectrometer using a spray voltage of 1.8 kV and a capillary temperature of 250 °C. Other instrument settings included a capillary voltage of 20 V and a tube-lens offset voltage of 120 V. For MS spectra, 200 scans were acquired and averaged. For MS/MS, precursor ions were isolated using a window of 4 mass units to ensure that the entire isotopic distribution was isolated, fragmented using a normalized collision energy of 25% for a period of 30 msec at an activation q value of 0.2. 100 scans were collected to achieve maximum signal to noise. All spectra were acquired using the high resolution ZoomScan mode. MS and MS/MS spectra of solutions containing 1 μM C-peptide with 1 μM $ZnCl_2$ and 1 μM E27A with 1 μM $ZnCl_2$ were also acquired using the same instrument conditions. Instead of flushing with 20 μM $ZnCl_2$, the lines were flushed with a solution of 1 μM $ZnCl_2$ at the beginning of the experiment as well as in between samples.

CHAPTER THREE

Characterization of Proinsulin C-peptide, C-peptide Mutants, and Their Binding with Zn^{2+}

3.1 Top-down Characterization of Proinsulin C-peptide

3.1.1 Bottom-up and Top-down Proteomics

Currently, two methods for sequencing proteins are being employed, "bottom-up" and "top-down" proteomics. In "bottom-up" up proteomics, a protein sample is first digested, separated by HPLC and injected into the mass spectrometer. The individual peptides may be subjected to MS/MS analysis to sequence the individual peptide ions. The product ion masses along with the precursor ion mass can be input into a database where the protein may be identified. However, proteolytic digestion greatly increases mixture complexity, making the analysis more difficult. "Top-down" proteomics[76, 77] is a developing method which involves injection of a whole protein sample directly into the mass spectrometer. Similar to the "bottom up" approach, MS/MS analysis may be conducted, except the analysis is performed on the whole protein as opposed to individual peptides. The problem of mixture complexity is minimized using this technique, however other problems arise. Large molecules do not fragment well by CID due to the large number of vibrational modes available for energy redistribution. Therefore, higher charge states must be selected to provide the molecule with sufficient energy following collisional activation.

It has also been found that greater sequence coverage may be obtained by fragmenting multiple precursor ion charge states[78, 79], each giving access to different fragmentation pathways. This results in the formation of complementary sequence information amongst the various MS/MS spectra, resulting in an increase in sequence coverage. The differing fragmentation patterns for the different charge states has been determined to be due to differences in the ability of the ionizing proton(s) to move along the peptide backbone, causing fragmentation at each amino acid. This is termed "proton mobility".[80] When the number of protons is less than or equal to the number of arginine and lysine residues within the protein sequence, limited fragmentation is typically observed. These are termed "non-mobile" and "partially-mobile" conditions. When the number of protons is greater than the combined number of basic residues (arginine, lysine and histidine), the ionizing proton(s) are considered to be "mobile" and thus may move along the peptide backbone to yield more extensive sequence information. The fragmentation pathways for different proteins and peptides under different charge state conditions have been extensively studied.[78, 81, 82]

Although C-peptide, with a length of 31 amino acids and molecular weight of 3021 Da is not a protein *per se*; its analysis was performed on the intact biological peptide, without prior use of a digesting agent. Therefore, a top-down characterization strategy can be considered as being applied.

3.1.2 Characterization of proinsulin C-peptide

The ESI mass spectrum of HPLC-purified proinsulin C-peptide in water, obtained using a linear quadrupole ion trap mass spectrometer, is shown in Figure 3.1. The $[M+2H^+]^{2+}$, $[M+3H^+]^{3+}$ and $[M+4H^+]^{4+}$ charge states are all observed. Note that two major adduct ions corresponding to ionization of C-peptide with K^+ and Na^+ were also observed, consistent with the previously reported C-peptide metal activation experiments.[47] These ions are most likely formed due to the presence of Na^+ and K^+ in the water used to dilute the samples, as well as on the insides of the fused-silica capillary tubing that was used for introduction of the sample to the instrument. While not critical to the characterization of the protonated C-peptide, minimization and control of these adduct levels will prove important in the Zn^{2+} - binding experiments (see below). Analysis by MALDI yielded the singly protonated precursor ion (data not shown).

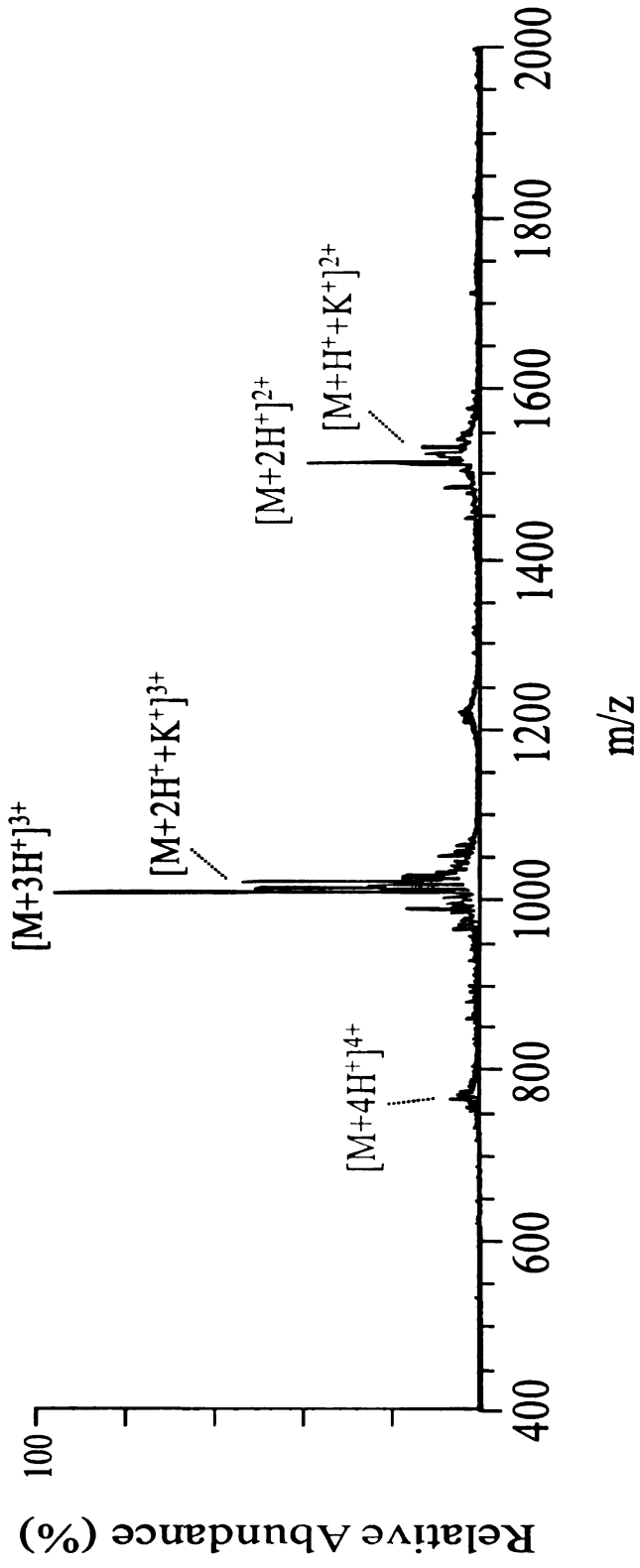

Figure 3.1: ESI Mass spectrum of 10 μM C-peptide in water.

To obtain maximum sequence information, the $[M+H^+]^+$, $[M+2H^+]^{2+}$, $[M+3H^+]^{3+}$, and $[M+4H^+]^{4+}$ charge states were subjected to CID-MS/MS. The MS/MS spectrum obtained for the $[M+2H^+]^{2+}$ charge state is shown in Figure 3.2. The MS/MS spectra for the $[M+H^+]^+$, $[M+3H^+]^{3+}$, $[M+4H^+]^{4+}$ are given in the Supporting Information section as Figures S1, S2, and S3, respectively. Extensive fragmentation for each charge state was observed.

To correlate a product ion in the mass spectrum with a sequence ion from the peptide, the charge of the ion was first determined. This was accomplished by examining the spacing of the peaks in the isotopic distribution, which follows the relationship given in equation (18)

$$z = 1/\Delta m \tag{18}$$

where z is the charge of the ion and Δm is the spacing between adjacent isotopic peaks. Once the charge state and therefore the mass of the ion was determined, it was then matched with a theoretical sequence ion mass. In the case of ions where a loss of 18 mass units was observed corresponding to a loss of water, a $^{\circ}$ symbol was used. Sequence ions observed to have a loss of 17 mass units corresponding to a loss of ammonia have a * label. The charge state of the ion, if greater than one, is designated on the label.

A summary of the product ions that were assigned and the sequence coverage that was obtained for each of the individual charge states, as well as an overall summary of the product ions and sequence coverage, are given in Figure 3.3. Product ions that were above 25% abundance in the mass spectra are labeled on the product ion and sequence coverage summaries.

From an examination of Figures 3.2, Figures S1, S2, and S3 and Figure 3.3, it can be seen that almost complete sequence coverage was obtained for nearly every charge state. Indeed, the only ions that are not observed are the low-mass b- and y-type ions, which is expected due to the limited low-mass cutoff of the ion trap. The overall sequence coverage in Figure 3.3 indicates that complete sequence coverage was obtained. This high degree of sequence coverage is unusual, particularly for large peptides. One rationale to explain this extensive sequence coverage, especially for the $[M+H^+]^+$ precursor ion, is the lack of basic residues within the peptide. As mentioned above, the presence of basic residues such as lysine or arginine will sequester ionizing protons, limiting their ability to move along the peptide backbone to facilitate fragmentation. For the C-peptide sequence however, which lacks basic residues, even the singly-charged ion is categorized as having a mobile proton. Thus, the proton is free to move along the backbone, allowing for fragmentation at nearly every bond. A few common cleavage patterns are present across the various charge states. For every charge state, the y_9 ion was observed as an abundant ion, and in the case of the $[M+3H^+]^{3+}$ and $[M+4H^+]^{4+}$ charge states, it was observed as the base peak. This product ion is formed by cleavage N-terminal to the Pro_{23} residue. Enhanced proline cleavage has previously been observed

to be a dominant process in proline-containing peptides[81] and proteins[78] under partially-mobile and mobile protonation conditions. Other dominant ions such y_{19} and y_{24} ions are also consistent with known peptide fragmentation patterns.[64] The wealth of sequence information obtained by fragmentation of C-peptide will be useful when comparing to the fragmentation of C-peptide bound with Zn^{2+} (see below).

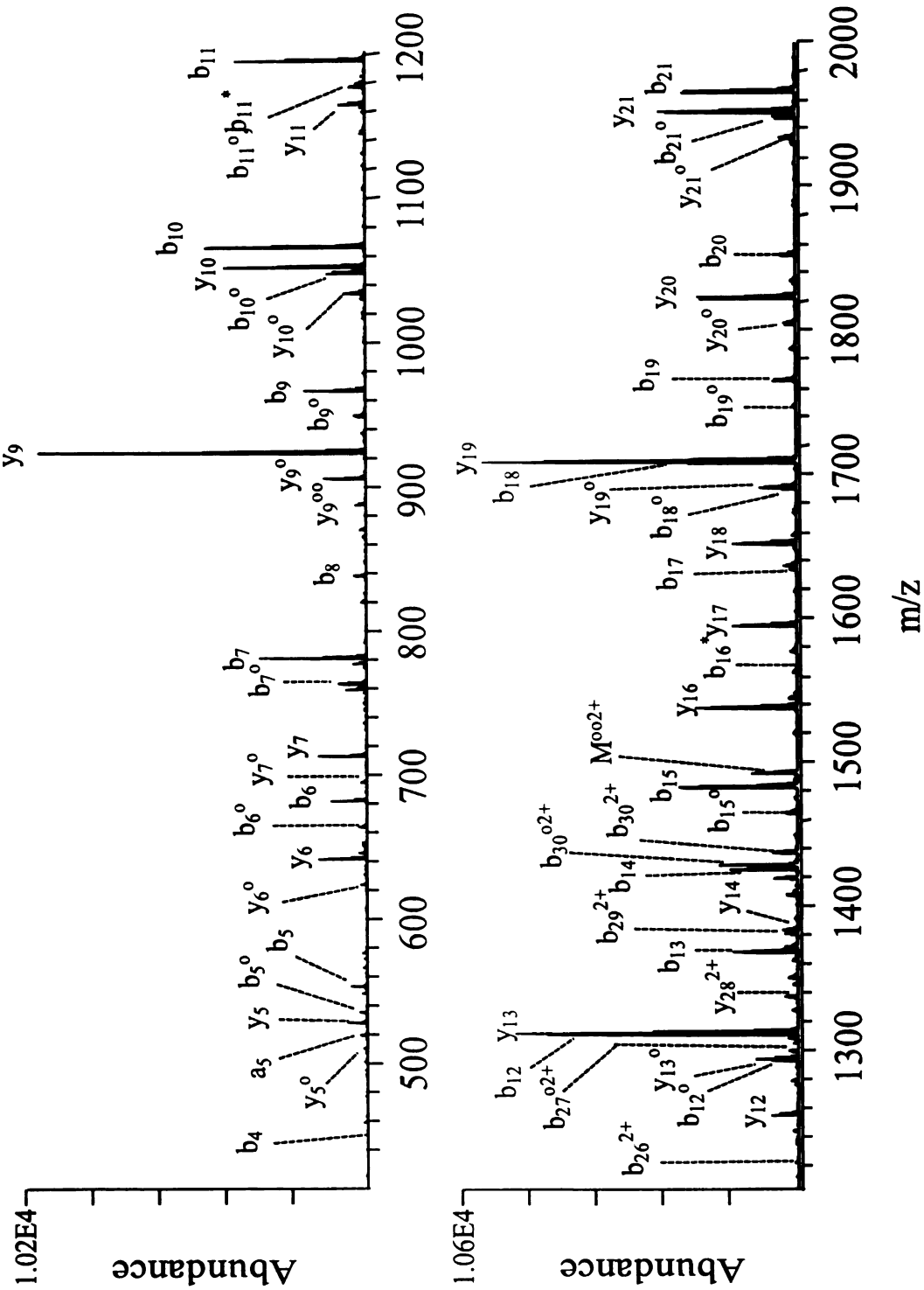

Figure 3.2: CID MS/MS Spectrum of the $[M+2H^+]^{2+}$ charge state (m/z = 1543.3) of C-peptide from Figure 3.1

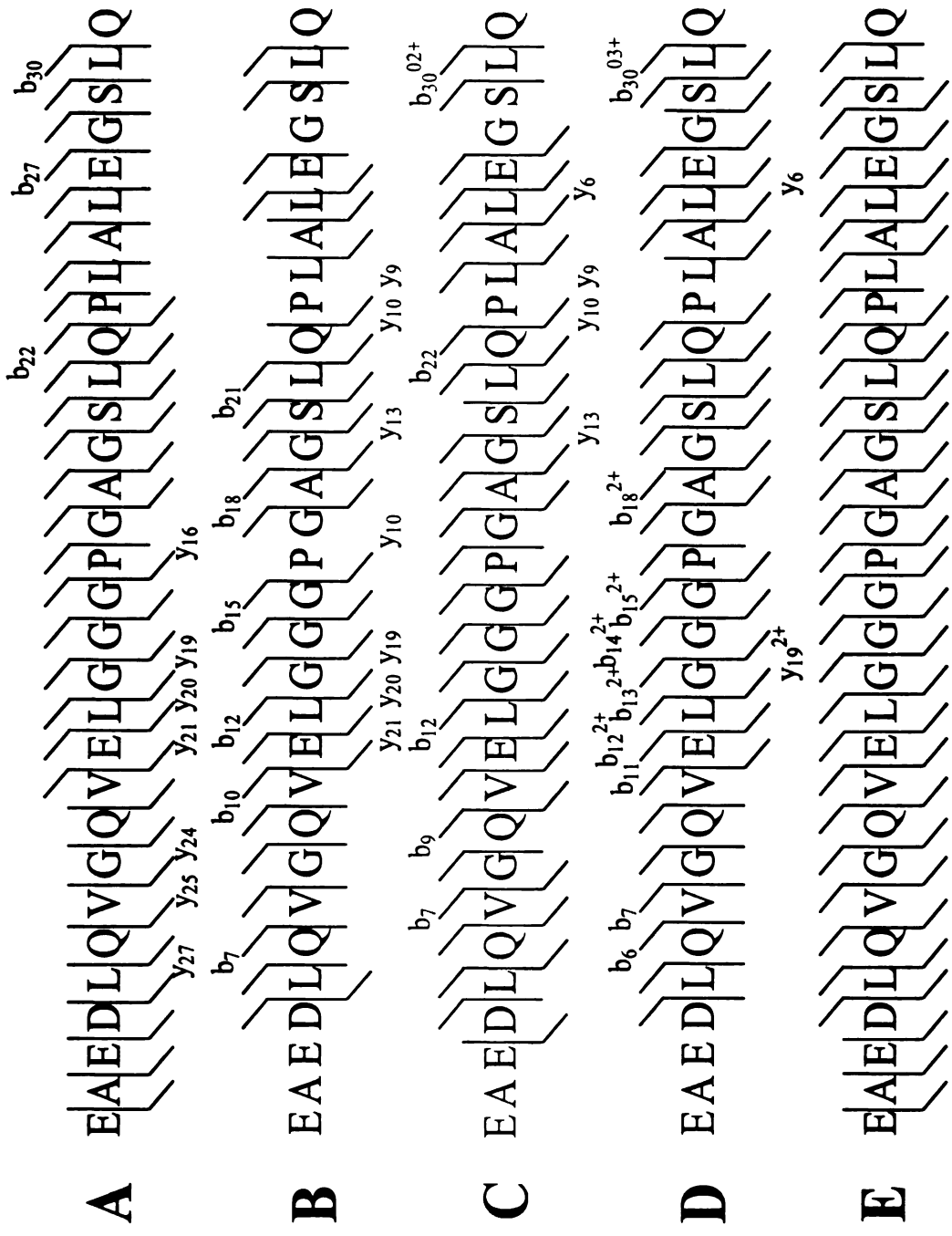

Figure 3.3: Product ion and sequence coverage summaries obtained from the CID spectra of the A) $[M+H^+]^+$, B) $[M+2H^+]^{2+}$, C) $[M+3H^+]^{3+}$, D) $[M+4H^+]^{4+}$, and E) combined product ion and sequence coverage summary for all charge states observed for C-peptide. The $[M+H^+]^+$ were acquired using MALDI while all others were acquired using ESI. Ions with a relative abundance greater than 25% are labeled on the summary.

3.2 Characterization of Proinsulin C-peptide Bound to Zn^{2+}

As mentioned in Chapter 1 above, C-peptide has previously been observed to bind to Zn^{2+}. Figure 3.4A shows the ESI mass spectrum of 10 μM C-peptide containing 10 μM $ZnCl_2$, obtained using the linear quadrupole ion trap mass spectrometer. Abundant ions corresponding to the doubly ($[M+Zn^{2+}]^{2+}$), triply ($[M+H^{+}+Zn^{2+}]^{3+}$) and quadruply ($[M+2H^{+}+Zn^{2+}]^{4+}$) charged precursor ions of Zn-bound C-peptide were all observed. Notably, ions corresponding to Na^{+} and K^{+} adducts were not observed. This was achieved by equilibrating the transfer line and ESI spray tip with 250 μL of a 10 μM $ZnCl_2$ solution before the sample was introduced.

In order to unambiguously identify the ions at m/z 1029.7 and m/z 1542.7 Da in Figure 3.4A as the Zn-bound $[M+H^{+}+Zn^{2+}]^{3+}$ and $[M+Zn^{2+}]^{2+}$ ions, respectively, high resolution 'UltraZoom' (28 m/z sec^{-1} resonance ejection scan rate)[79] scans were acquired for the two charge states, and are shown in Figure 3.4B and 3.4C, respectively. By observing the isotopic distributions for these ions and by comparison with the theoretical distributions for the Zn-bound C-peptide, it was found that the experimental results agreed with the theoretical distributions, thereby confirming the identity of the Zn-bound C-peptide.

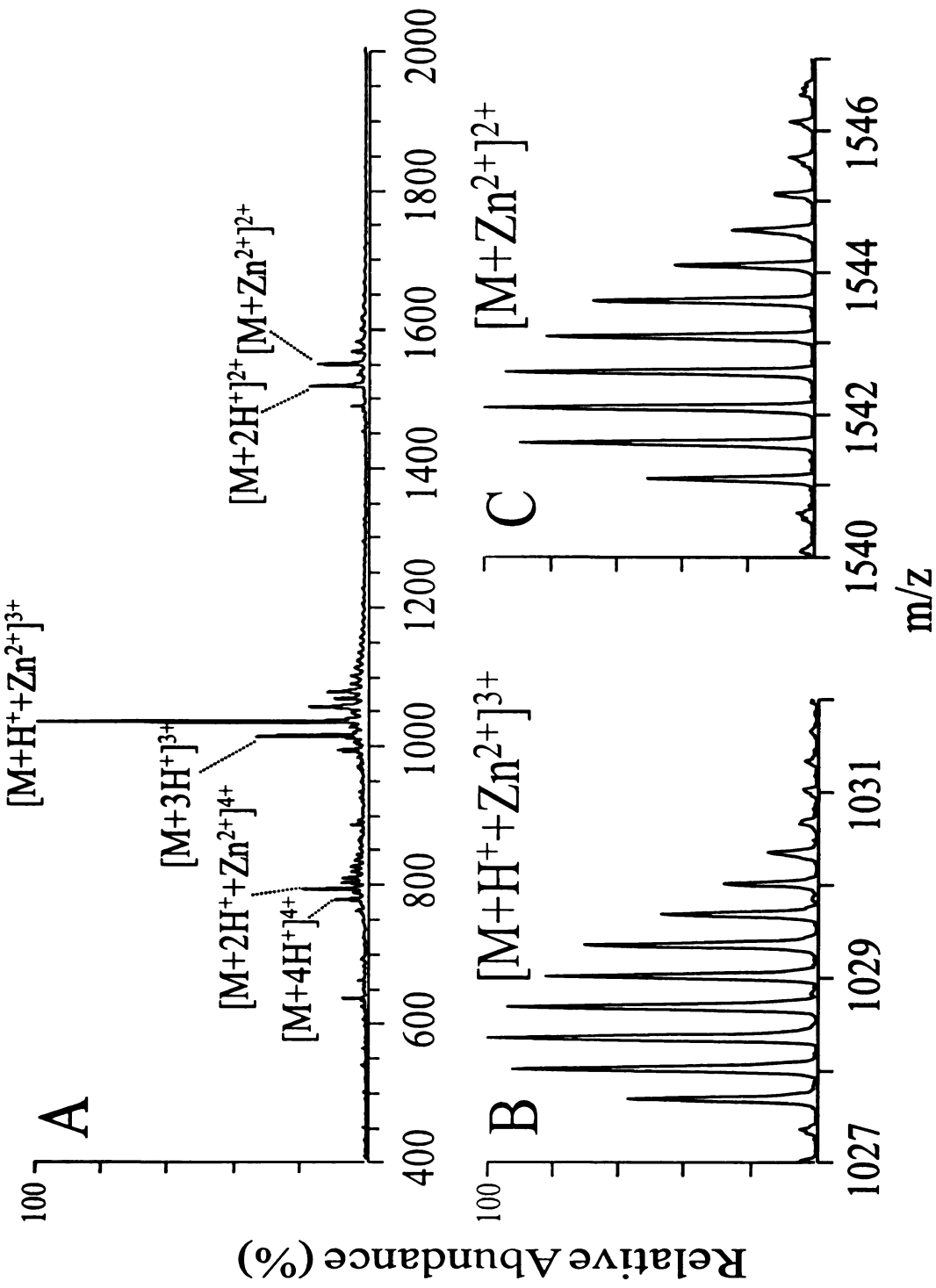

Figure 3.4: A) Mass spectrum of 10 μM C-peptide and 10 μM $ZnCl_2$ B) UltraZoom scan of the $[M+H^{+}+Zn^{2+}]^{3+}$ charge state C) UltraZoom scan of the $[M+Zn^{2+}]^{2+}$ charge state.

To characterize the metal-binding site(s) within the Zn-bound C-peptide, CID-MS/MS was then performed on the $[M+Zn^{2+}]^{2+}$, $[M+H^{+}+Zn^{2+}]^{3+}$ and $[M+2H^{+}+Zn^{2+}]^{4+}$ charge states. Figure 3.5 shows the MS/MS spectrum of the $[M+Zn^{2+}]^{2+}$ charge state. Figure 3.6 shows the product ion and sequence coverage summary for the $[M+Zn^{2+}]^{2+}$, $[M+H^{+}+Zn^{2+}]^{3+}$ and $[M+2H^{+}+Zn^{2+}]^{4+}$ charge states, as well as a combined product ion and sequence coverage summary. Ions above a relative abundance of 25% in Figure 3.3 are labeled in Figure 3.4. MS/MS spectra for the $[M+H^{+}+Zn^{2+}]^{3+}$ and $[M+2H^{+}+Zn^{2+}]^{4+}$ charge states are shown in the Supporting Information section as Figures S4 and S5, respectively.

For each of these spectra, the presence of Zn within a given product ion was assigned based on the observation of its characteristic isotope distribution. Similar to the spectrum of protonated C-peptide, the charge state of the product ions was first determined in order to determine the mass of the ion. Ions bound to Zn were identified by their characteristic isotopic distribution in the same manner as identifying the intact Zn-bound C-peptide precursor ions. Product ions that contain Zn were given in bold along with a † label.

The observation of product ions in both bound and unbound forms indicates that multiple populations of the Zn-bound C-peptide are present, suggesting that the Zn is not preferentially bound at any one specific site or region within the peptide sequence, making localization of the binding site difficult. This is also confirmed by the observation of Zn-bound product ions at both the N- and C-terminal regions of the

peptide. Another factor further confounding the ability to localize the metal binding site to a particular location is the number of fragment ions observed. Abundant product ions such as the y_9 and y_{19} ions present in the unbound MS/MS spectrum in Figure 3.2 are also present in Figure 3.5. As mentioned before, previous studies have found that fragmentation of metal-peptide complexes resulted in a decreased number of fragment ions, as the metal acts as a 'non-mobile' charge, which can direct the fragmentation to occur at the binding site(s). From the MS/MS spectra in Figure 3.5 and Figures S4 and S5, as well as Figure 3.6, however, almost complete sequence coverage was achieved, indicating a lack of a specific binding site for Zn^{2+} to C-peptide.

Despite the similarity of the two MS/MS spectra, some conclusions may be reached when examining the distribution of unbound, "mixed" (i.e. bound and unbound), and bound ions. Unbound sequence ions are observed to occur for small sequence ions, where binding is not observed to occur before the y_5 ion. Ions corresponding to cleavage in the middle region of the peptide appear to be mixed, while high mass sequence ions corresponding to cleavages near the termini of the peptide are observed as only Zn-bound ions. This would suggest roles of multiple residues in the binding of Zn.

Note that in the $[M+H^{+}+Zn^{2+}]^{3+}$ and $[M+2H^{+}+Zn^{2+}]^{4+}$ charge state product ion and sequence coverage summaries in Figure 3.6 the presence of y-type ions containing Zn were only observed for y_5 and above . The y_5 ion corresponds to cleavage at the N-terminal side of the Glu27 residue, which as discussed above has shown to have potential biological activity. The observation of bound y_5 and unbound y_4 ion would therefore

suggest that some binding is occurring at the Glu27 residue, which is consistent with the studies discussed previously showing that transition metals bind to deprotonated carboxylates of acidic amino acids.

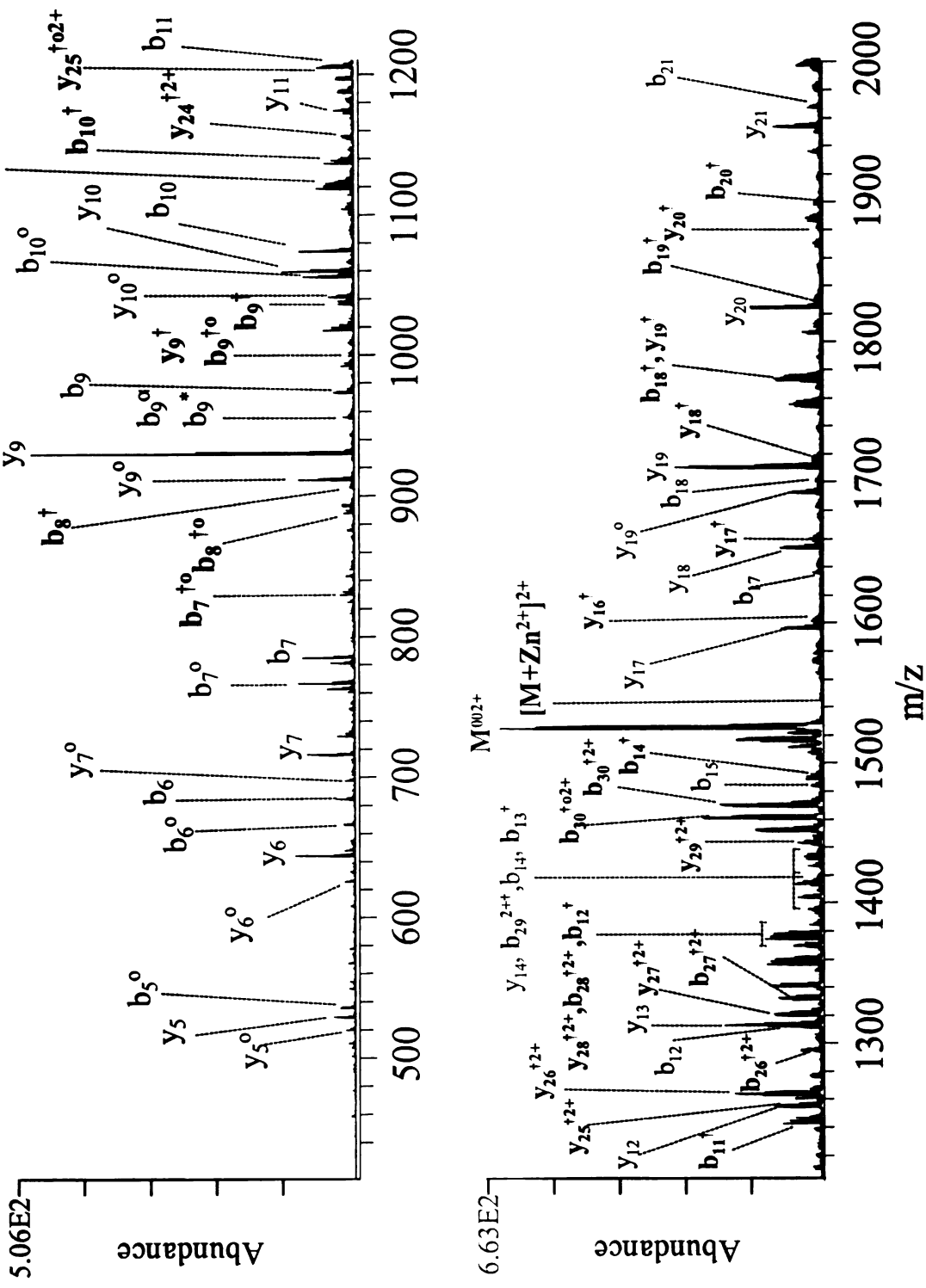

Figure 3.5: CID MS/MS Spectrum of the $[M+Zn^{2+}]^{2+}$ charge state (m/z = 1542.7) of C-peptide from Figure 4A. Ions observed to have Zn bound are labeled with † in bold.

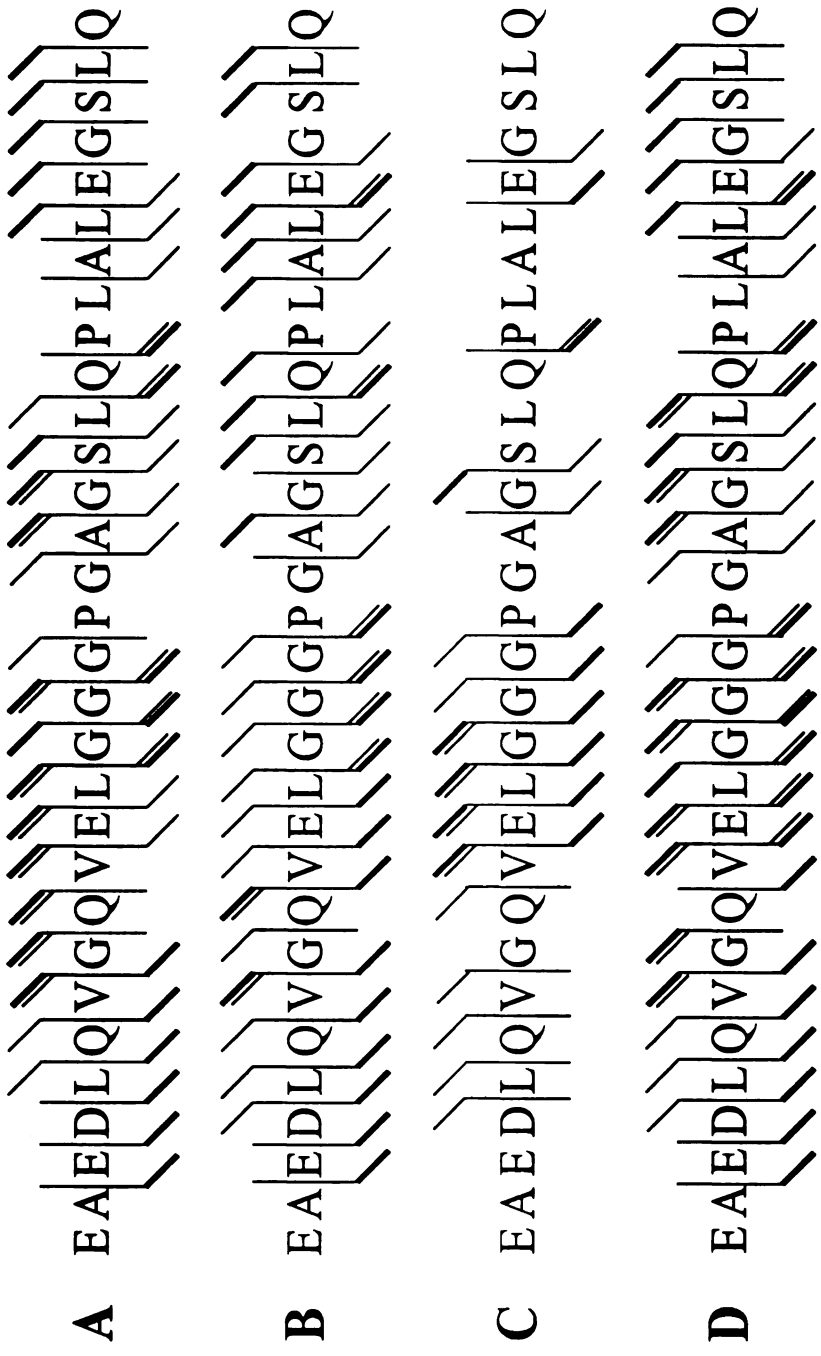

Figure 3.6: Product ion and sequence coverage summaries obtained from the CID spectra of the A) $[M+Zn^{2+}]^{2+}$, B) $[M+Zn^{2+}+H^{+}]^{3+}$, C) $[M+Zn^{2+}+2H^{+}]^{4}$ charge states of C-peptide as well as D) the overall product ion and sequence coverage summary. \ indicates an unbound b or y ion, \ indicates only the Zn-bound fragment was found, and \\ indicates that both bound and unbound ions were identified.

3.3 Top-down Characterization of the Proinsulin C-peptide Mutants

To gain a greater understanding of the effects of the potential residues involved in metal-binding to C-peptide, several single amino acid mutants were synthesized using solid-phase peptide synthesis. Each of the acidic glutamic acid and aspartic acid residues were individually replaced with alanine (termed E27A, E11A, D4A, E3A, and E1A) then the mutant peptides were first characterized in their protonated forms by CID-MS/MS, and compared to the data obtained from protonated C-peptide. A representative CID-MS/MS spectra for the $[M+2H^+]^{2+}$ charge state of the E27A mutant is given in Figure 3.7. The CID-MS/MS spectra acquired for the $[M+H^+]^+$ through $[M+4H^+]^{4+}$ charge states for each of the five mutants are provided in Figures S6 through S24. As with the wild type C-peptide, CID-MS/MS spectra for the singly protonated precursor were acquired using MALDI. A product ion and sequence coverage summary from the $[M+2H^+]^{2+}$ charge states for each of the five mutants is given in Figure 3.8. The overall product ion and sequence coverage summaries from the 3 observed charge states for each of the 5 mutants for is given in Figure S25. Product ions whose relative abundances were observed above 25% are labeled on the summaries. When compared to the MS/MS spectra of protonated C-peptide, the spectra for the mutants were all very similar, demonstrating that the presence of the single mutations did not significantly affect the fragmentation behavior. As with C-peptide, complete sequence information was obtained from each of the mutants.

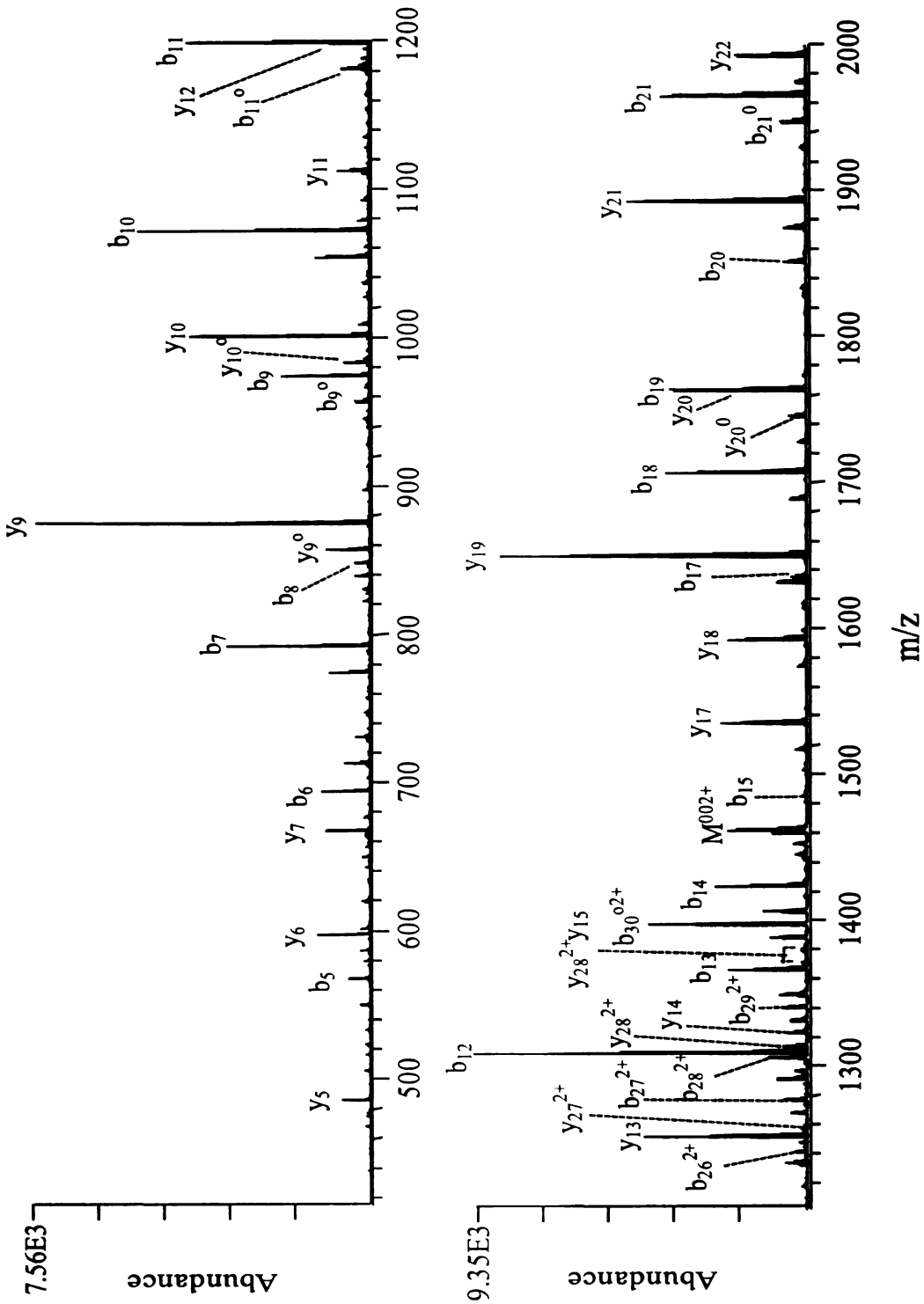

Figure 3.7: CID MS/MS Spectrum of the $[M+2H^{+}]^{2+}$ charge state (m/z = 1482.6) of E27A.

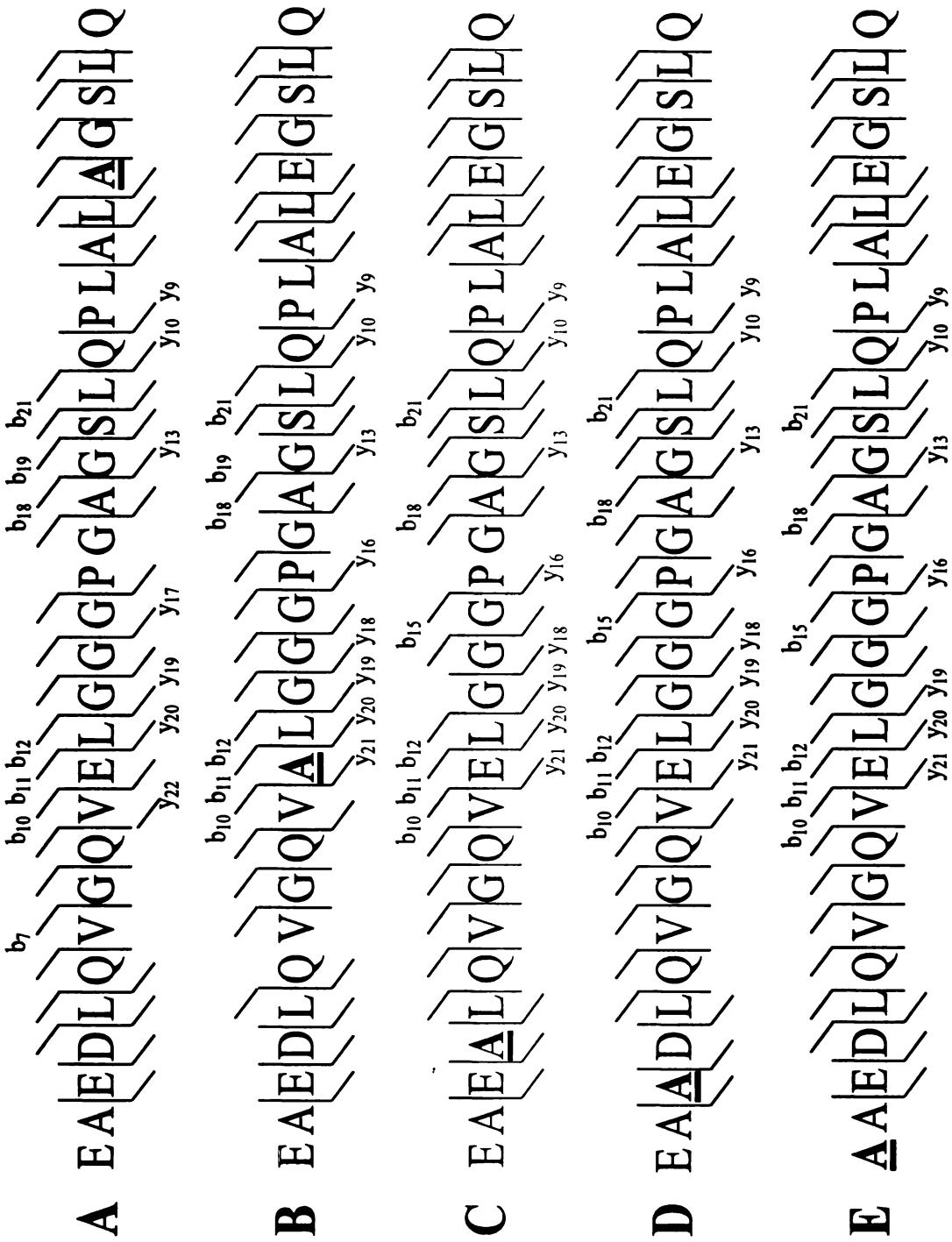

Figure 3.8: Product ion and sequence coverage summaries obtained from the CID spectra of the $[M+2H^{+}]^{2+}$ charge state of A) E27A, B) E11A, C) D4A, D) E3A, and E) E1A mutants of C-peptide. Ions with relative abundance greater than 25% are labelled on the summary.

3.4 Characterization of the Zn^{2+}-bound C-peptide Mutants

Identical to the method employed for analysis of the Zn-bound C-peptide, each of the five C-peptide single amino acid mutants were analyzed by ESI-MS in the presence of Zn. Figures 3.9 and 3.10 show the resultant ESI mass spectra obtained for the E27A, E11A, D4A, E3A, and E1A peptides.

Similar to the Zn-bound C-peptide spectrum in Figure 3.4A, the doubly ($[M+Zn^{2+}]^{2+}$), triply ($[M+H^{+}+Zn^{2+}]^{3+}$) and quadruply ($[M+2H^{+}+Zn^{2+}]^{4+}$) charged precursor ions were all abundant. Note that while the spectrum in 3.4A did not contain Na^{+} and K^{+} adducts, these adducts were all present in the C-peptide mutant spectra, albeit at variable abundance. This will be discussed later in this thesis in regard to the relative binding experiments.

CID-MS/MS spectra were then acquired to determine if the fragmentation behavior of the Zn-bound C-peptide was altered upon substitution of a single acidic residue, and whether this allows information to be obtained in regards to the metal binding. Ions were labeled using the same process as for the Zn-bound C-peptide experiment.

The MS/MS spectrum for the $[M+Zn^{2+}]^{2+}$ charge state of the E27A mutant is shown in Figure 3.11. The MS/MS spectra for the $[M+H^{+}+Zn^{2+}]^{3+}$ and $[M+2H^{+}+Zn^{2+}]^{4+}$ charge states are shown in Figures S26 and S27, respectively. Figure 3.12 shows the product ion and sequence coverage summary for the $[M+Zn^{2+}]^{2+}$, $[M+H^{+}+Zn^{2+}]^{3+}$ and $[M+2H^{+}+Zn^{2+}]^{4+}$ charge states, as well as a combined product ion

and sequence coverage summary for the E27A mutant. Figures S28 through S39 contain the MS/MS spectra for the $[M+Zn^{2+}]^{2+}$ through $[M+2H^{+}+Zn^{2+}]^{4+}$ charge states of the remaining four mutants. A product ion and sequence coverage summary for the $[M+Zn^{2+}]^{2+}$ charge state for the remaining four mutants is given in Figure 3.13. Overall product ion and sequence coverage summaries for the four remaining mutants are given in Figure S40.

When comparing the MS/MS spectra for C-peptide in Figure 3.5 and that for the E27A mutant in Figure 3.11, there are many similarities. The y_9 ion corresponding to cleavage N-terminal to proline is dominant in both cases, as is the Zn-bound b_{30} ion. The overall sequence coverages are similar, and when examining the distribution of bound and unbound sequence ions, a similar pattern was observed to that of C-peptide.

Another measure of the similarity of the binding was obtained by examination of the ratio of bound: unbound intensities for dominant ions. When looking at the y_9 ion, for example, the unbound ion is dominant in all cases, with the Zn bound ion occurring at low intensities. These ratios remain consistent for similar charge states of C-peptide and E27A.

One main difference however, is the lack of a Zn-bound y_5 ion in any of the spectra of the E27A mutant. This ion was observed in the $[M+H^{+}+Zn^{2+}]^{3+}$ and $[M+2H^{+}+Zn^{2+}]^{4+}$ MS/MS spectra of C-peptide, although at low abundance. The lack of binding on the N-terminal region of E27A suggests a role for Zn binding of the Glu27 residue.

When comparing the mutant spectra with each other, again, there were again very few differences. Similar dominant product ions as well as binding ratios of the y_9 ions indicated that one amino acid does not play a crucial role to the binding of Zn. Again, 'bound' sequence ions at both the N- and C-terminal region of the sequences were observed, indicating non-specific binding.

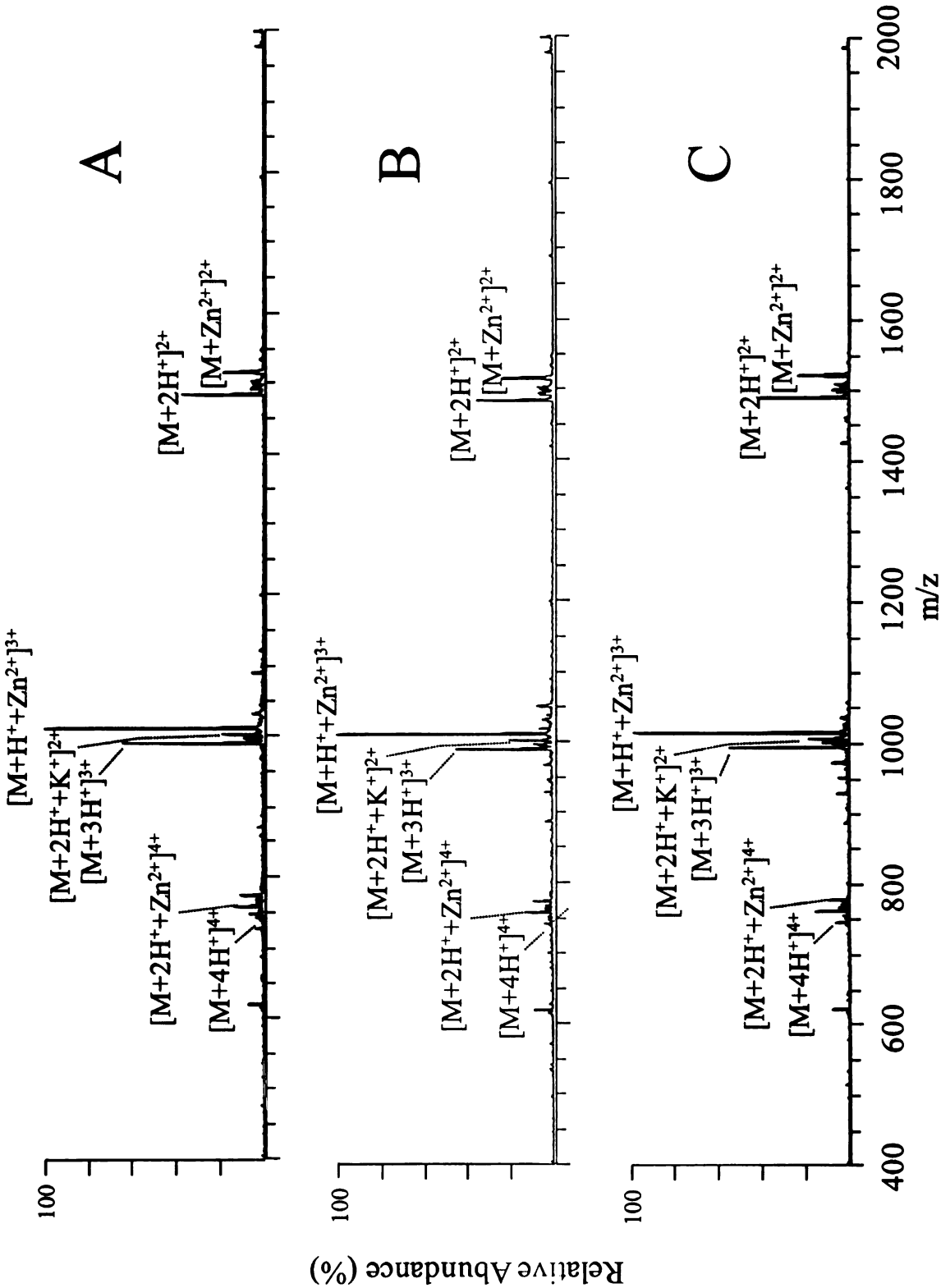

Figure 3.9: ESI mass spectra of 10μM $ZnCl_2$ and 10μM A) E27A, B) E11A, C) D4A in H_2O

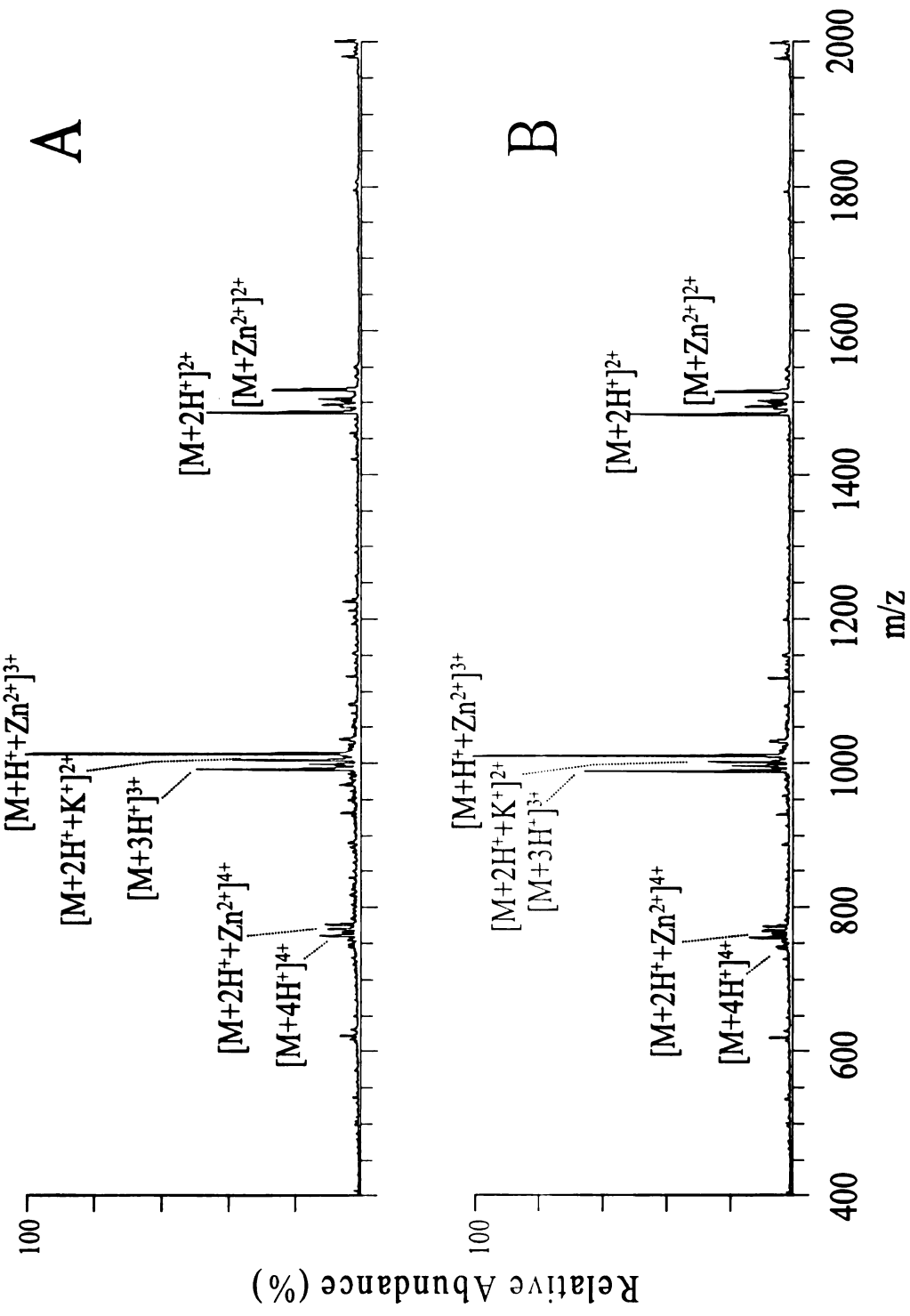

Figure 3.10: ESI mass spectra of 10μM $ZnCl_2$ and 10μM A) E3A and B) E1A in H_2O

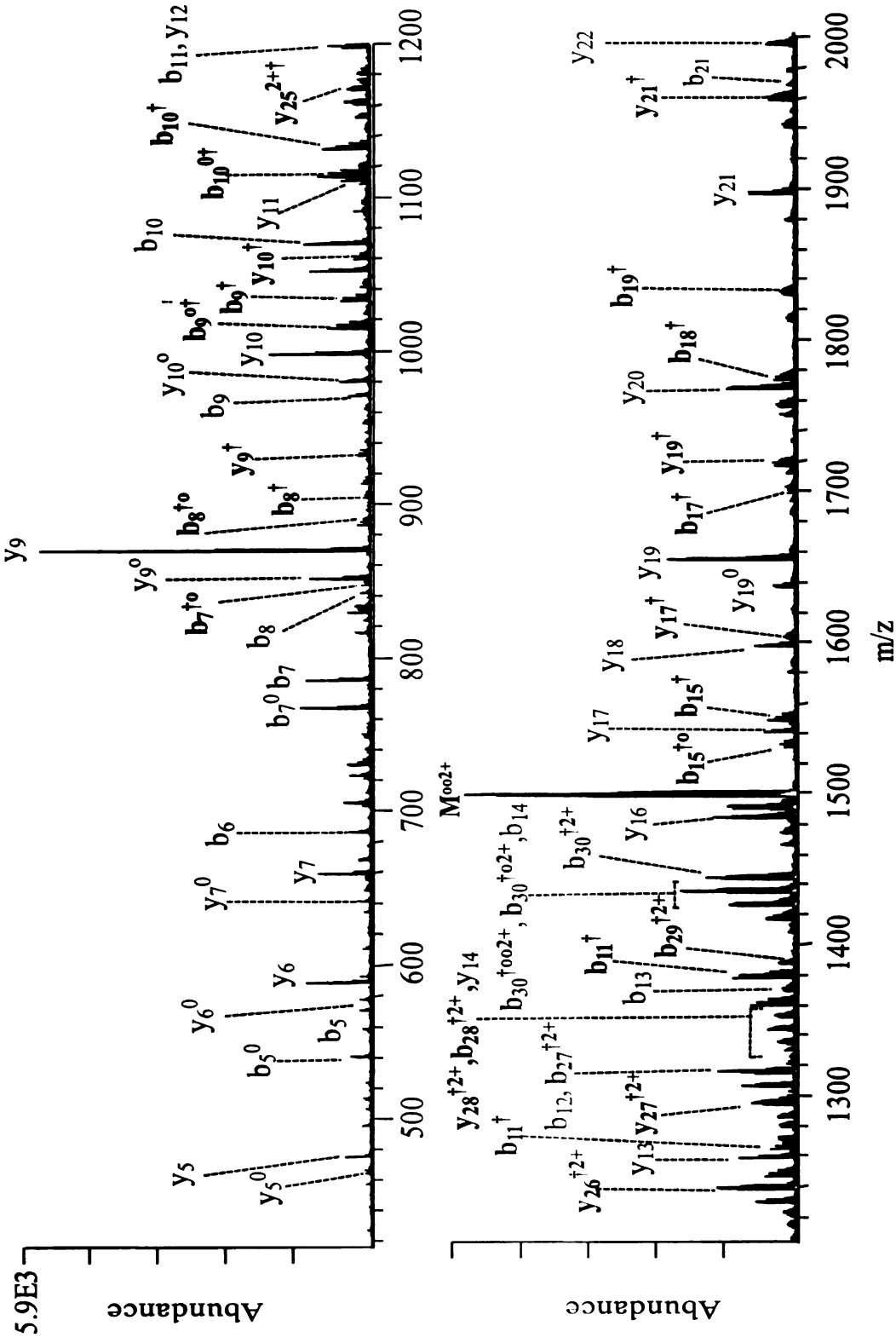

Figure 3.11: CID MS/MS Spectrum of the $[M+Zn^{2+}]^{2+}$ charge state (m/z = 1514.44) of the E27A mutant of C-peptide from Figure 9A.

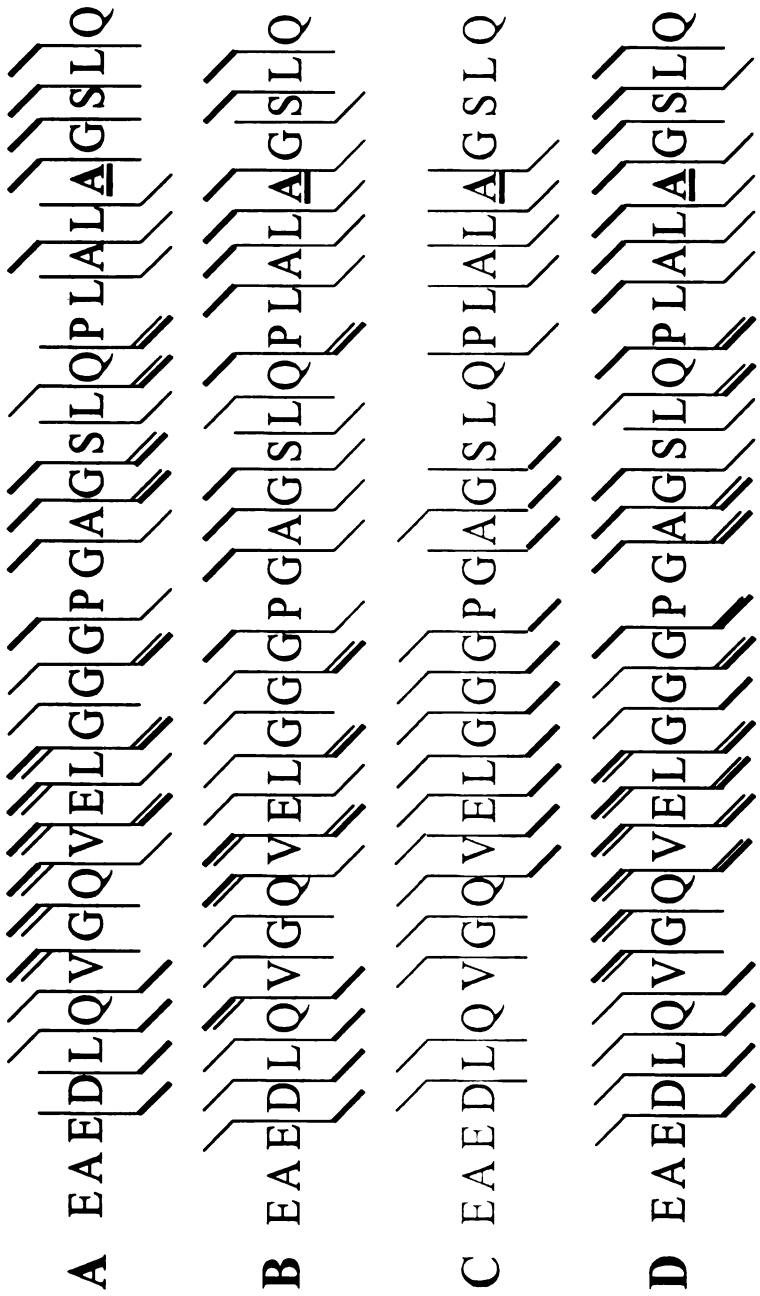

Figure 3.12: Product ion and sequence coverage summaries obtained from the CID spectra of the A) $[M+Zn^{2+}]^{2+}$, B) $[M+Zn^{2+}+H^{+}]^{3+}$, C) $[M+Zn^{2+}+2H^{+}]^{4}$ charge states of E27A as well as D) the overall product ion and sequence coverage summary. \ indicates an unbound b or y ion, \ indicates only the Zn-bound fragment was found, and \ indicates that both bound and unbound ions were identified.

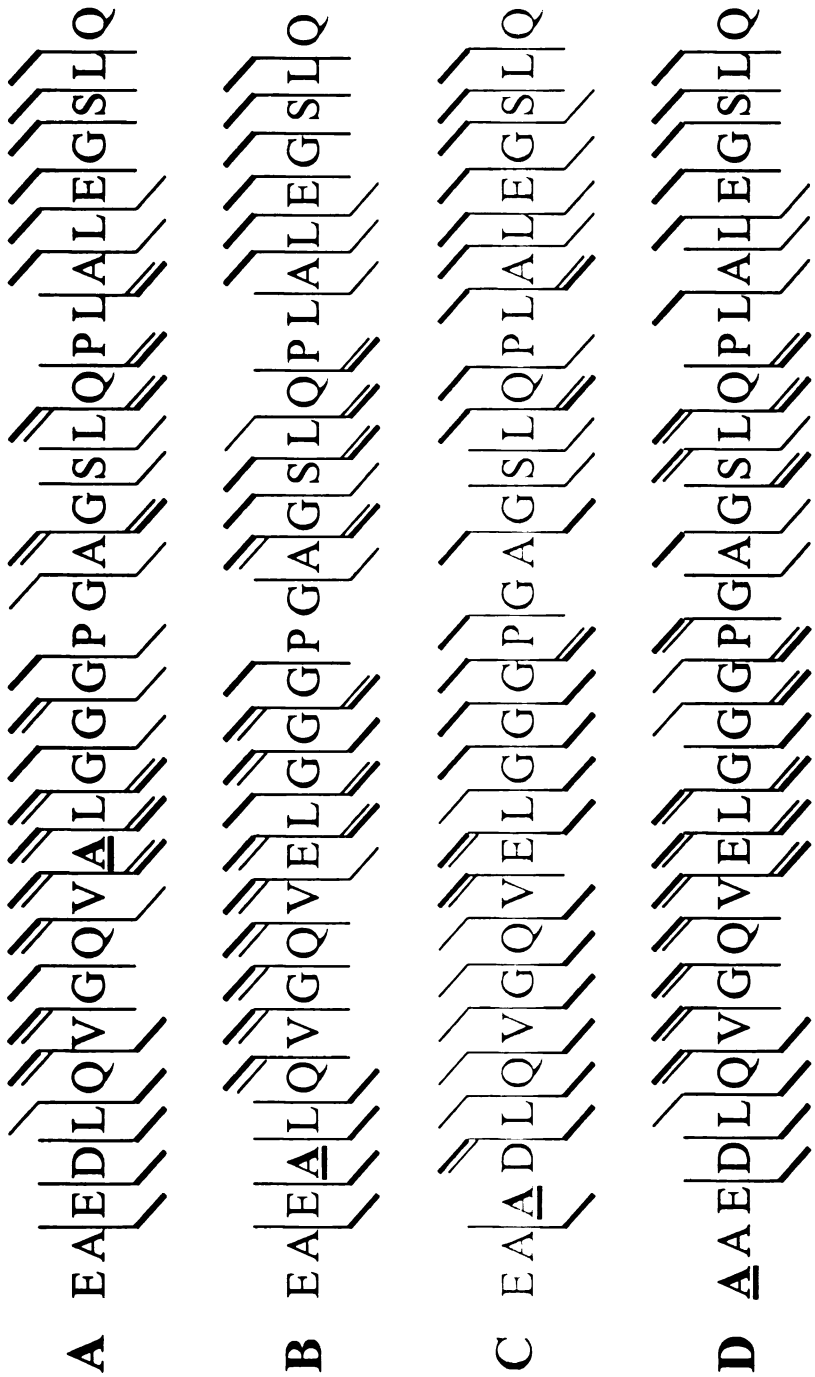

Figure 3.13: Product ion and sequence coverage summaries obtained from the CID spectra of the $[M+Zn^{2+}]^{2+}$ charge state of A) E11A, B) D4A, C) E3A and D) E1A mutants of C-peptide. \ indicates an unbound b or y ion, \ indicates only the Zn-bound fragment was found, and // indicates that both bound and unbound ions were identified.

3.5 Effect of Amino Acid Mutations on the Relative Binding of Zn^{2+} to C-peptide

While it has been shown that substitution of a potentially metal-binding amino acid has little to no effect on the fragmentation behavior of C-peptide, it is possible that elimination of one of these residues could play a role in the amount of Zn that the peptide can bind, thereby providing information regarding the residues that are important to C-peptide metal interactions. Therefore, ESI-MS spectra were acquired in triplicate for each of the C-peptide mutants in the presence of one molar equivalent of Zn^{2+}. Representative spectra for each peptide are shown in Figure 3.4A for the C-peptide and in Figures 3.9A-C and 3.10 A-B for the mutants. Compared to the wild-type C-peptide spectrum in Figure 3.4A, where no Na^+ or K^+ adduct ions were observed in the spectrum, Na^+ or K^+ adducts of variable abundance were observed in the spectra from the mutants in Figures 3.9and 3.10, indicating a lower affinity for Zn^{2+} for these mutants.

To quantitatively measure the amount of Zn binding for the C-peptide versus the mutants, a ratio of bound: unbound can be calculated from each spectrum. This was performed by summing the intensities of each of the charge states observed for the ions containing Zn, and dividing by the summed intensities of the charge states observed for the unbound ions (Figure 3.14A). Also, to account for the presence of the Na^+ and K^+ salt adducts in the mutant peptide spectra, a modified bound: unbound ratio was calculated after summing the intensities of the salt adduct peaks with the unbound ions Figure 3.14B). It can be seen from Figure 3.14 that an approximate 50% decrease in the amount of Zn binding was observed in each of the mutants compared to the wild-type C-

peptide. Thus, while mutation of any individual acidic residue results in a decrease in Zn binding, it appears that no specific acidic residue is critical. This is consistent with the MS/MS data which demonstrated that the fragmentation behavior did not change upon substitution of a single acidic residue.

Previous activity studies conducted on C-peptide have been performed using equimolar concentrations of C-peptide and Zn^{2+} in the nanomolar range. The mass spectrometry studies conducted here were performed using 10 μM concentrations of both C-peptide and Zn^{2+}. In an effort to examine any concentration dependence on the site of binding in C31 and the E27A mutant, as well as the relative binding of Zn^{2+}, ESI-MS and ESI-MS/MS experiments were conducted on the full length C-peptide and E27A mutants at 1 μM concentrations (data not shown). The MS spectra were essentially identical, suggesting that a 10-fold decrease in the concentration did not significantly affect the site of Zn^{2+} binding. Results from a relative binding experiment (data not shown) showed an overall decrease in the amount of Zn^{2+} binding at the 1 μM conecntration, although the relative binding ratios of C-peptide : E27A between the 10 μM samples and 1 μM samples remained relatively constant. This suggested that a decrease in concentration did not affect the relative binding.

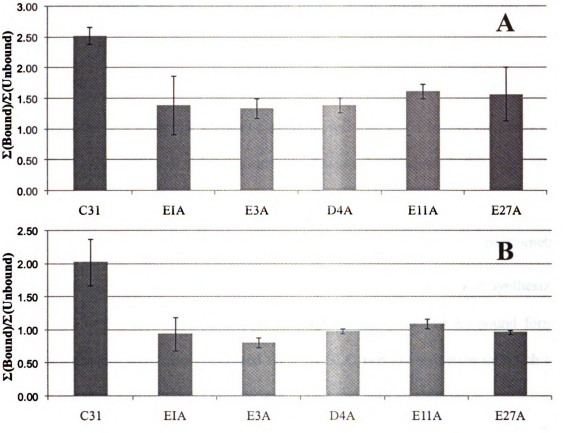

Figure 3.14: Plot showing binding ratios of the $[M+Zn^{2+}+nH^{+}]^{(n+2)+}$ to $[M+nH]^{n+}$ for C-peptide and the 5 mutants A) Not accounting for $[M+Na]^{+}$ and $[M+K]^{+}$ adducts and B) accounting for the $[M+Na]^{+}$ and $[M+K]^{+}$ adducts. Intensities for the 2+, 3+, and 4+ charge states were summed. Standard deviations for the triplicate measurements are shown on the plot.

3.6 Characterization and Activity Studies of the C-terminal Pentapeptide of C-peptide

In order to more closely examine the effect of a single acidic residue on Zn^{2+} binding and activity, a c-peptide segment containing residues 27-31 (i.e. in the absence of the other four acidic residues) was examined. As discussed in Chapter 1, this fragment of the C-peptide sequence has been shown to exhibit biological activity, and requires the presence of the Glu27 residue.[14, 31] Thus, as an extension of the mass spectrometric binding characterization studies described above, the EGSLQ peptide was synthesized and subjected to MS and MS/MS analysis in both its unbound and Zn-bound forms. Similar experiments were also conducted on a AGSLQ peptide sequence in which the previously reported critical Glu27 residue was substituted with an alanine.

ESI-MS spectra for the EGSLQ and AGSLQ peptides in the presence of 10 uM Zn are shown in Figures 3.15A and 3.15B, respectively. From these spectra, it can be seen that there is a dramatic decrease in the amount of binding as compared with C-peptide and the full length single amino acid mutants. This is likely a result of a decreased number of locations for Zn binding, as the EGSLQ peptide contains only a single acidic residue. While triplicate experiments were not conducted, decreased binding was observed for the AGSLQ peptide, consistent with that expected due to the lack of an acidic residue. Note however, that the C-terminal carboxylate group is available for binding in both peptides.

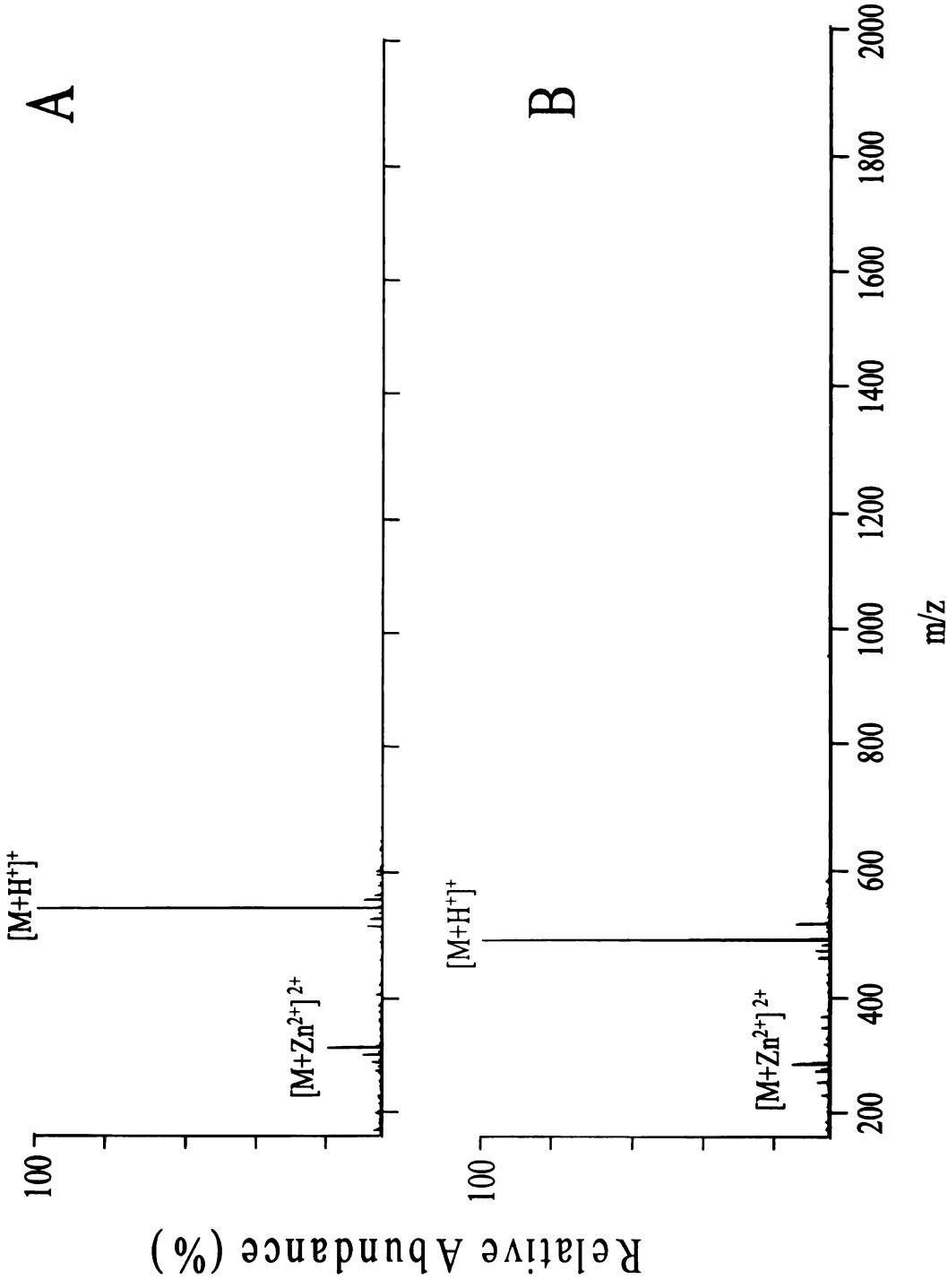

Figure 3.15: ESI mass spectra for 10 μM Zn^{2+} and 10 μM A) EGSLQ and B) AGSLQ.

CID-MS/MS spectra from the $[M+Zn^{2+}]^{2+}$ precursor ions of the EGSLQ and AGSLQ peptides are shown in Figures 3.16A and 3.16B, respectively. Limited sequence information was observed for both peptides. Dominant product ions corresponding to the neutral losses of water (labeled as $M^{\dagger\circ 2+}$ and $M^{\dagger\circ\circ 2+}$) were observed in both spectra. This is similar to the full-length peptides.

Examination of the other dominant ions in the CID-MS/MS spectra in Figure 3.16 allow for insights into the binding properties of this peptide. In the MS/MS spectrum of EGSLQ, the Zn-bound b_4 and unbound y_1 ion are dominant. These two ions correspond to cleavage at the same bond: the Leu/Gln amide bond. The Zn-bound b_4 ion indicates that Zn is retained on the N-terminal region of the peptide. This end contains the potentially-critical Glu27 residue, which from earlier experiments on the full-length single amino acid mutants was implicated in the Zn-binding. In the spectrum of AGSLQ in Figure 3.16B, this ion pair is much less dominant. Instead, there is a dominant bound-y_3/ unbound-b_2 ion pair. This corresponds to cleavage of the Gly/Ser bond, where the Zn is retained on the C-terminal region. This could indicate that binding is occurring at the C-terminal carboxylate of the peptide or at the side chain hydroxyl group of the Ser or at a carbonyl oxygen of the amide backbone. Also of note is the presence of the bound-b_4 /unbound-y_1 pair in the spectrum of AGSLQ is observed, albeit at much lower abundance compared to their abundance in the spectrum of EGSLQ. As there are no acidic residues to bind Zn in the b_4 fragment, which would again implicate Zn binding involving the carbonyl oxygens or the Ser residue.

The ratio of the b_4/y_1 pair to the y_3/b_2 pair indicates a measure of the competition for the Zn at the N- and C- termini for each peptide. The spectrum of EGSLQ contains the y_3/b_2 pair at only minor abundance, indicating a much weaker competition of the C-terminal carboxylate for Zn. The y_3/b_2 pair for AGSLQ is present at a much higher abundance, indicating a greater affinity of the Zn to the C-terminal carboxylate.

Zn^{2+} has been shown to exhibit tetrahedral coordination geometry in proteins[83]. These structures were based on solution-phase calculations where water molecules aid in the stabilization of the metal. In the case of EGSLQ, there are only two main sites for the Zn to interact, and because a gas-phase ion is being measured, no water molecules are available to interact with the Zn. Studies conducted using Cr^{3+} on acidic peptides have proposed two-coordinate gas-phase complexes,[59] which would suggest a similar geometry for the gas-phase EGSLQ-Zn^{2+} complexes. The AGSLQ peptide only has one carboxylate group, and as mentioned before the Ser residue or possibly the amide carbonyl groups could aid in the stabilization.

While the binding data on the single amino acid mutants and the results from the EGSLQ fragment indicate a role for the Glu27 residue in the binding of Zn^{2+} to C-peptide, it is necessary to correlate these results with a specific biological activity. Thus, similar ATP release experiments to those performed on Zn-activated full length C-peptide described in Chapter 1, were performed using the EGSLQ and AGSLQ peptides (these data were provided by Ms Jennifer Meyer and Prof. Dana Spence).

ATP release experiments were performed using a luciferin/luciferase chemiluminescence assay.[47] Rabbit erythrocytes were incubated for two hours with an appropriate volume of 8.3 μM stock solution of peptide and $ZnCl_2$ in a physiological salt solution to yield a final peptide and Zn^{2+} concentration of 10 nM. Chemiluminesence was measured using a photomultiplier tube (PMT). Figure 3.17 shows the summary of the ATP release data with n = 7, and statistical significance was calculated using a single-sided students t-test with p = 0.025

Incubation of the erythrocytes with the EGSLQ peptide in the presence of Zn resulted in a greater than 100% increase in ATP release. Notably, this was statistically equivalent to the ATP released upon incubation of the erythrocytes with the full-length C-peptide. The AGSLQ mutant, however, showed no increase in ATP release activity over the control level. These data are therefore consistent with the mass spectrometry results described above, that indicate a possible role of the Glu27 residue in Zn binding.

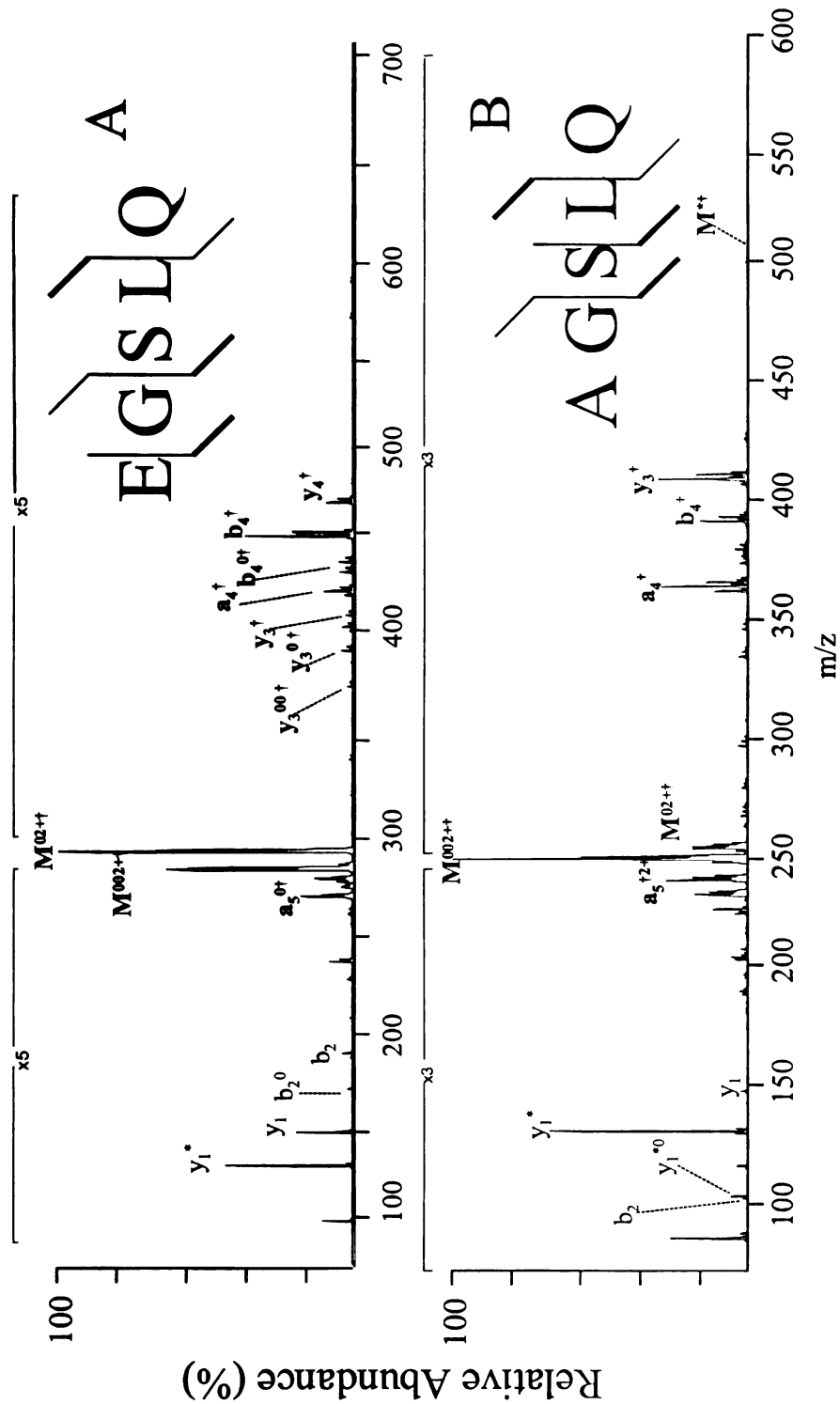

Figure 3.16: CID-MS/MS spectra of the $[M+Zn^{2+}]^{2+}$ precursor ions of A) EGSLQ and B) AGSLQ.

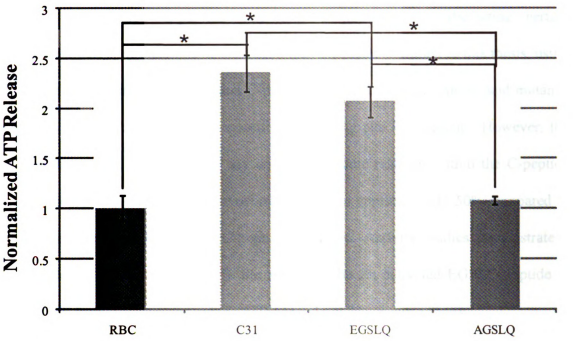

Figure 3.17: Bar graph showing Normalized ATP relase in erythrocytes for C-peptide as well as the EGSLQ pentapeptide and the AGSLQ mutant. Measurements were taken with n = 7, and error bars are plotted as the standard error of the mean. A * indicates a statistically significant difference was calculated using a single sided students t-test (p = 0.025).

3.7 Conclusions and Future Directions

It has been demonstrated that proinsulin C-peptide has the ability to bind Zn^{2+}, and that Zn-activated C-peptide may play a key role in alleviating certain microvasculature complications of diabetes. From the results outlined in this thesis, using MS and MS/MS analysis of Zn bound C-peptide and various single amino acid mutants, as well as C-peptide segments, no specific Zn binding site is apparent. However, the results indicate that elimination of any one of the acidic residues within the C-peptide sequence results in a decrease in the overall binding to approximately 50% compared to that of the wild type full length C-peptide sequence. Activity studies demonstrate a critical role for the Glu27 residue in the ability of the Zn activated EGSLQ peptide to release ATP from erythrocytes, where AGSLQ did not return any activity.

Future work should include activity measurements on the single amino acid mutations synthesized for the binding experiments. This will allow for a correlation between the activity and Zn-binding for full-length peptides, as opposed to the C-terminal pentapeptide fragment. While the Glu27 residue has shown to be active in the segment, it has not yet been demonstrated that elimination of this residue in the full length sequence has any effect on the activity of the peptide. Since it is clear from the experiments performed that substitution of one acidic residue does not eliminate the Zn-binding, synthesis of peptides containing multiple mutations of the acidic residues will need to be performed. This will allow for a greater understanding of the peptide-metal interactions. Synthesis of peptides containing four mutations will allow for the effect of a single acidic residue in the full length sequence to be studied.

SUPPORTING INFORMATION

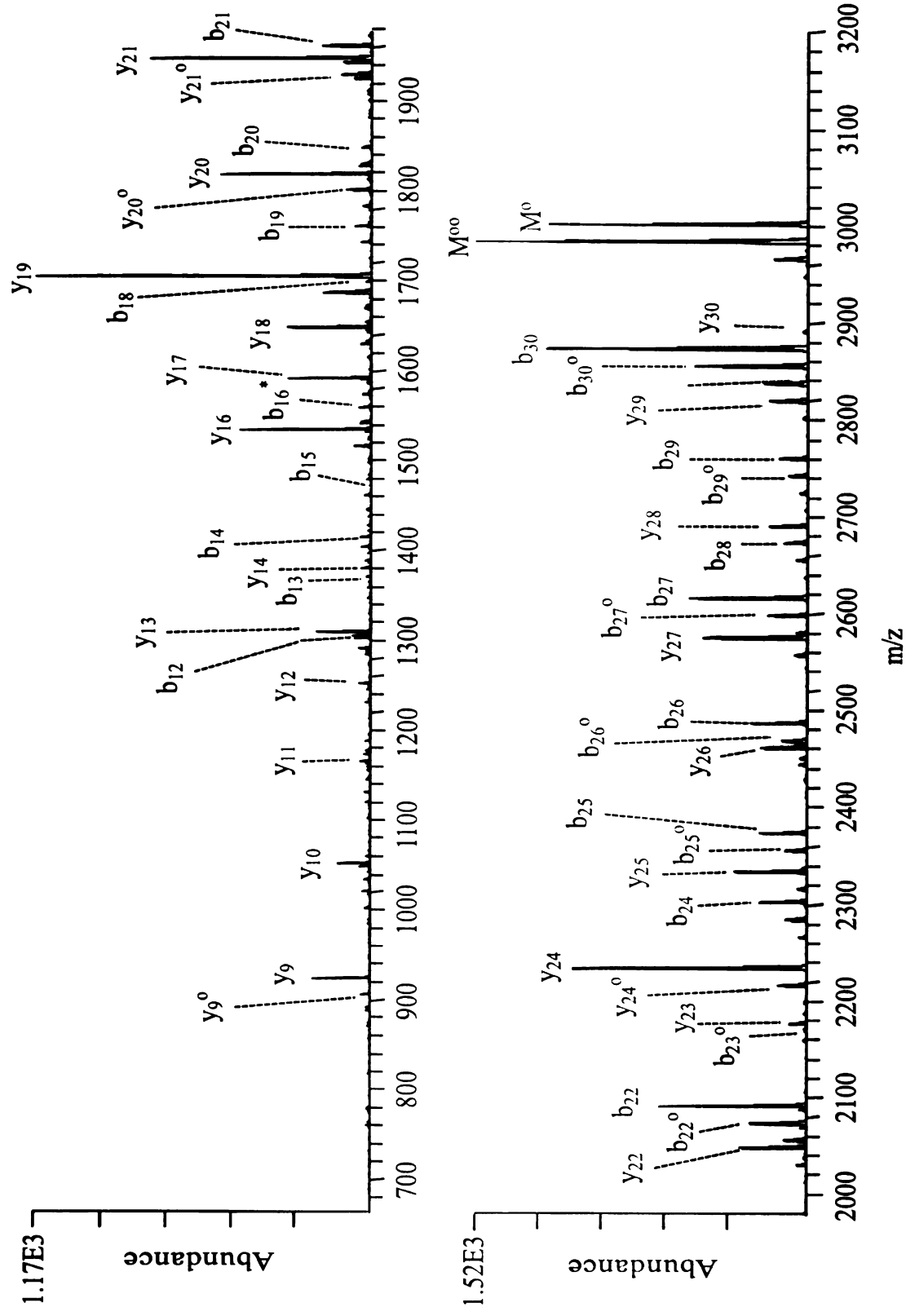

Figure S1: MALDI CID MS/MS Spectrum of the $[M+H^{+}]^{+}$ charge state (m/z = 3021.3) of C-peptide

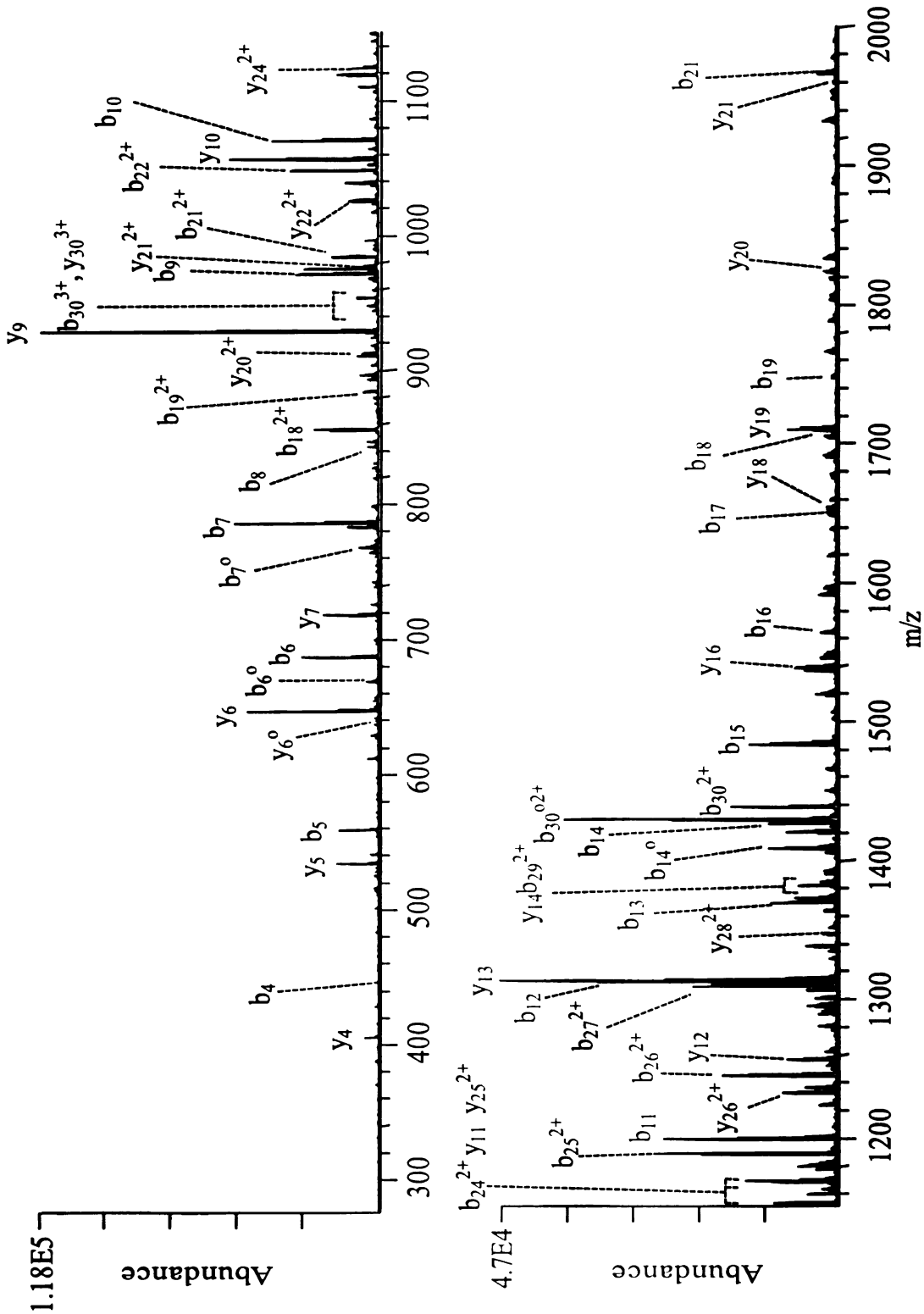

Figure S2: CID MS/MS Spectrum of the $[M+3H^+]^{3+}$ charge state (m/z = 1007.6) of C-peptide

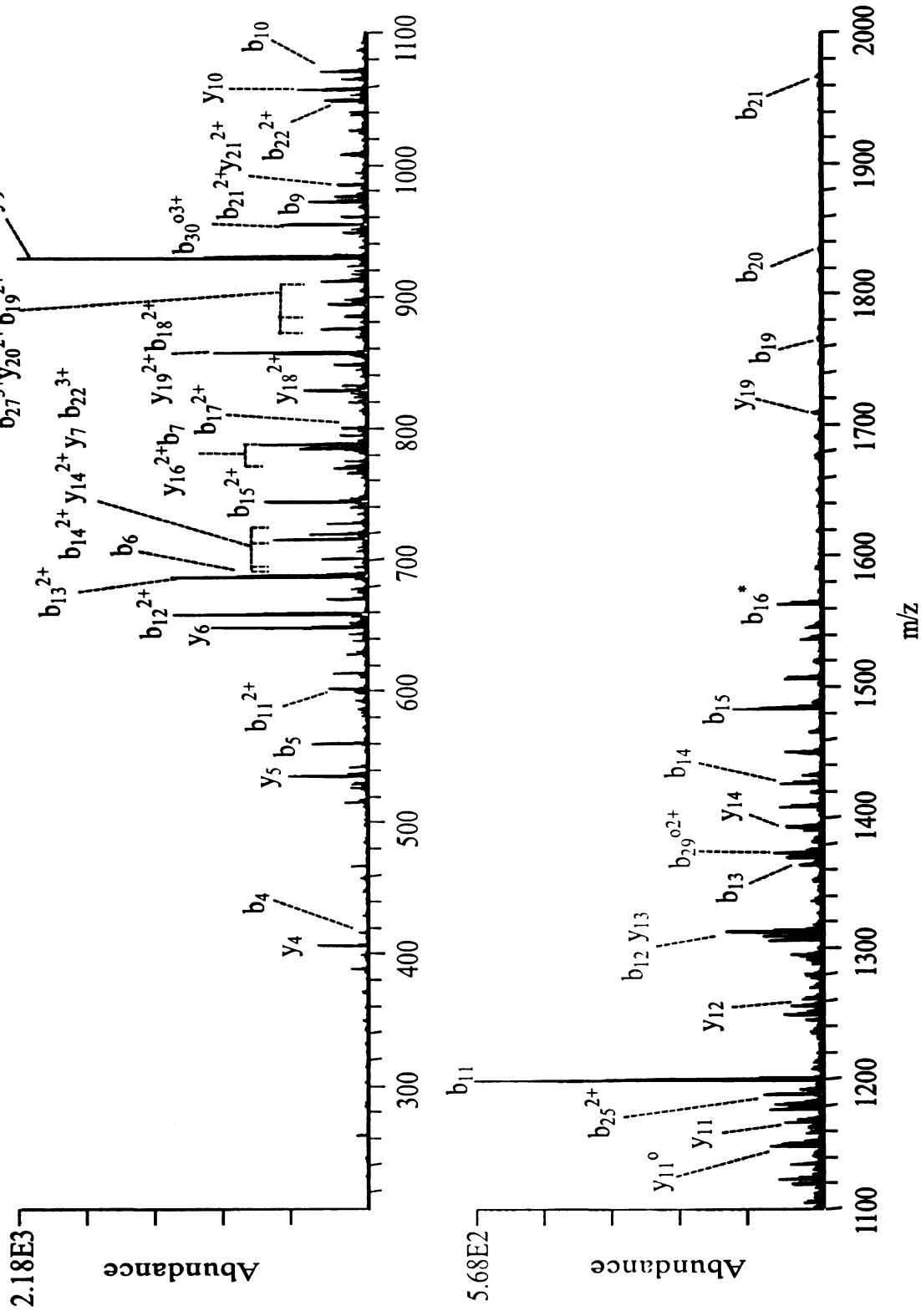

Figure S3: CID MS/MS Spectrum of the $[M+4H^+]^{4+}$ charge state (m/z = 756.0) of C-peptide

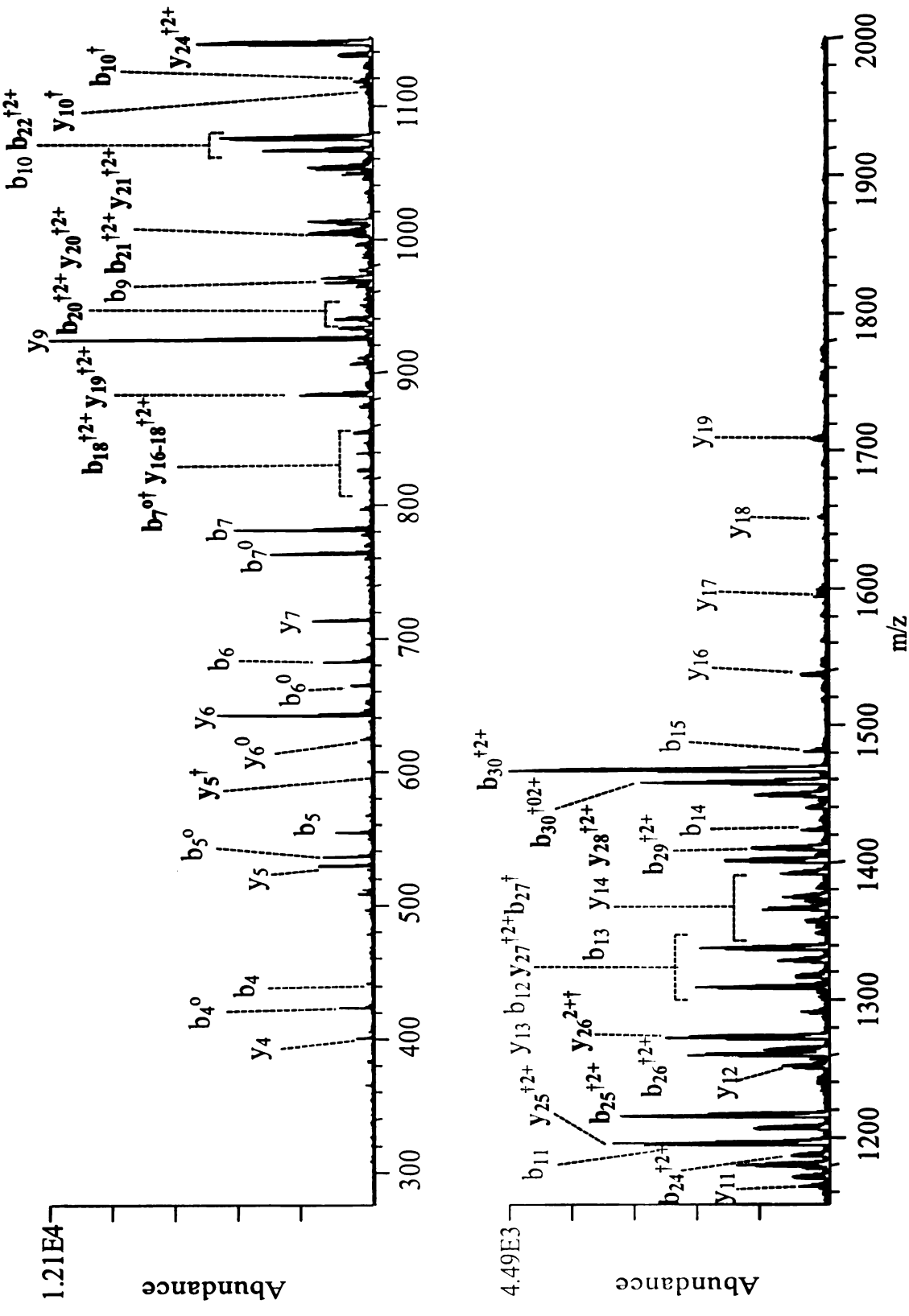

Figure S4: CID MS/MS Spectrum of the $[M+Zn^{2+}+H^{+}]^{3+}$ charge state (m/z = 1007.6) of C-peptide

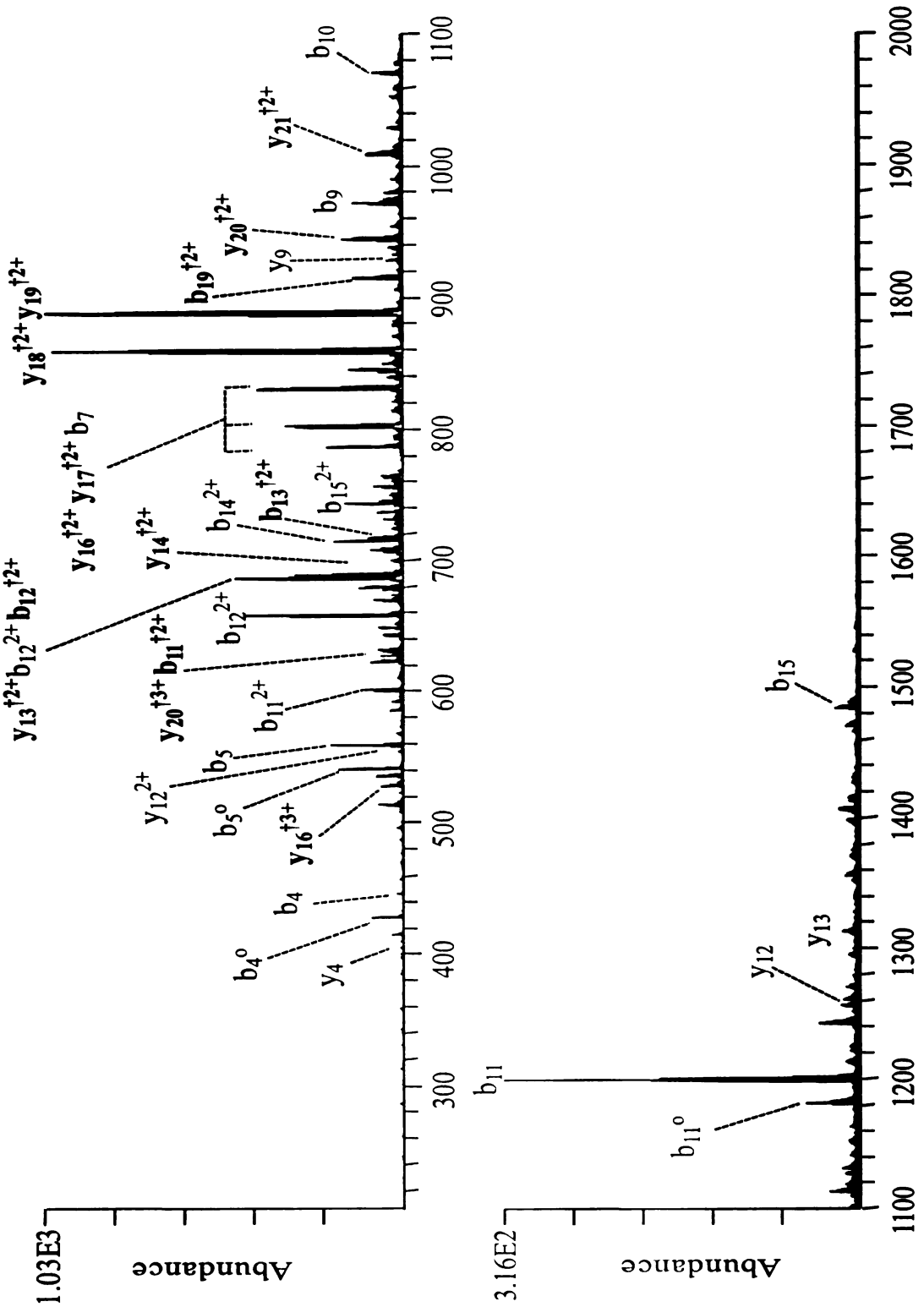

Figure S5: CID MS/MS Spectrum of the $[M+2H^{+}+Zn^{2}]^{4+}$ charge state (m/z = 772.0) of C-peptide

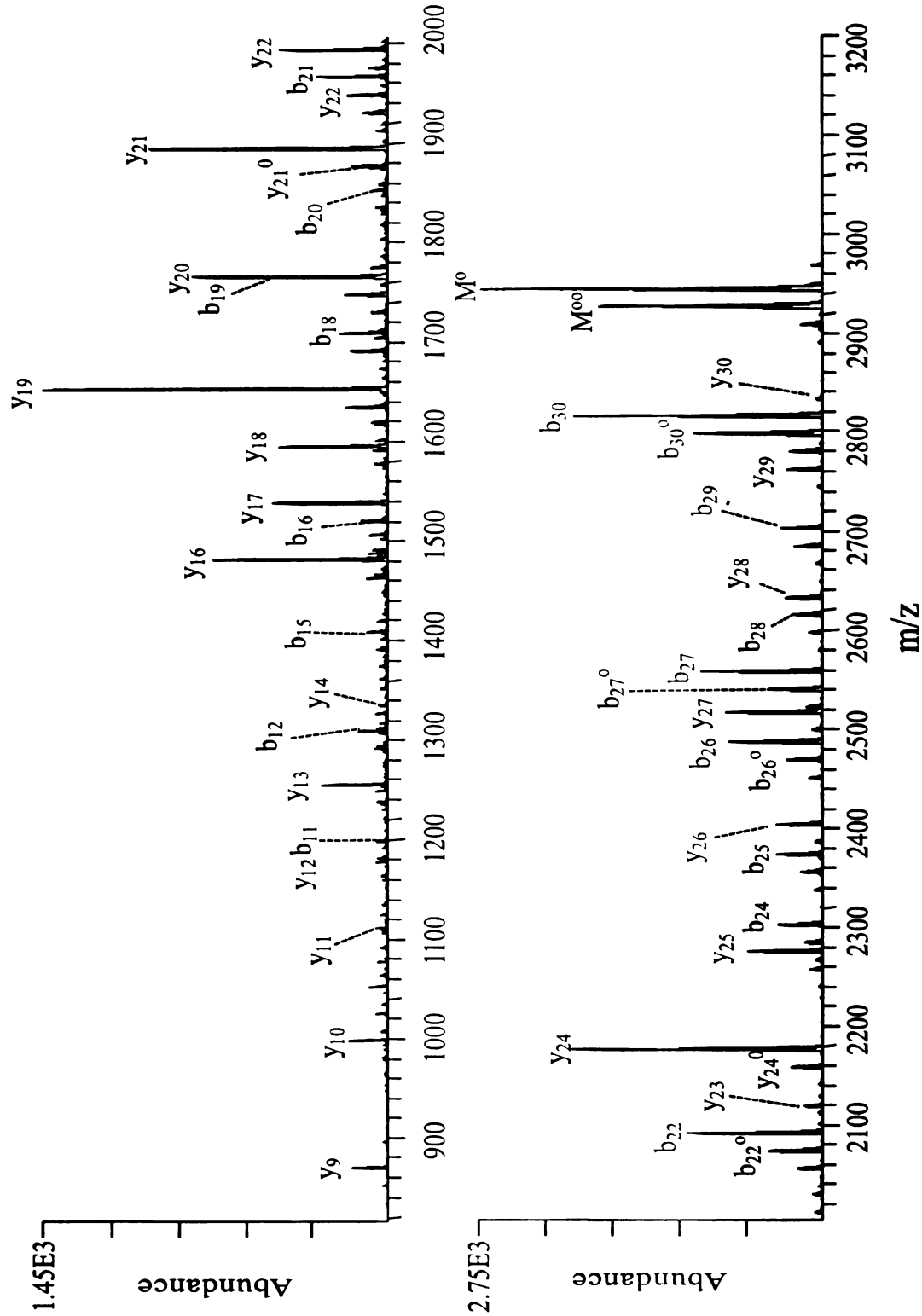

Figure S6: MALDI CID MS/MS Spectrum of the $[M+H^+]^+$ charge state (m/z = 2962) of E27A

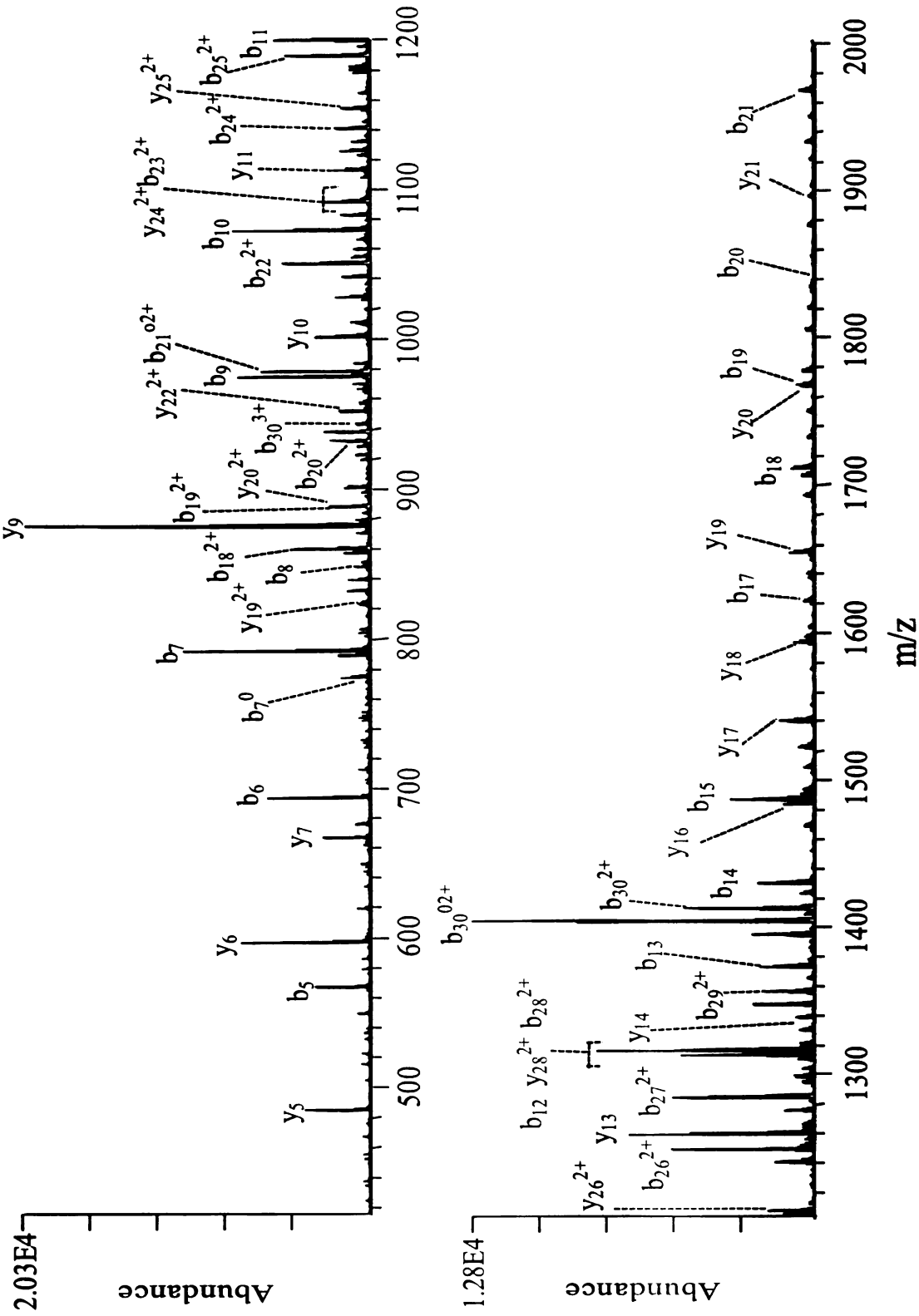

Figure S7: CID MS/MS Spectrum of the $[M+3H^+]^{3+}$ charge state (m/z = 988.6) of E27A

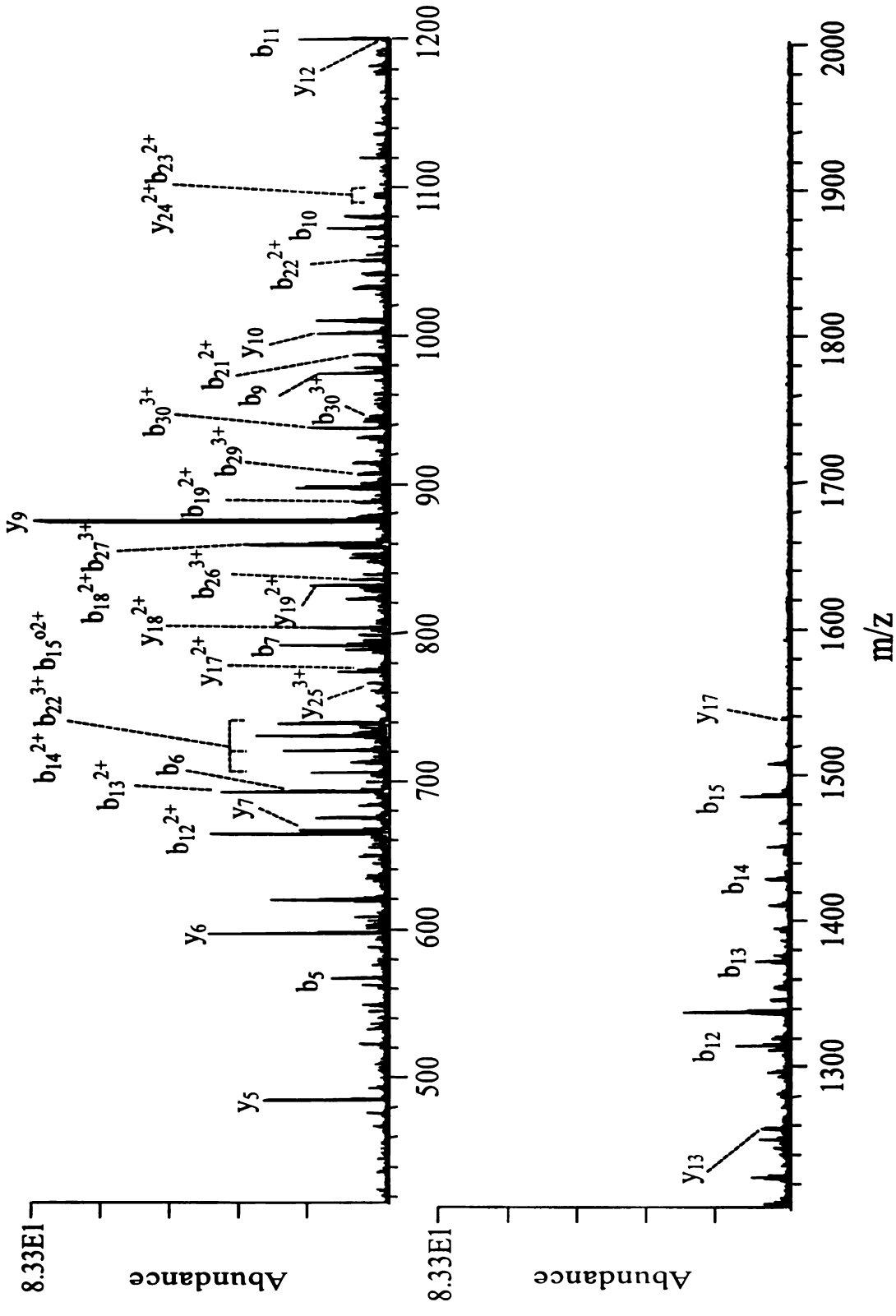

Figure S8: CID MS/MS Spectrum of the $[M+4H^+]^{4+}$ charge state (m/z = 741.5) of E27A

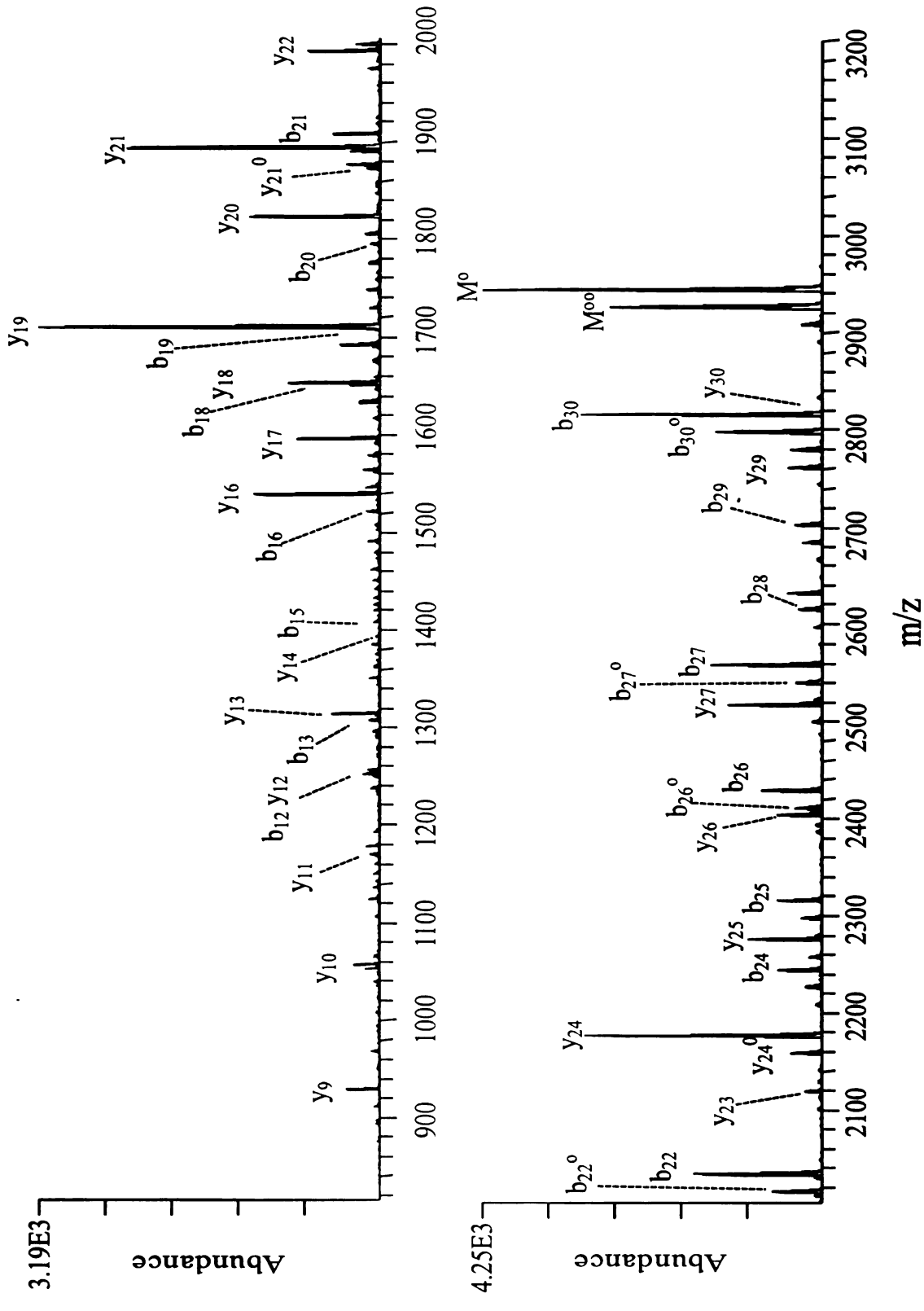

Figure S9: MALDI CID MS/MS Spectrum of the $[M+H^+]^+$ charge state (m/z = 2962.5) of E11A

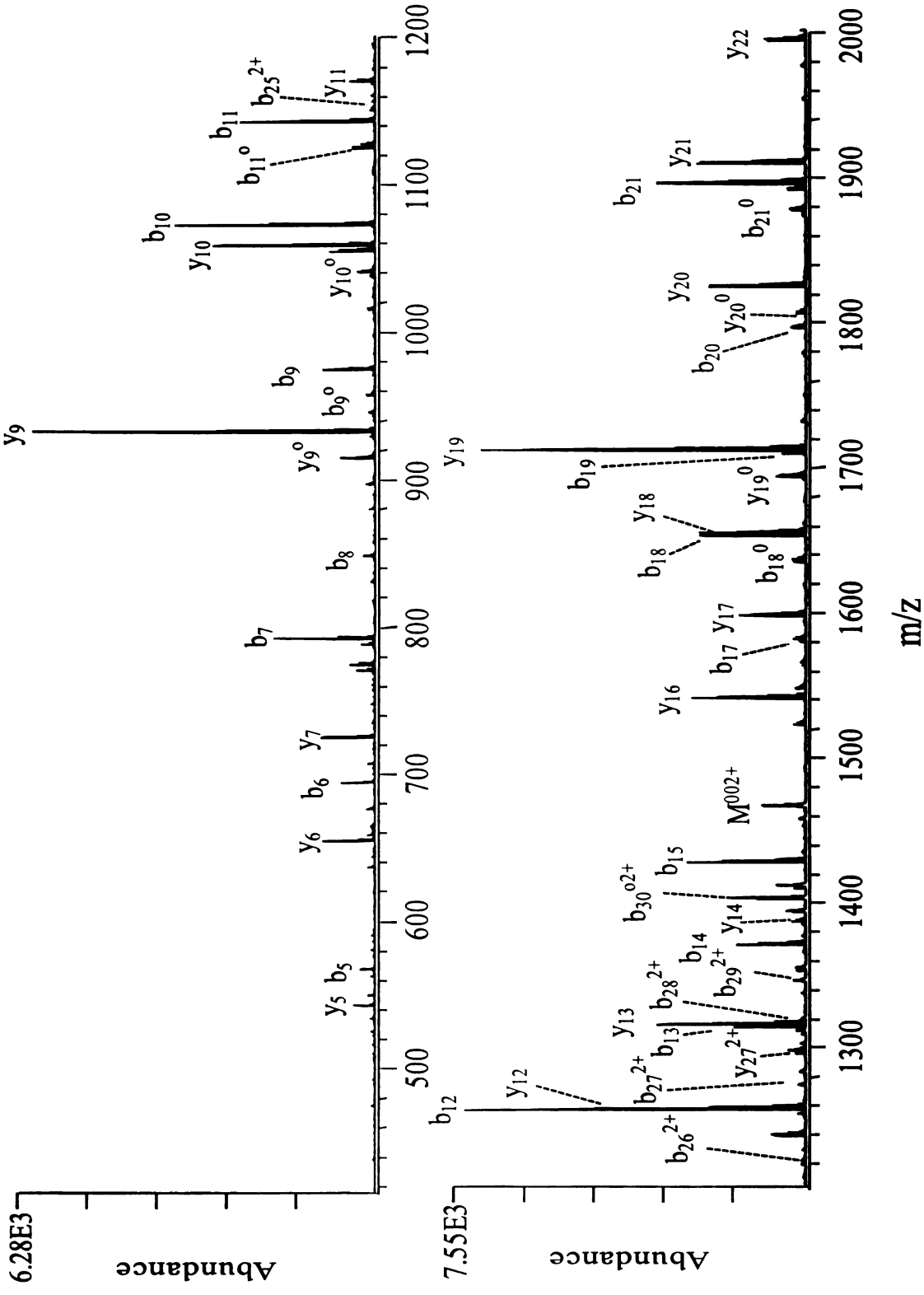

Figure S10: CID MS/MS Spectrum of the $[M+2H^{+}]^{2+}$ charge state (m/z = 1482.6) of E11A

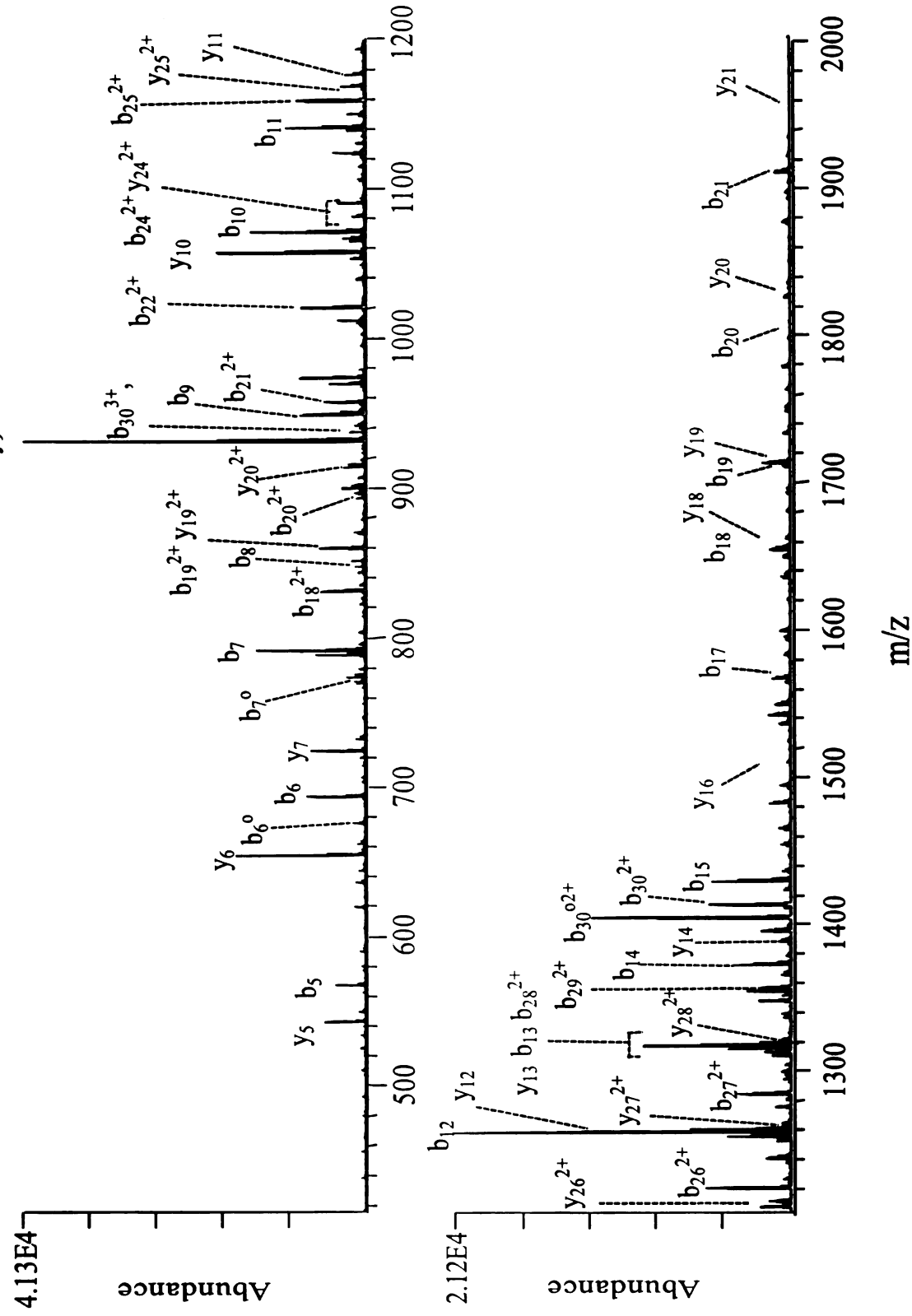

Figure S11: CID MS/MS Spectrum of the $[M+3H^{+}]^{3+}$ charge state (m/z = 988.6) of E11A

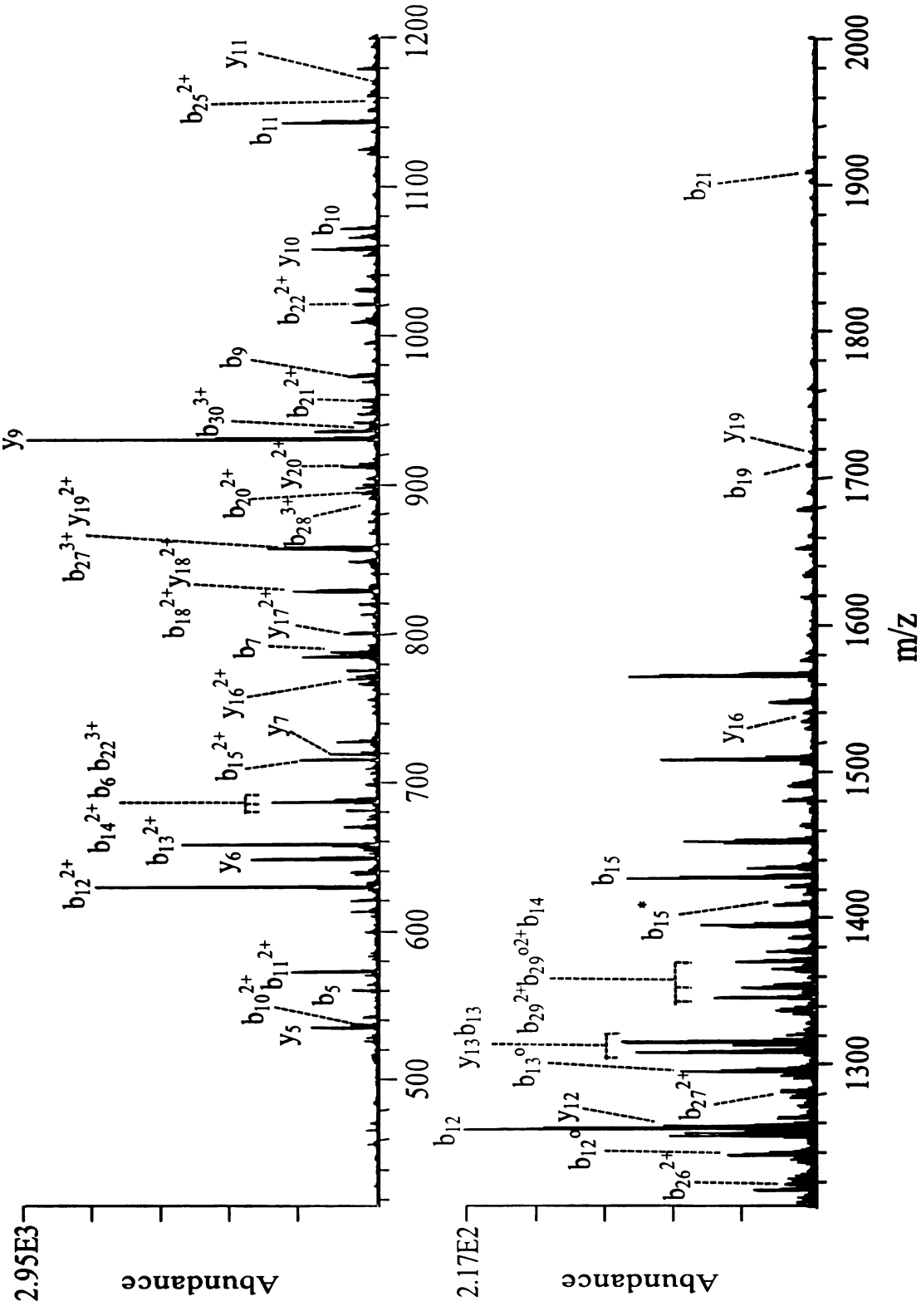

Figure S12: CID MS/MS Spectrum of the $[M+4H^+]^{4+}$ charge state (m/z = 741.5) of E11A

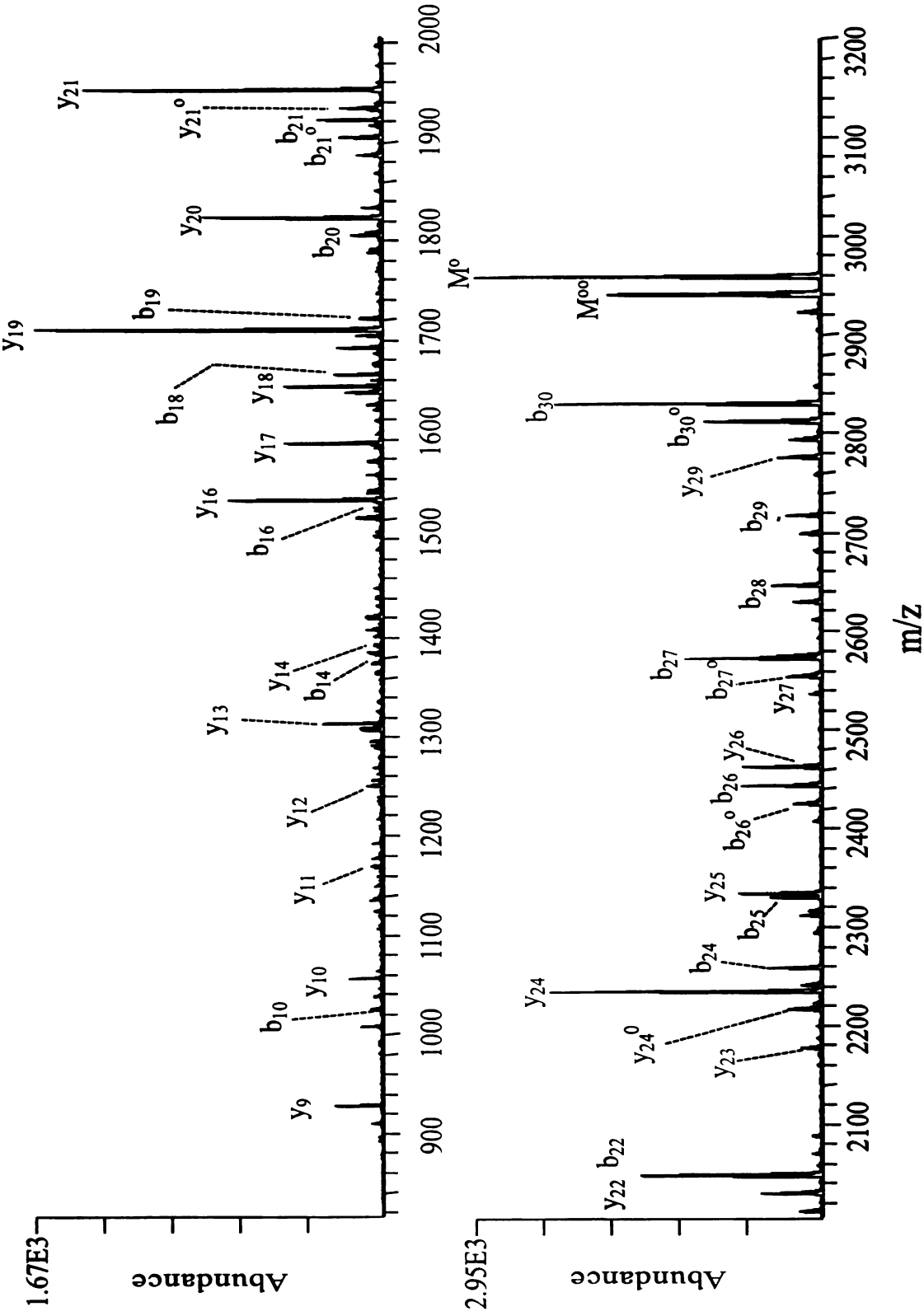

Figure S13: MALDI CID MS/MS Spectrum of the $[M+H^+]^+$ charge state (m/z = 2976) of D4A

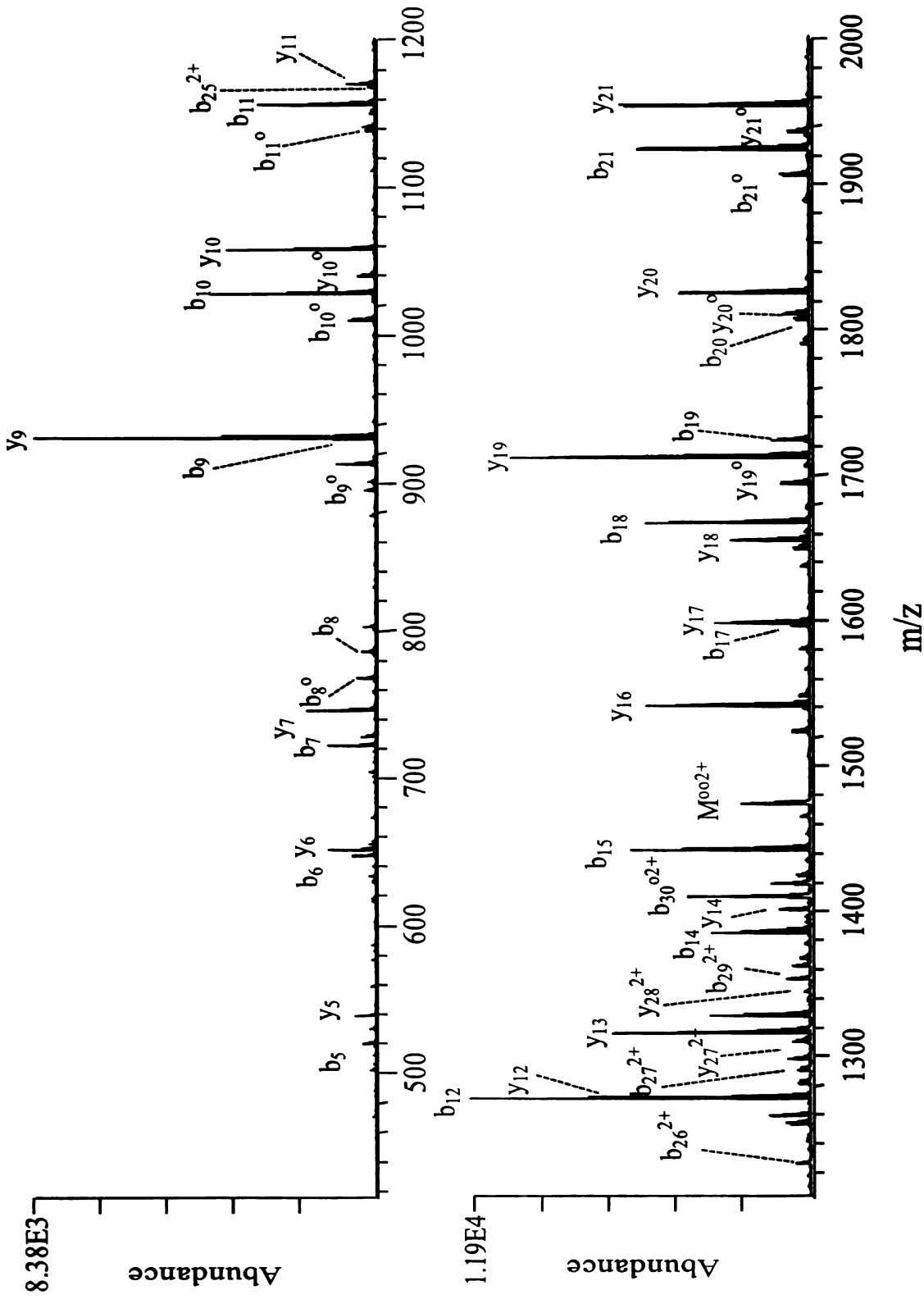

Figure S14: CID MS/MS Spectrum of the $[M+2H^{+}]^{2+}$ charge state (m/z = 1489.5) of D4A

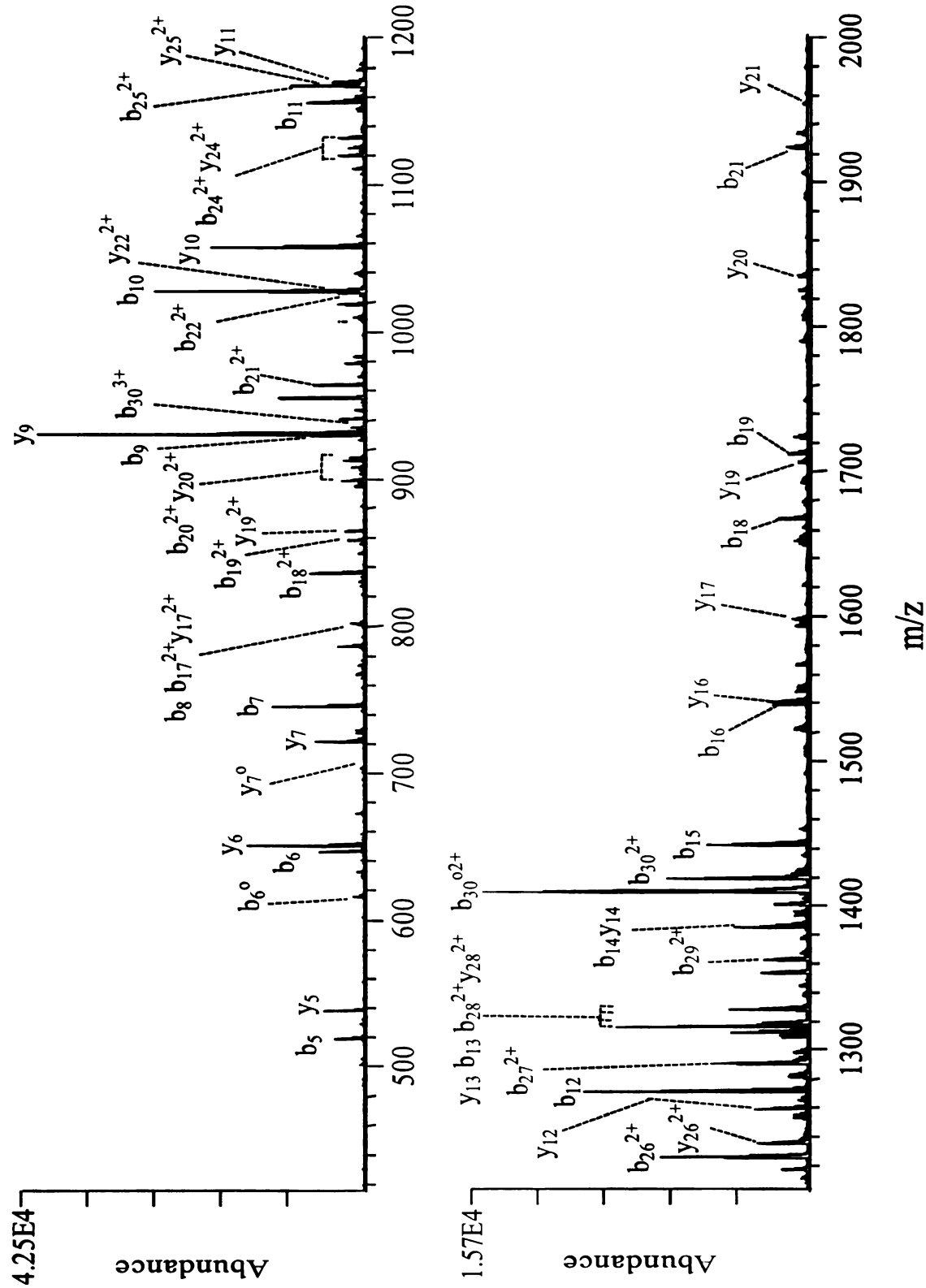

Figure S15: CID MS/MS Spectrum of the $[M+3H^+]^{3+}$ charge state (m/z = 993.5) of D4A

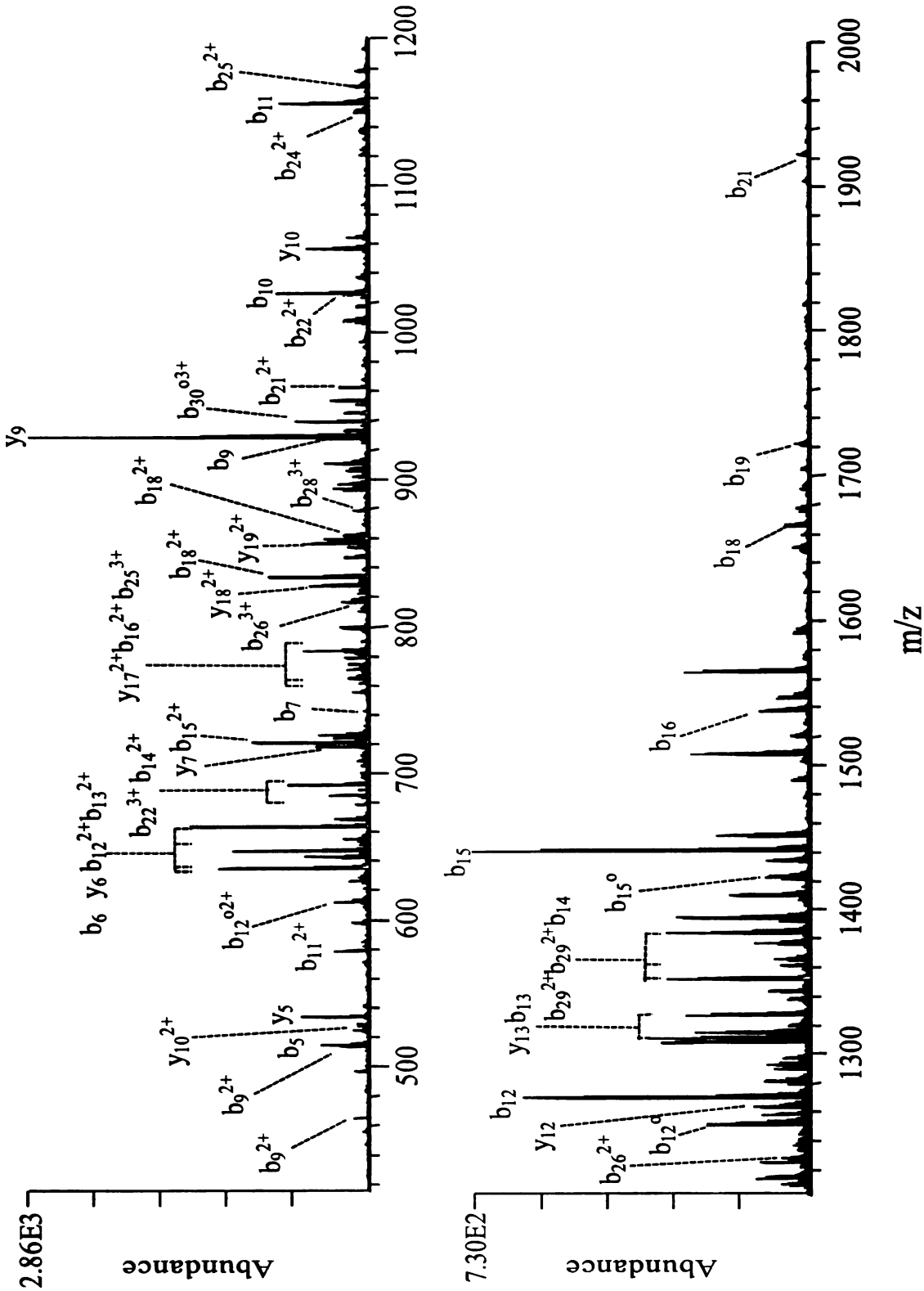

Figure S16: CID MS/MS Spectrum of the $[M+4H^{+}]^{4+}$ charge state (m/z = 745.5) of D4A

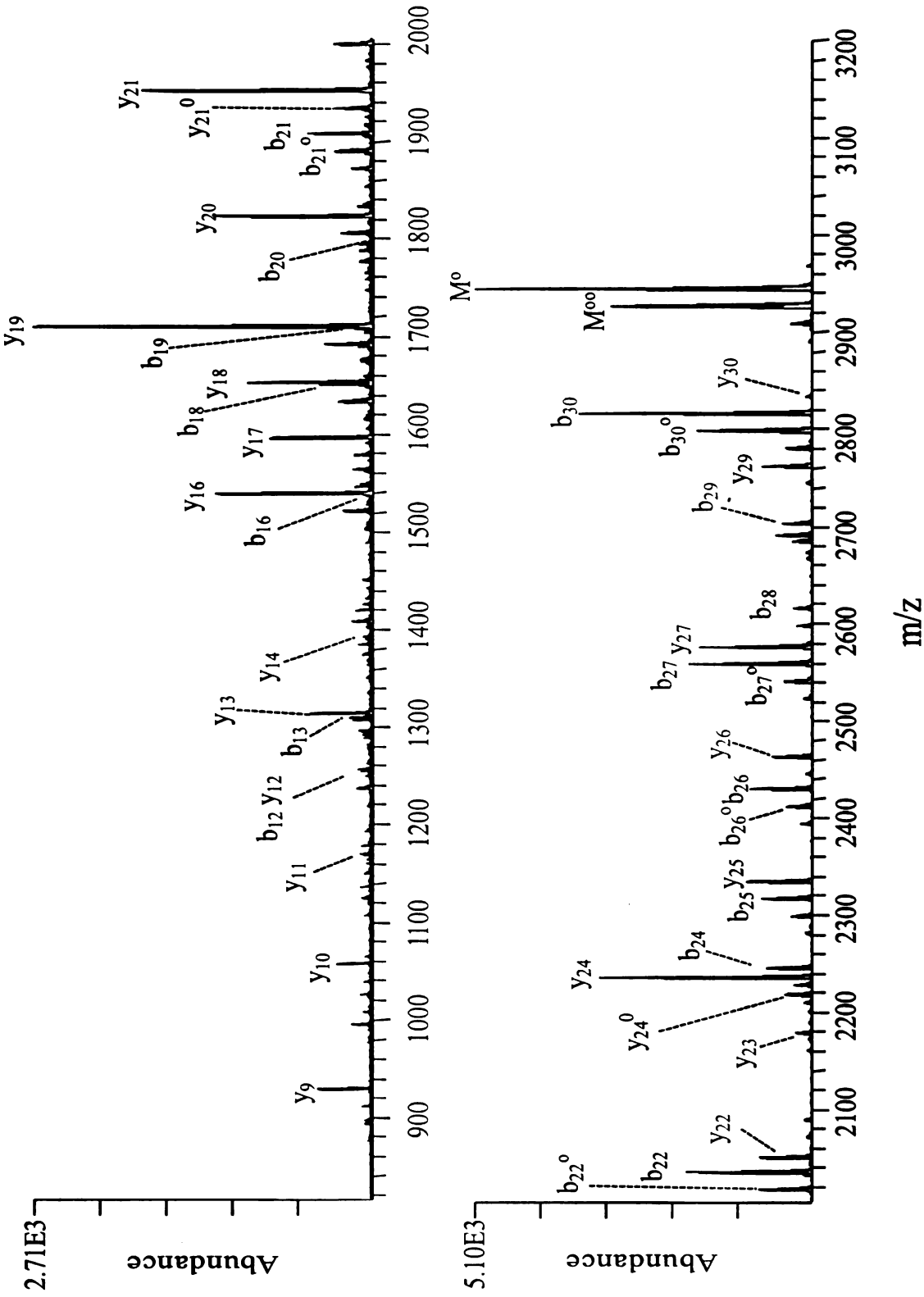

Figure S17: MALDI CID MS/MS Spectrum of the $[M+H^+]^+$ charge state (m/z = 2962.3) of E3A

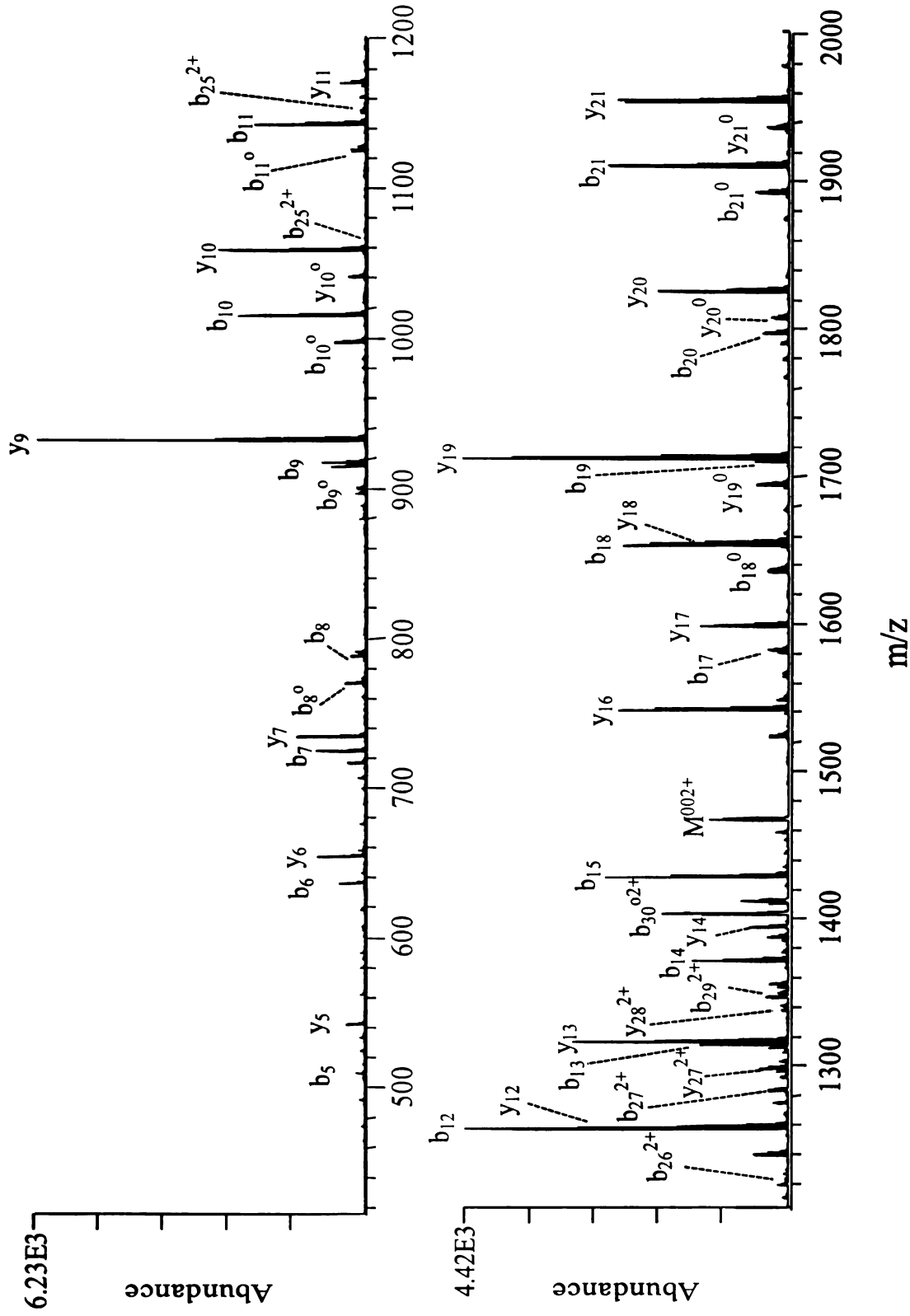

Figure S18: CID MS/MS Spectrum of the $[M+2H^{+}]^{2+}$ charge state (m/z = 1488.5) of E3A

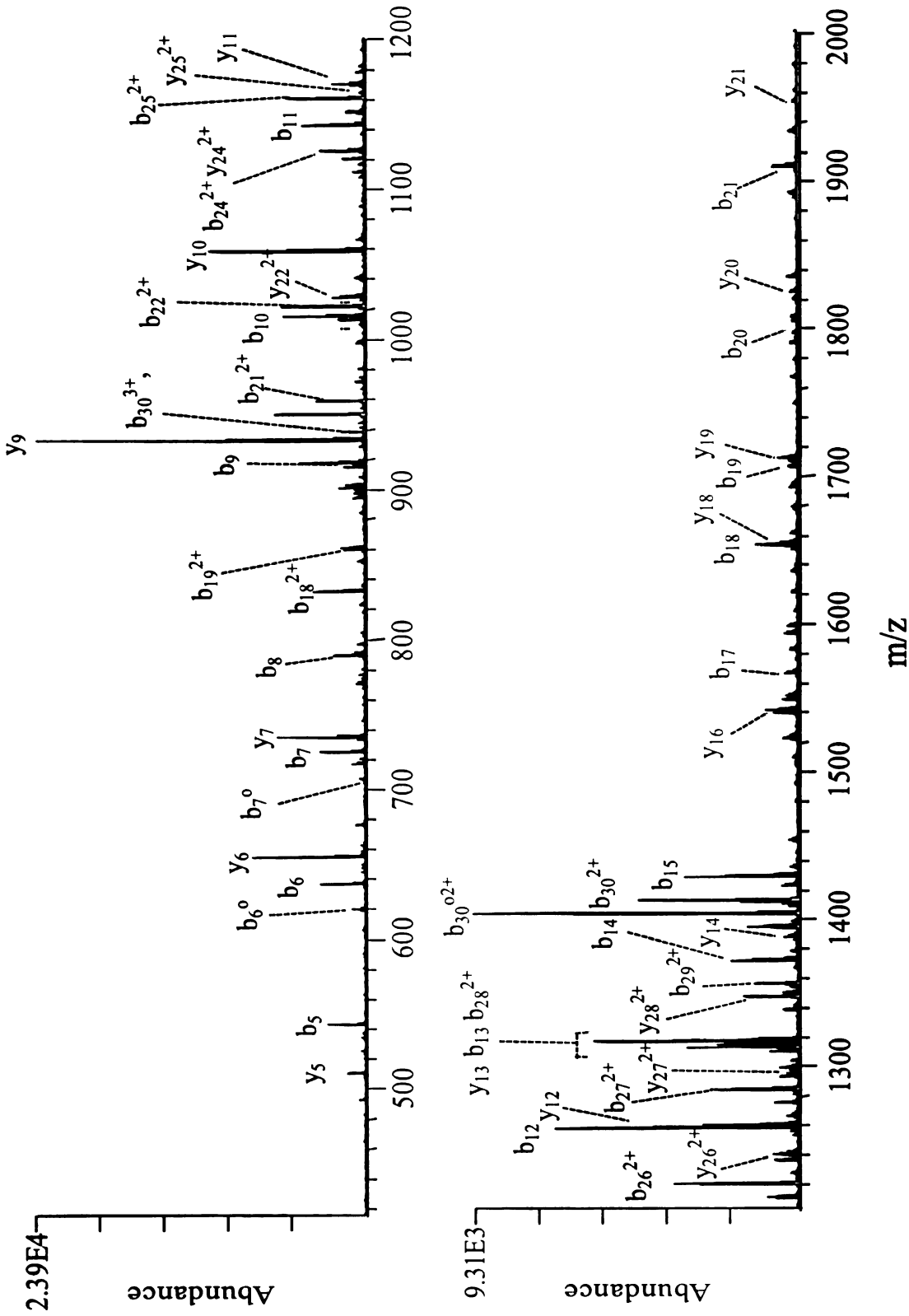

Figure S19: CID MS/MS Spectrum of the $[M+3H^{+}]^{3+}$ charge state (m/z = 988.5) of E3A

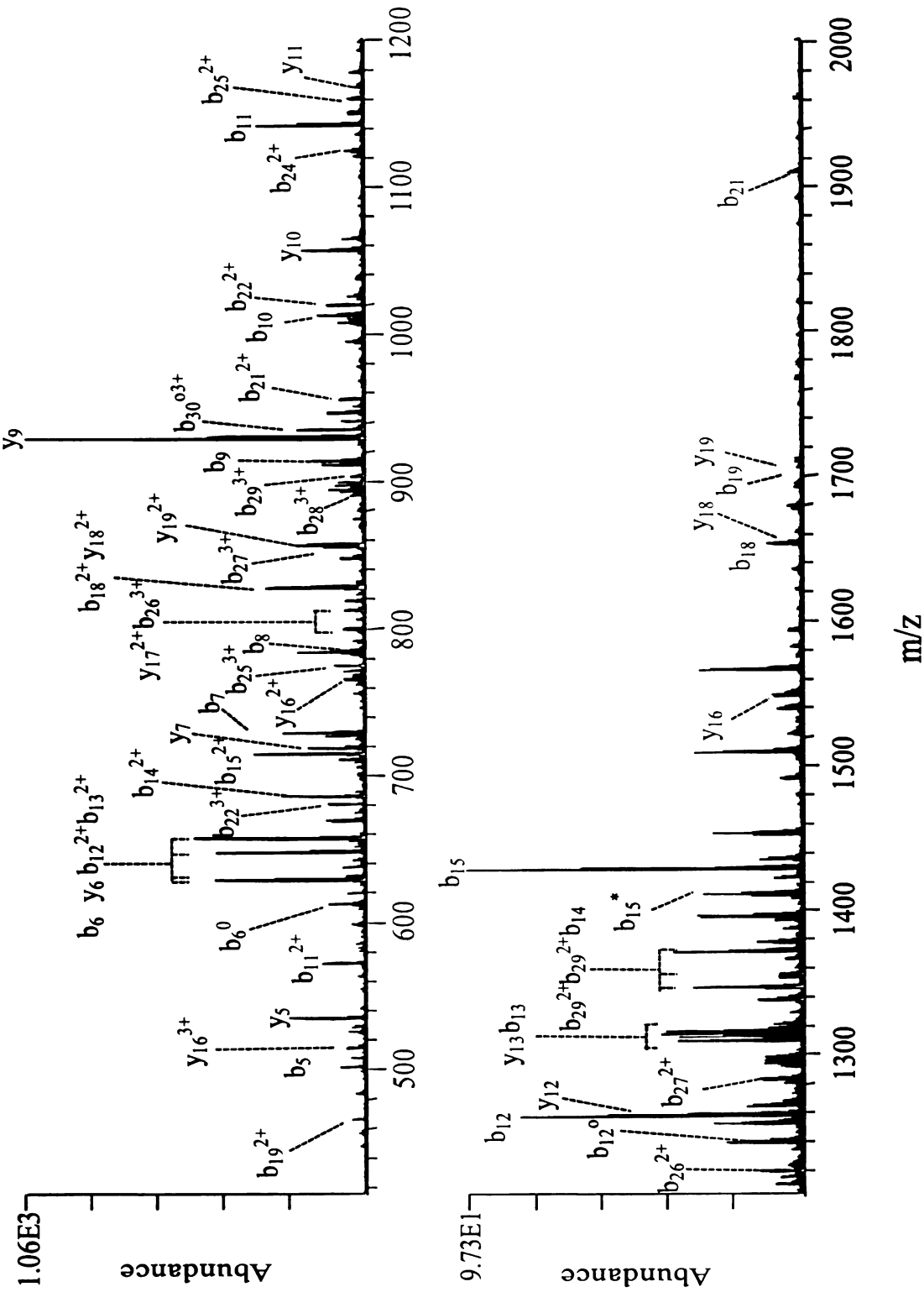

Figure S20: CID MS/MS Spectrum of the $[M+4H^{+}]^{4+}$ charge state (m/z = 741.6) of E3A

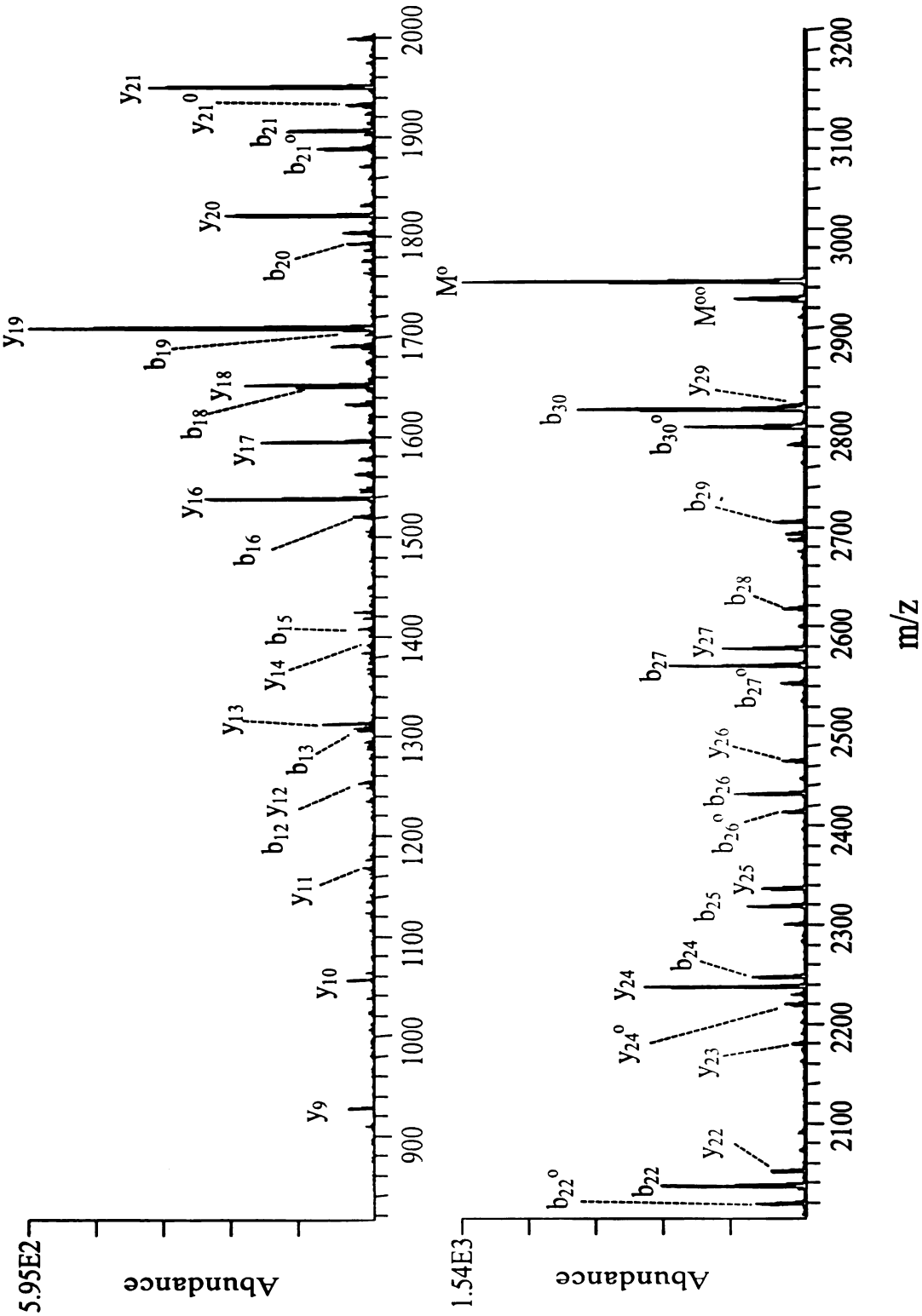

Figure S21: MALDI CID MS/MS Spectrum of the $[M+H^+]^+$ charge state (m/z = 2962.4) of E1A

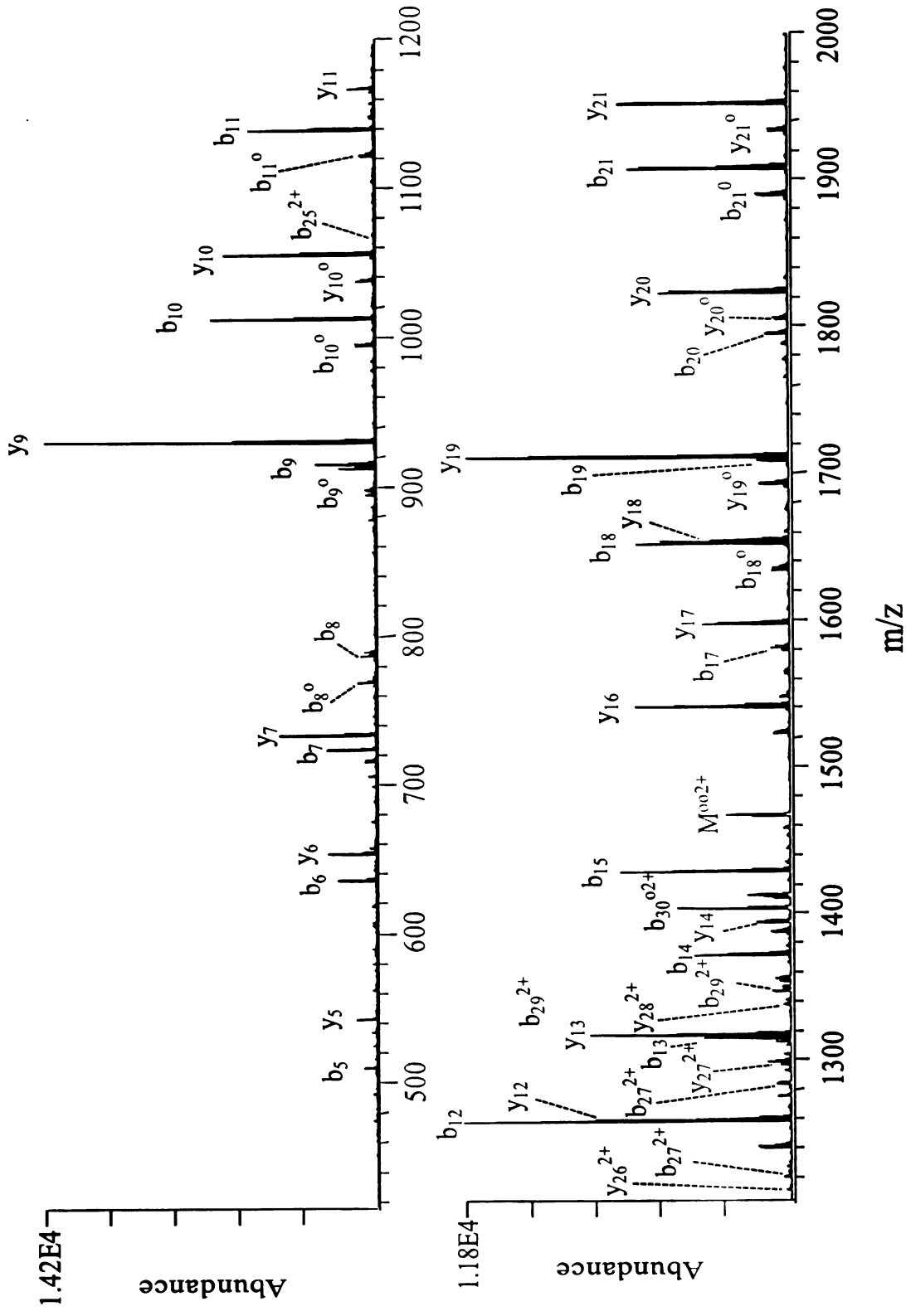

Figure S22: CID MS/MS Spectrum of the $[M+2H^{+}]^{2+}$ charge state (m/z = 1488.5) of E1A

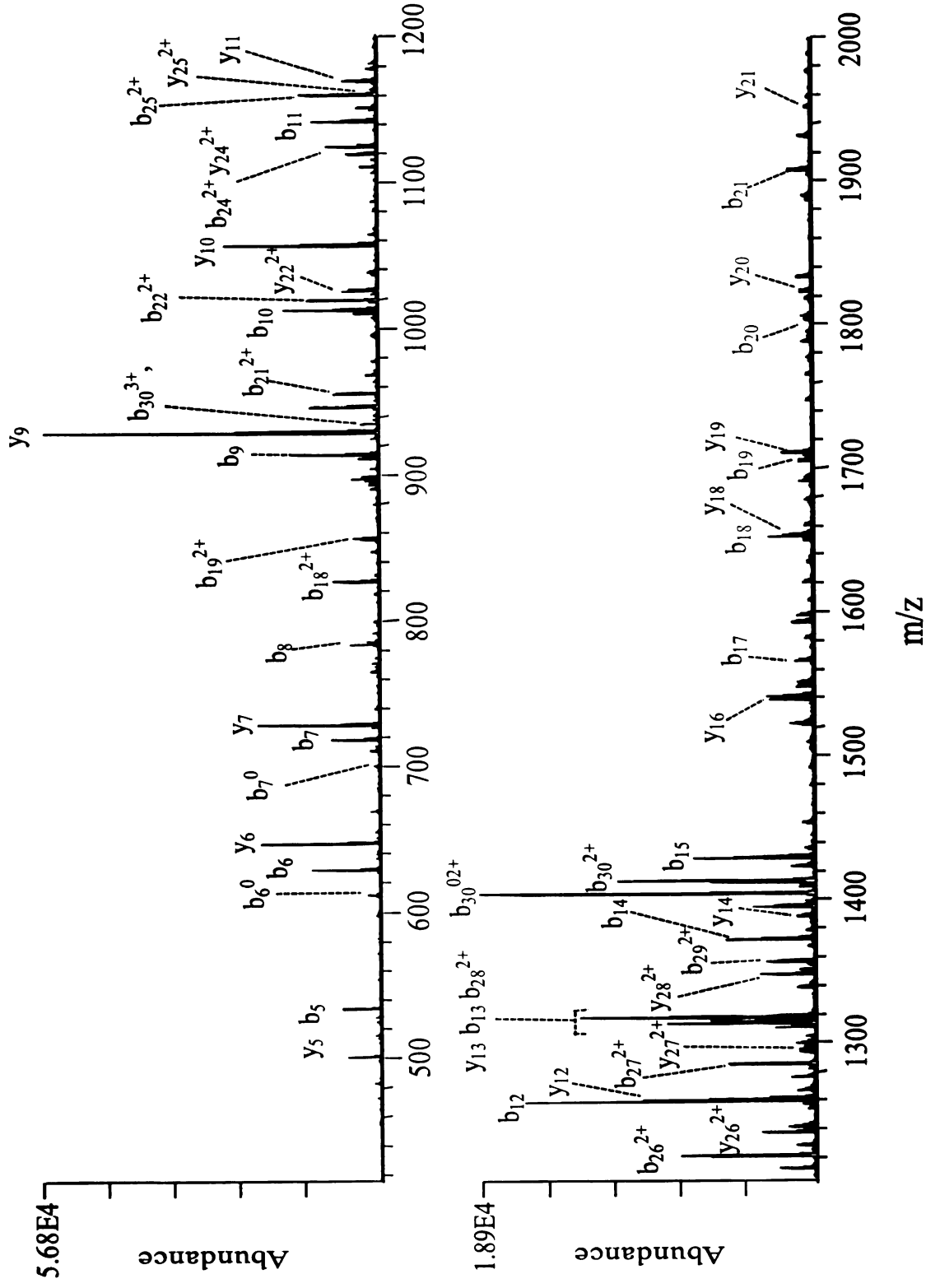

Figure S23: CID MS/MS Spectrum of the $[M+3H^{+}]^{3+}$ charge state (m/z = 988.5) of E1A

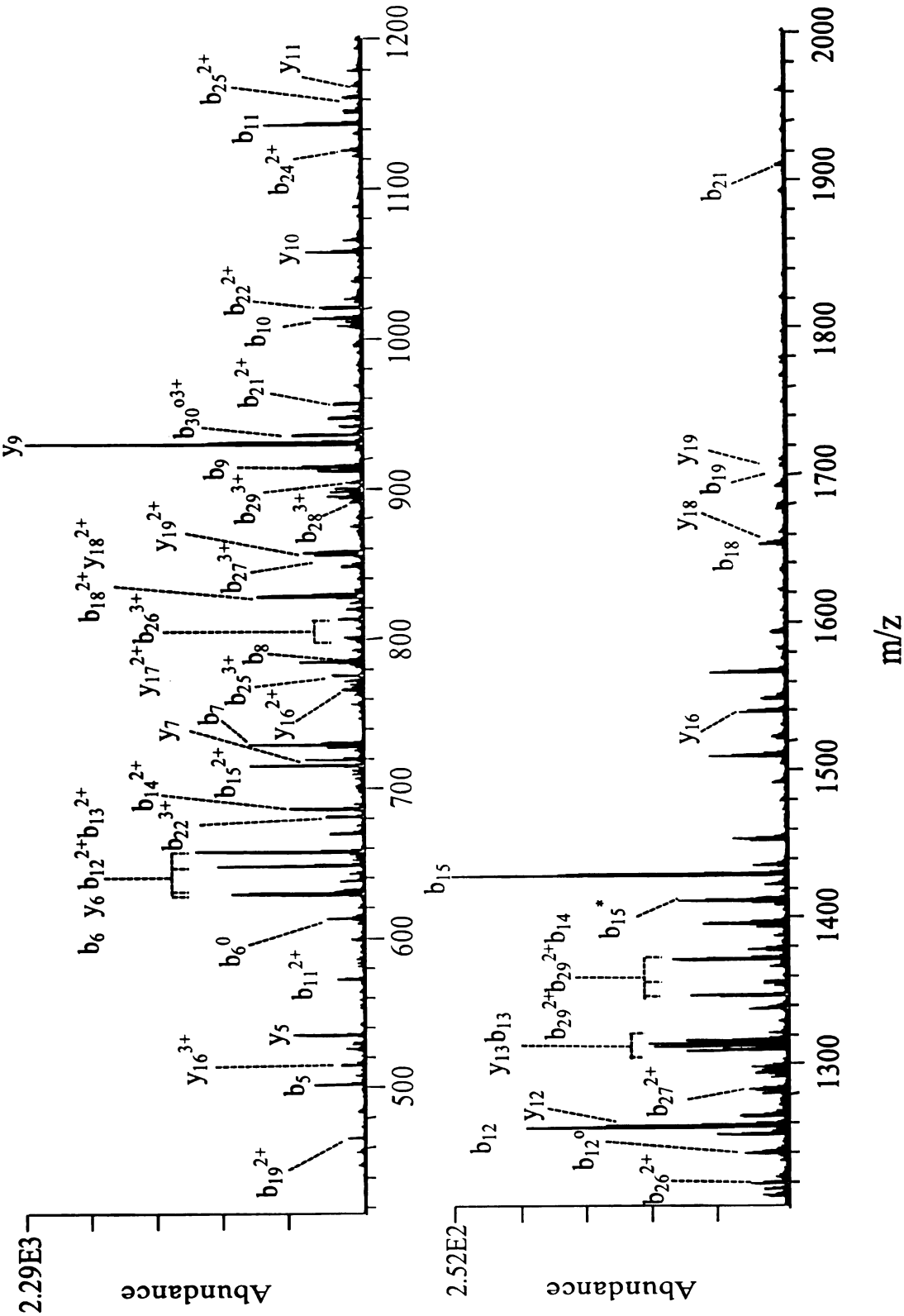

Figure S24: CID MS/MS Spectrum of the $[M+4H^{+}]^{4+}$ charge state (m/z = 741.5) of E1A

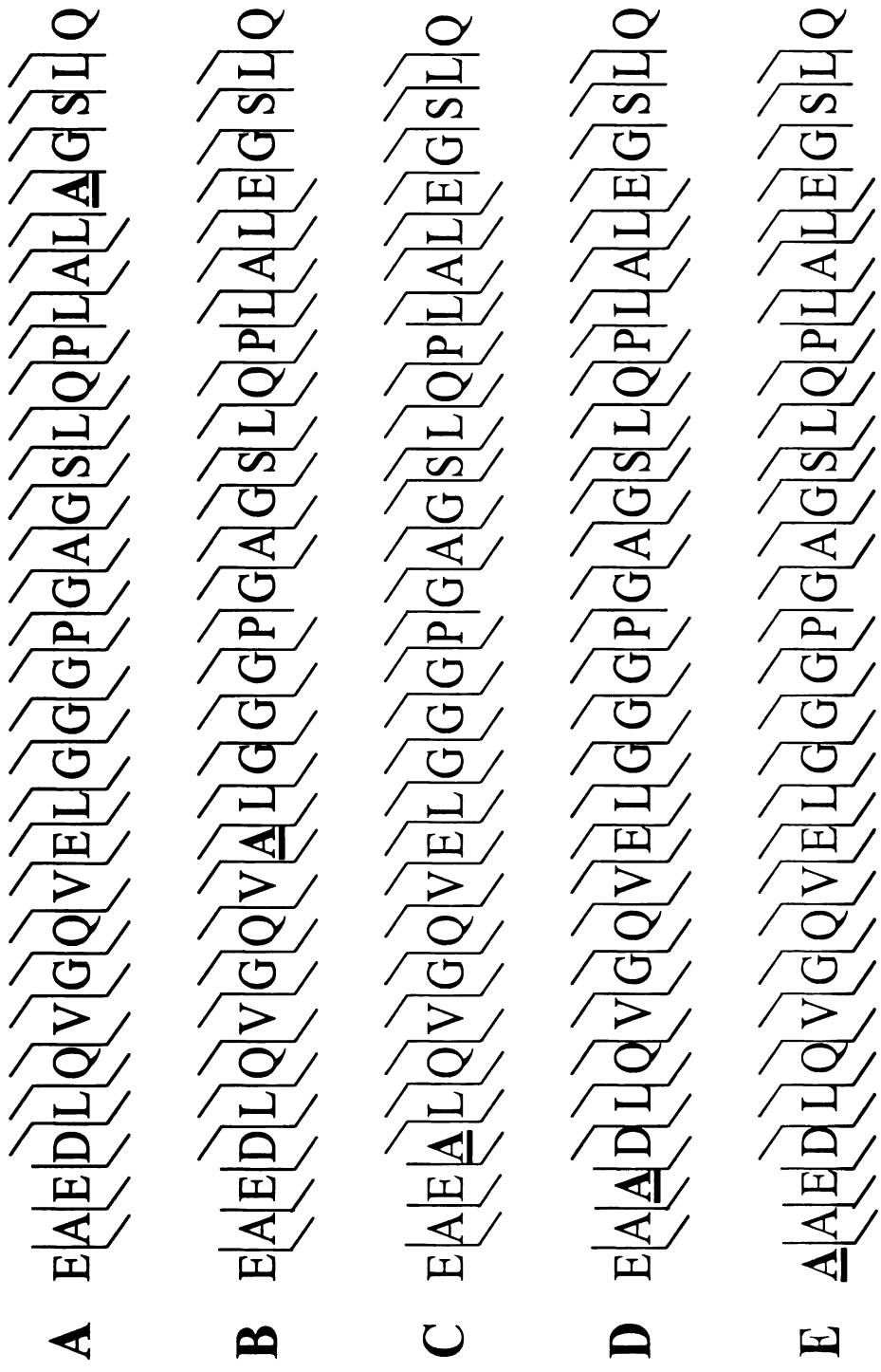

Figure S25: Overall product ion and sequence coverage summaries of the $[M+H^+]^+$, $[M+2H^+]^{2+}$, $[M+3H^+]^{3+}$, and $[M+4H^+]^{4+}$ charge states of the A)E27A, B) E11A, C) D4A, D) E3A, and E) E1A mutants of C-peptide

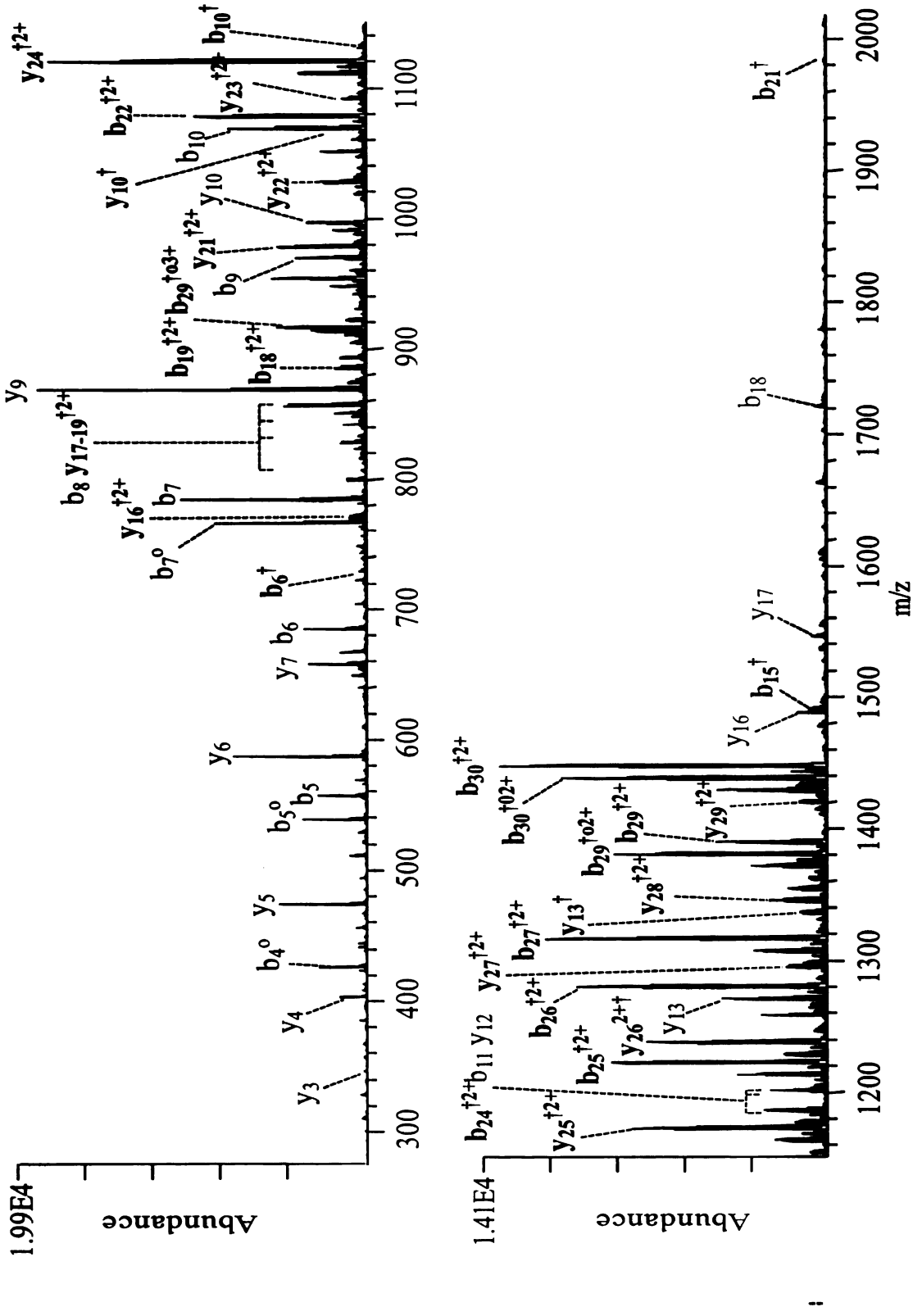

Figure S26: CID MS/MS Spectrum of the $[M+Zn^{2+}+H^{+}]^{3+}$ charge state (m/z = 1008.9) of E27A

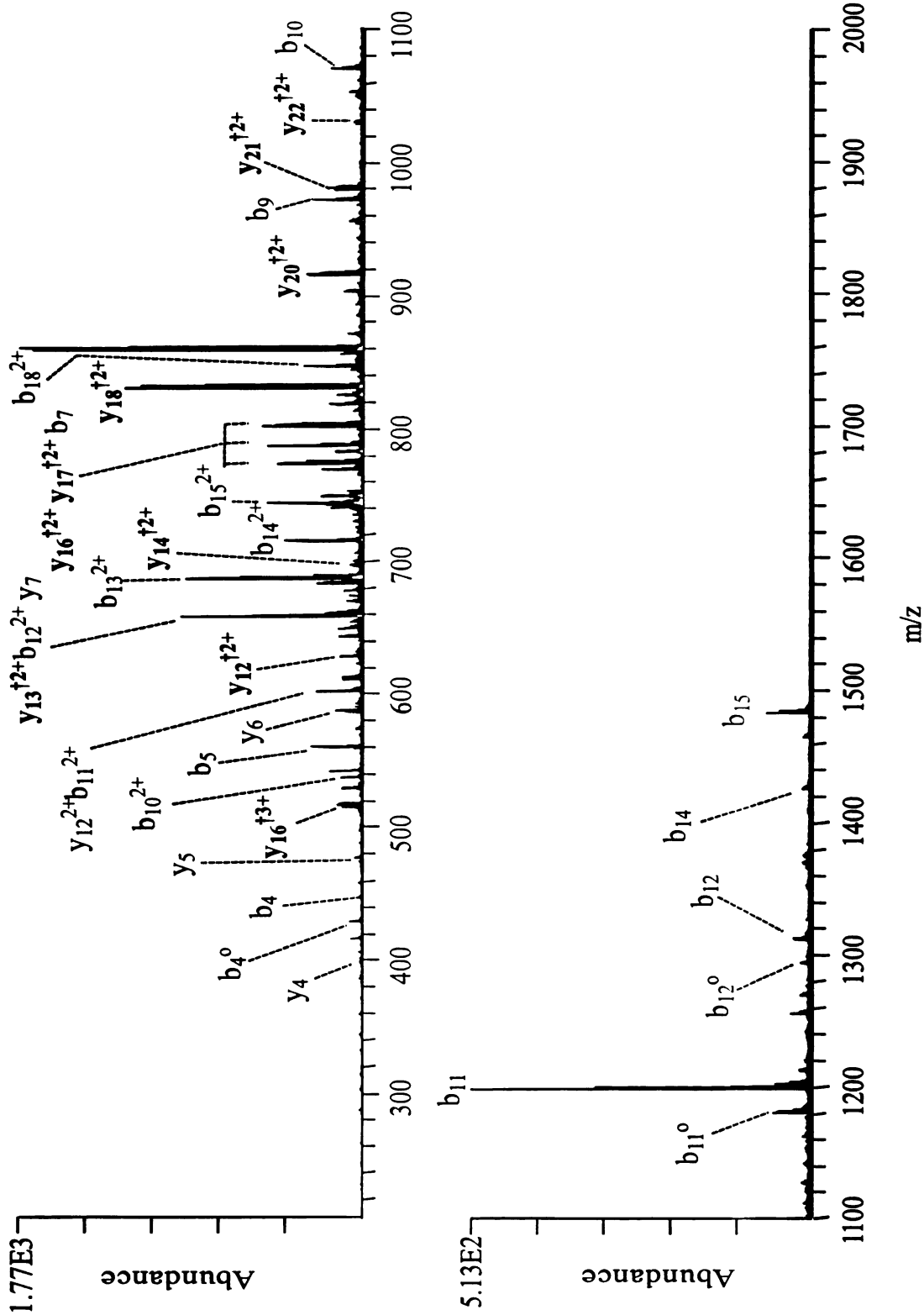

Figure S27: CID MS/MS Spectrum of the $[M+Zn^{2+}+2H^{+}]^{4+}$ charge state (m/z = 758.0) of E27A

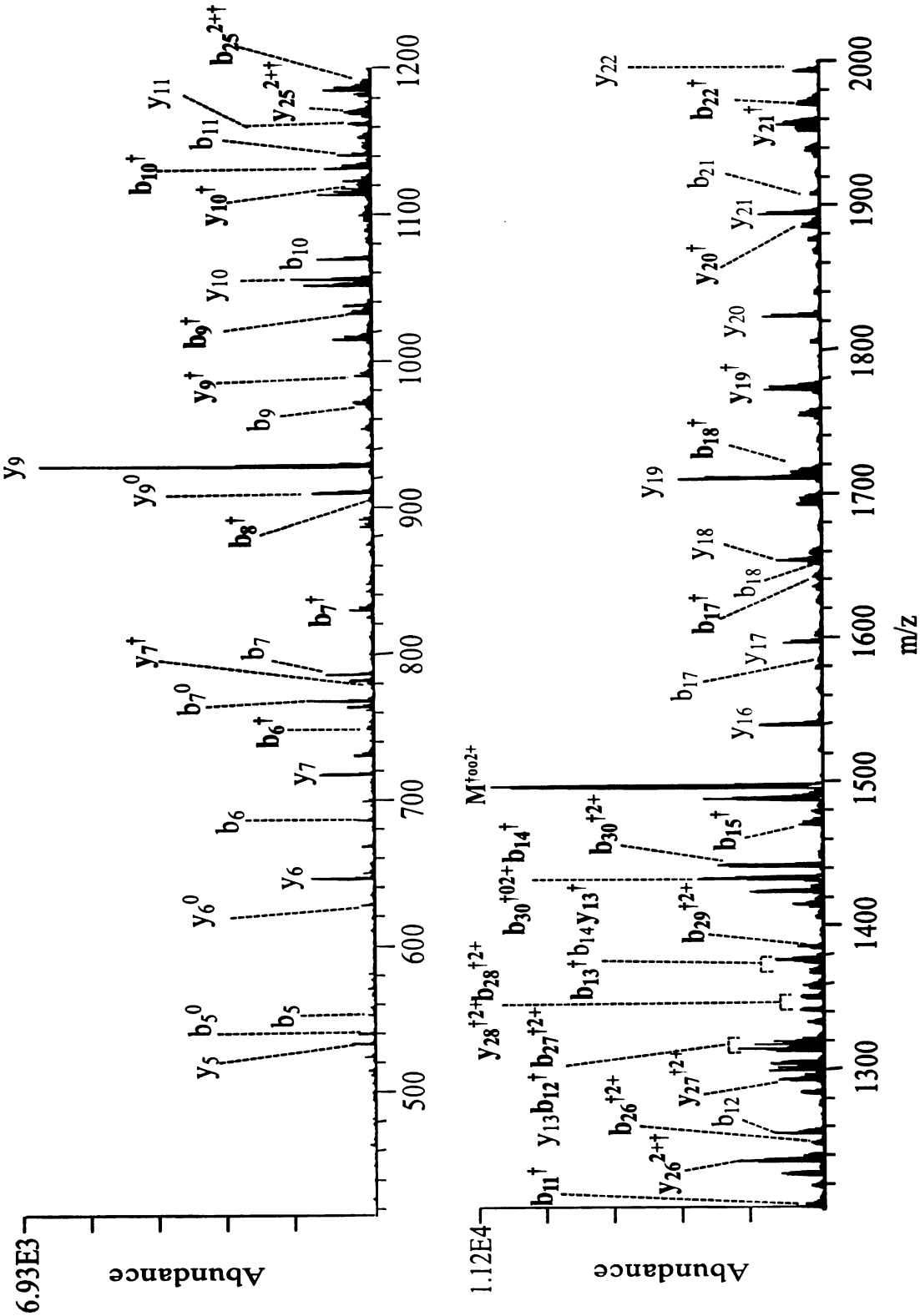

Figure S28: CID MS/MS Spectrum of the $[M+Zn^2]^{2+}$ charge state (m/z = 1514.4) of E11A

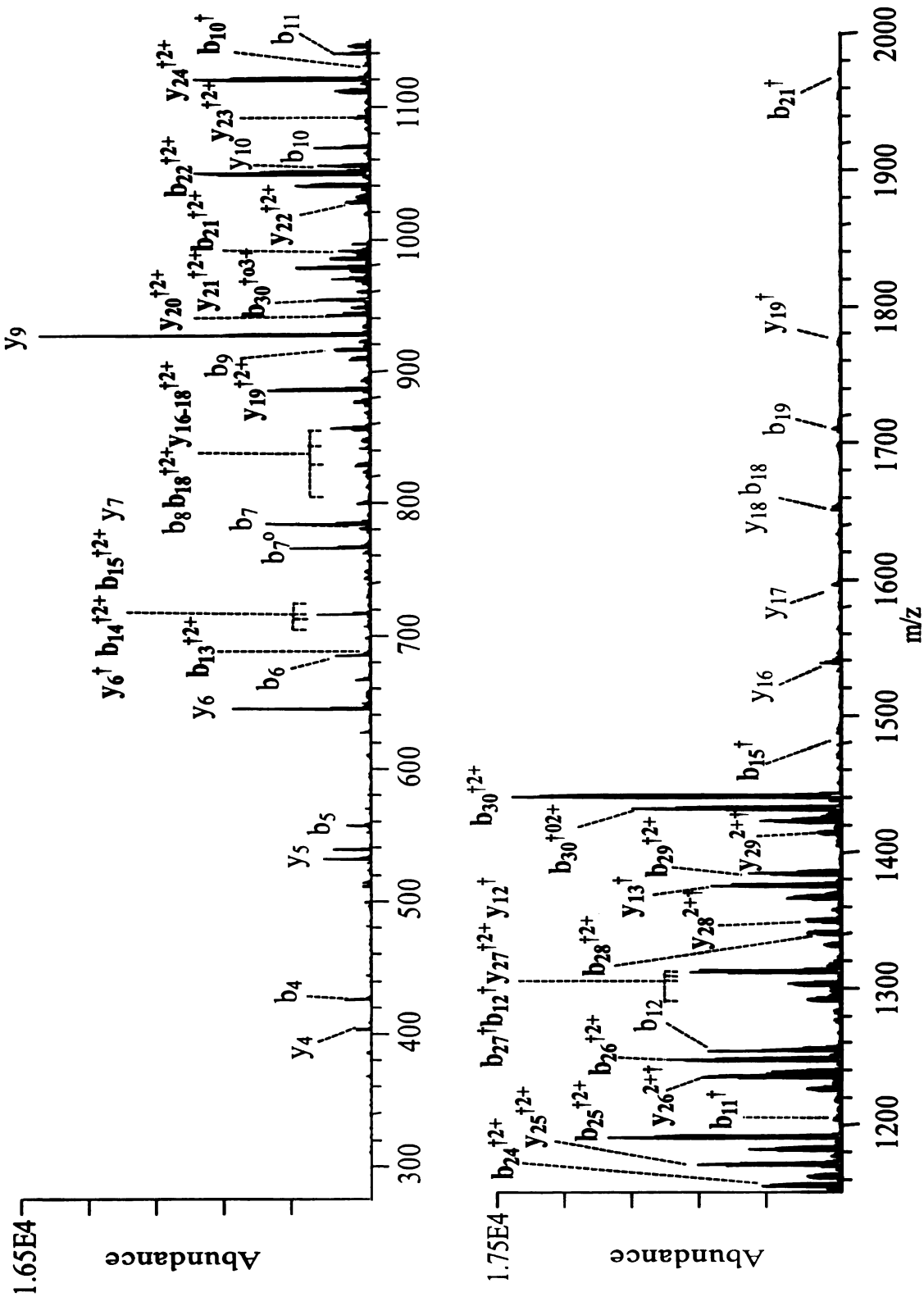

Figure S29: CID MS/MS Spectrum of the $[M+H^{+}+Zn^{2}]^{3+}$ charge state (m/z = 1008.9) of E11A

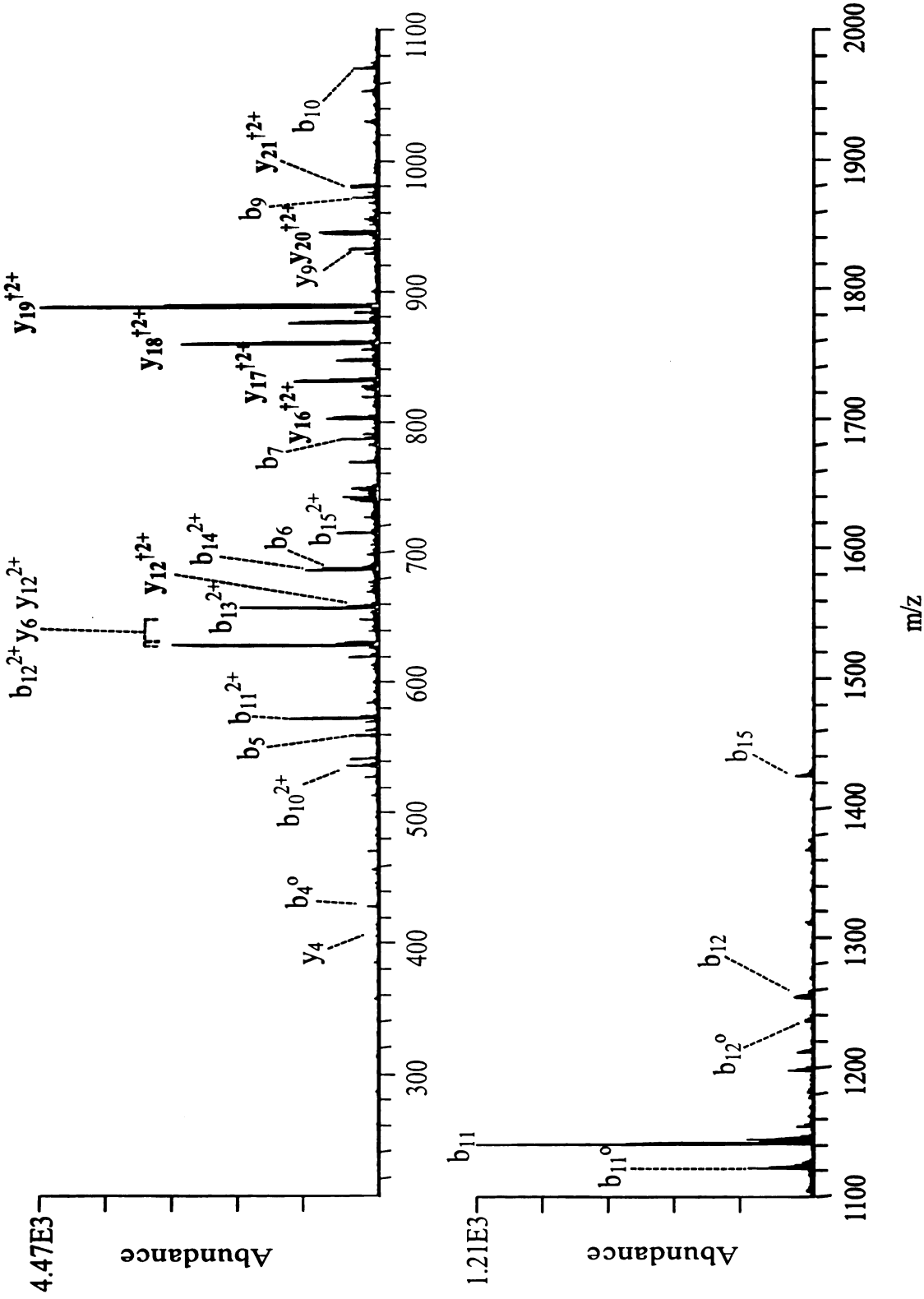

Figure S30: CID MS/MS Spectrum of the $[M+2H^{+}+Zn^{2}]^{4+}$ charge state (m/z = 758.0) of E11A

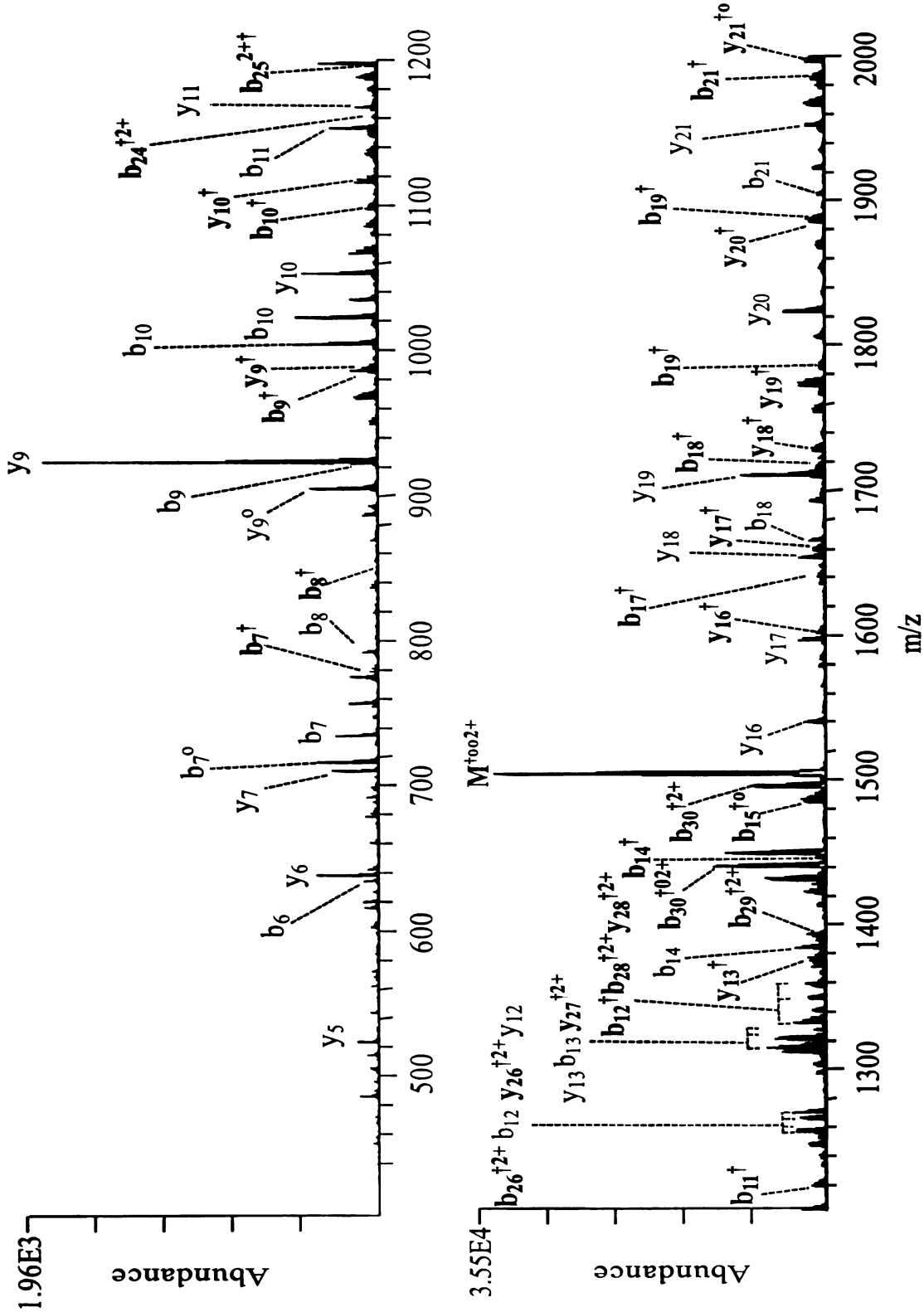

Figure S31: CID MS/MS Spectrum of the $[M+Zn^{2}]^{2+}$ charge state (m/z = 1521.6) of D4A

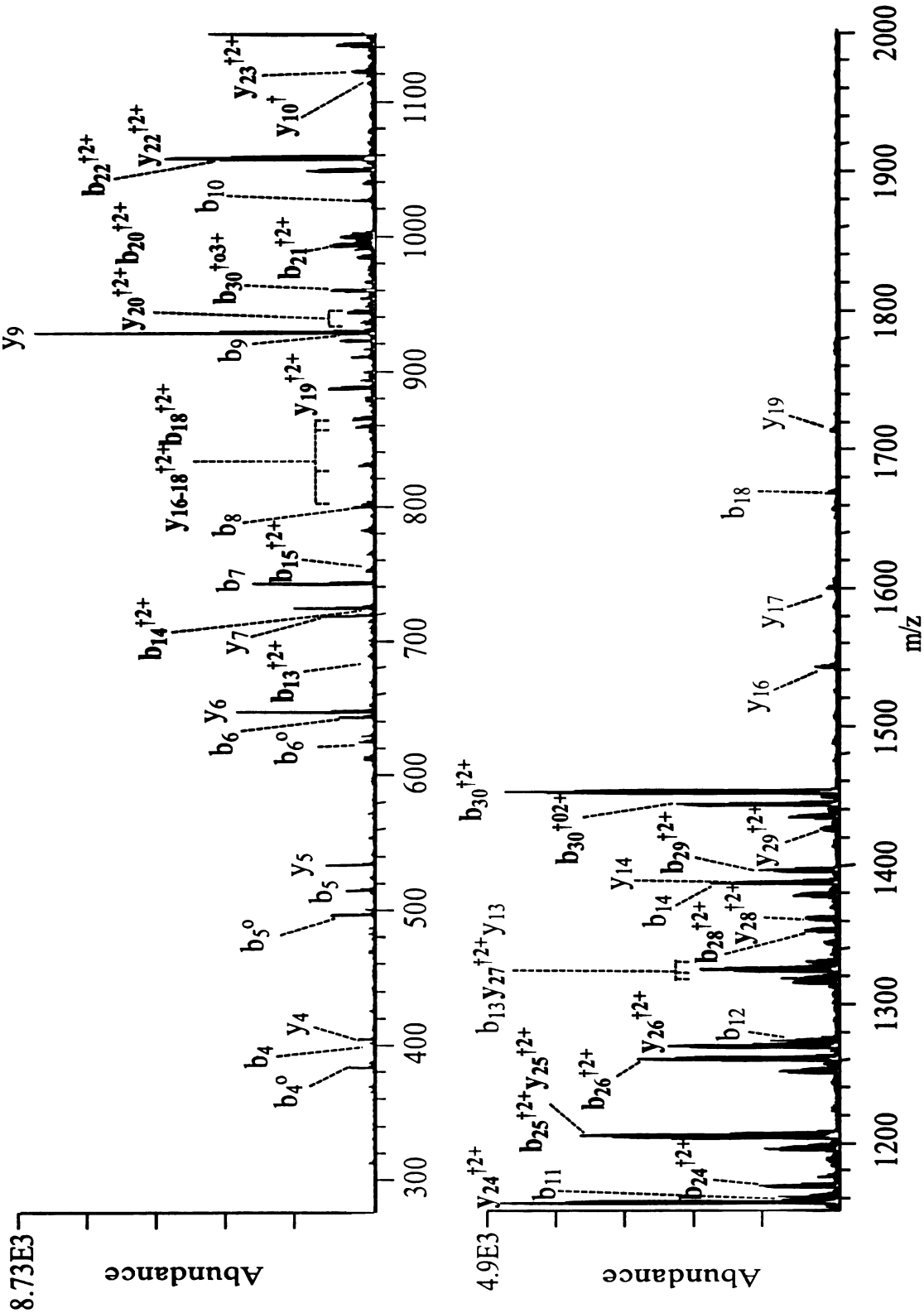

Figure S32: CID MS/MS Spectrum of the $[M+H^{+}+Zn^{2}]^{3+}$ charge state (m/z = 1014.0) of D4A

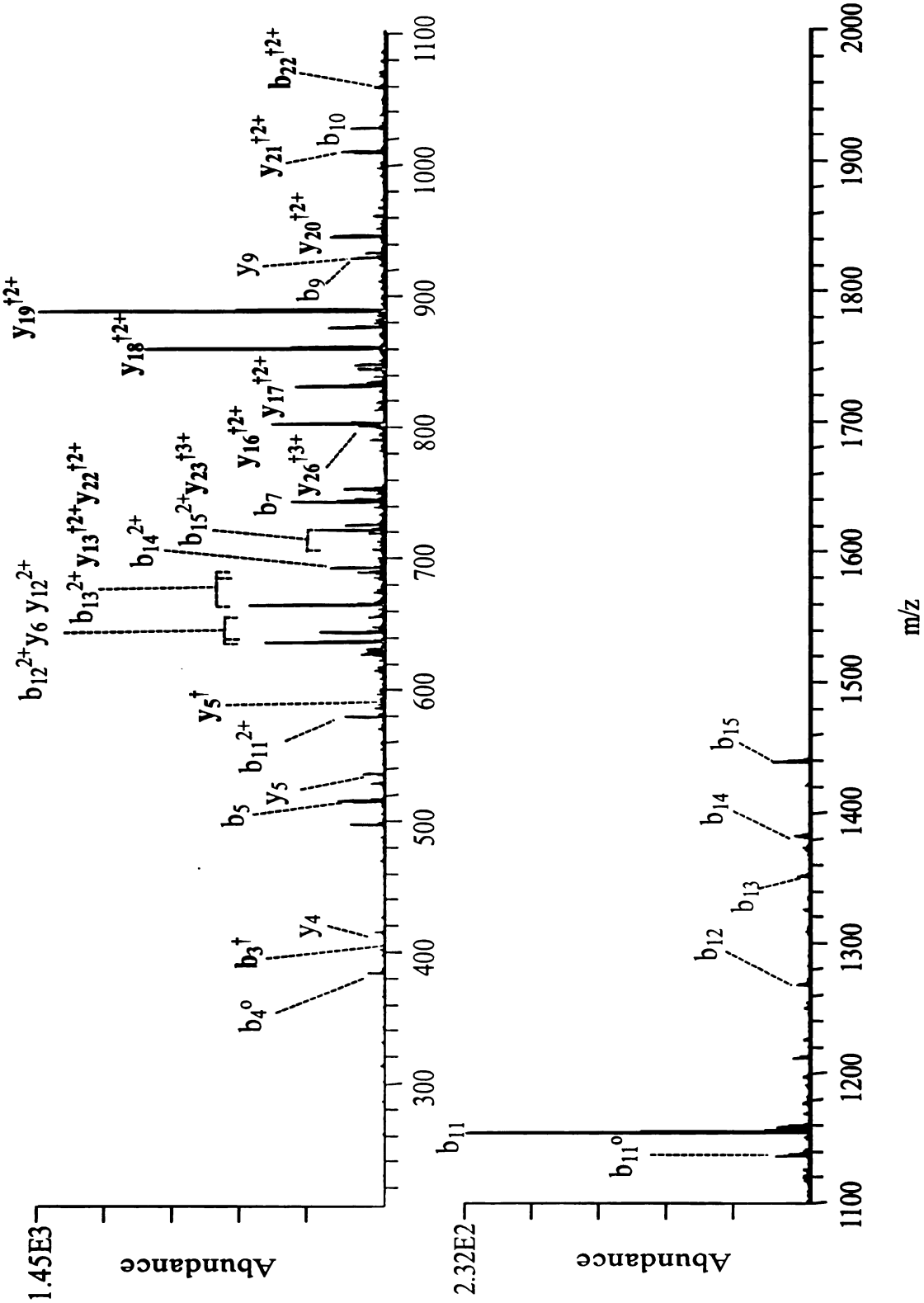

Figure S33: CID MS/MS Spectrum of the $[M+2H^{+}+Zn^{2}]^{4+}$ charge state (m/z = 760.7) of D4A

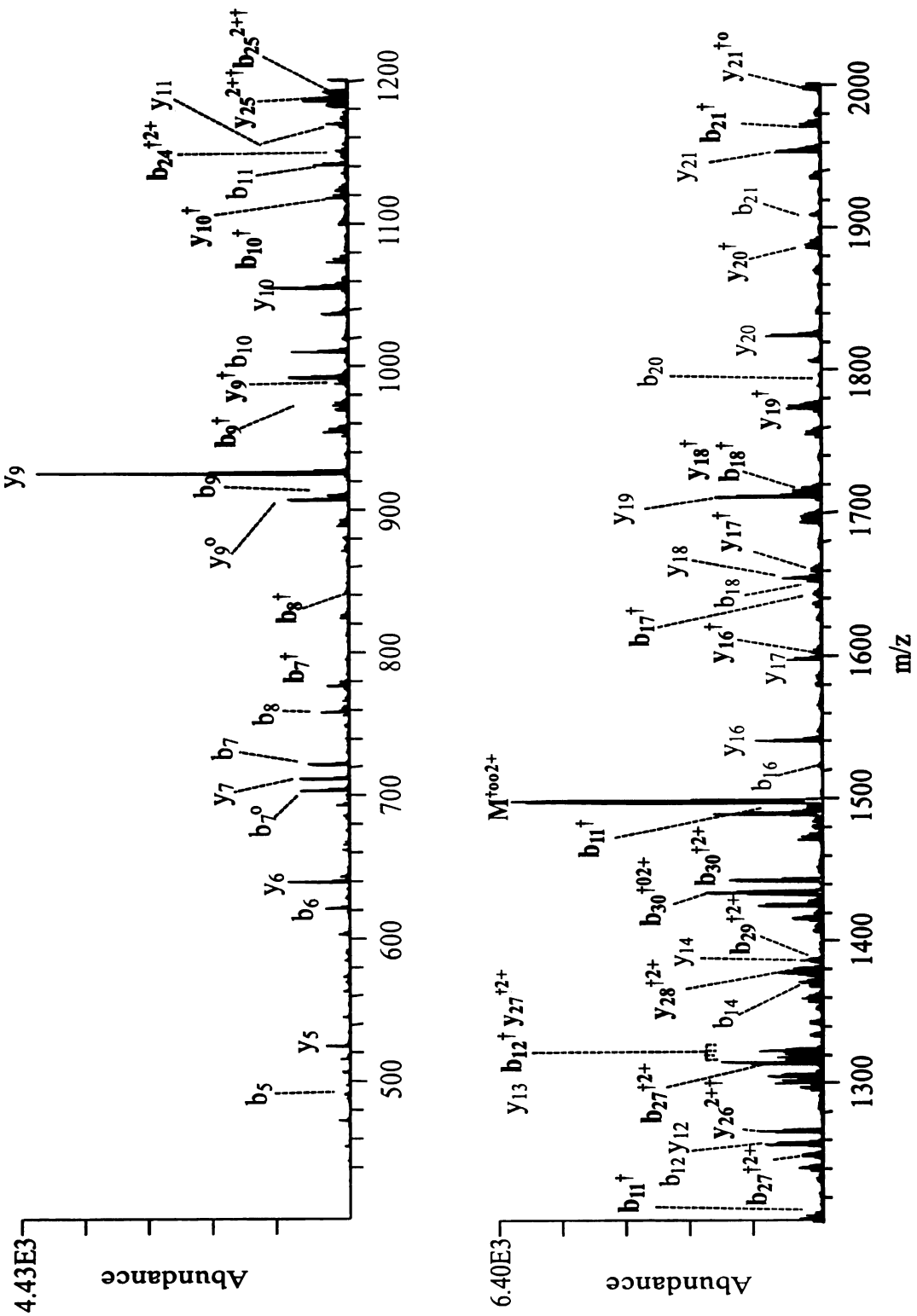

Figure S34: CID MS/MS Spectrum of the $[M+Zn^{2}]^{2+}$ charge state (m/z = 1513.6) of E3A

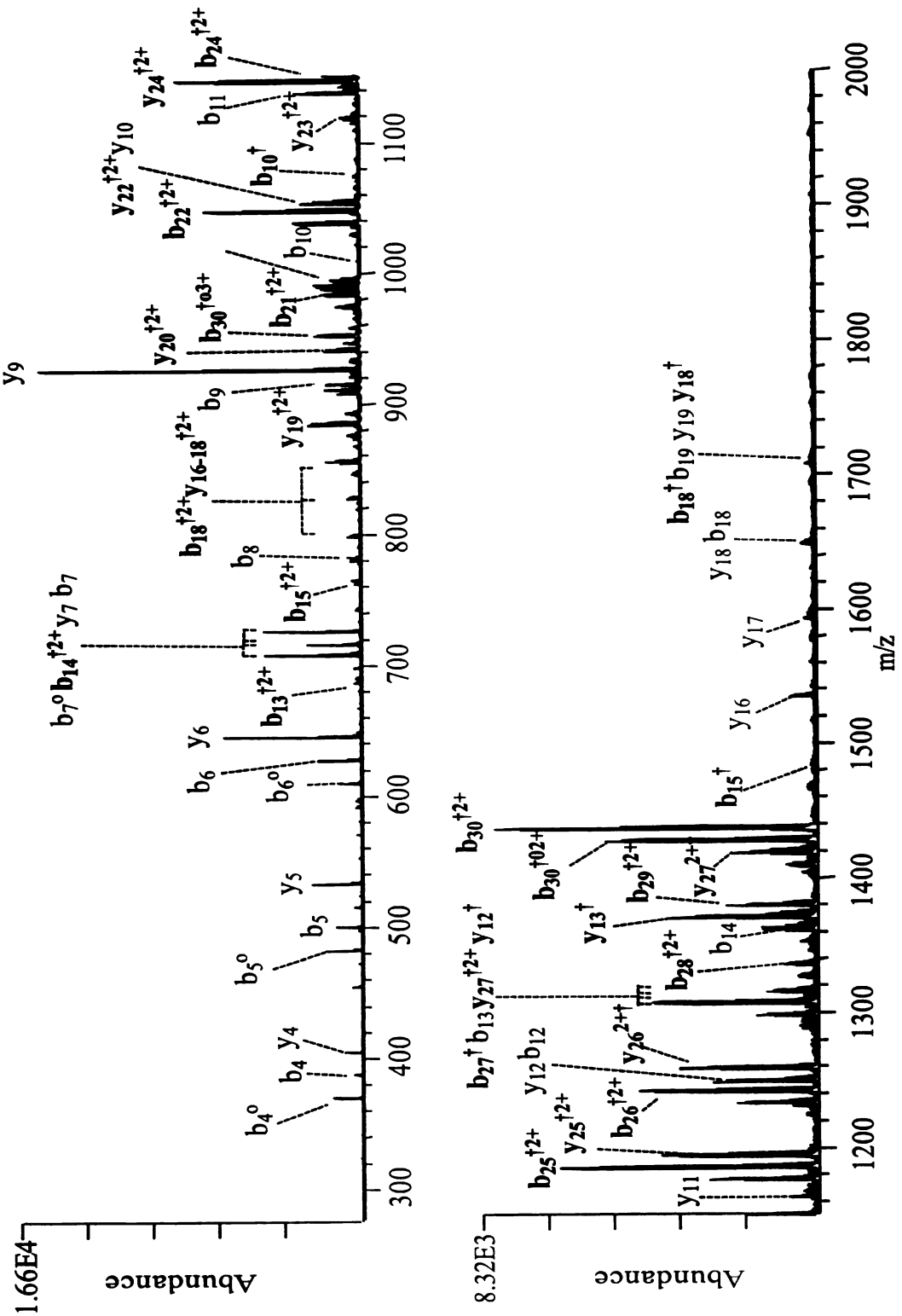

Figure S35: CID MS/MS Spectrum of the $[M+H^{+}+Zn^{2}]^{3+}$ charge state (m/z = 1008.9) of E3A

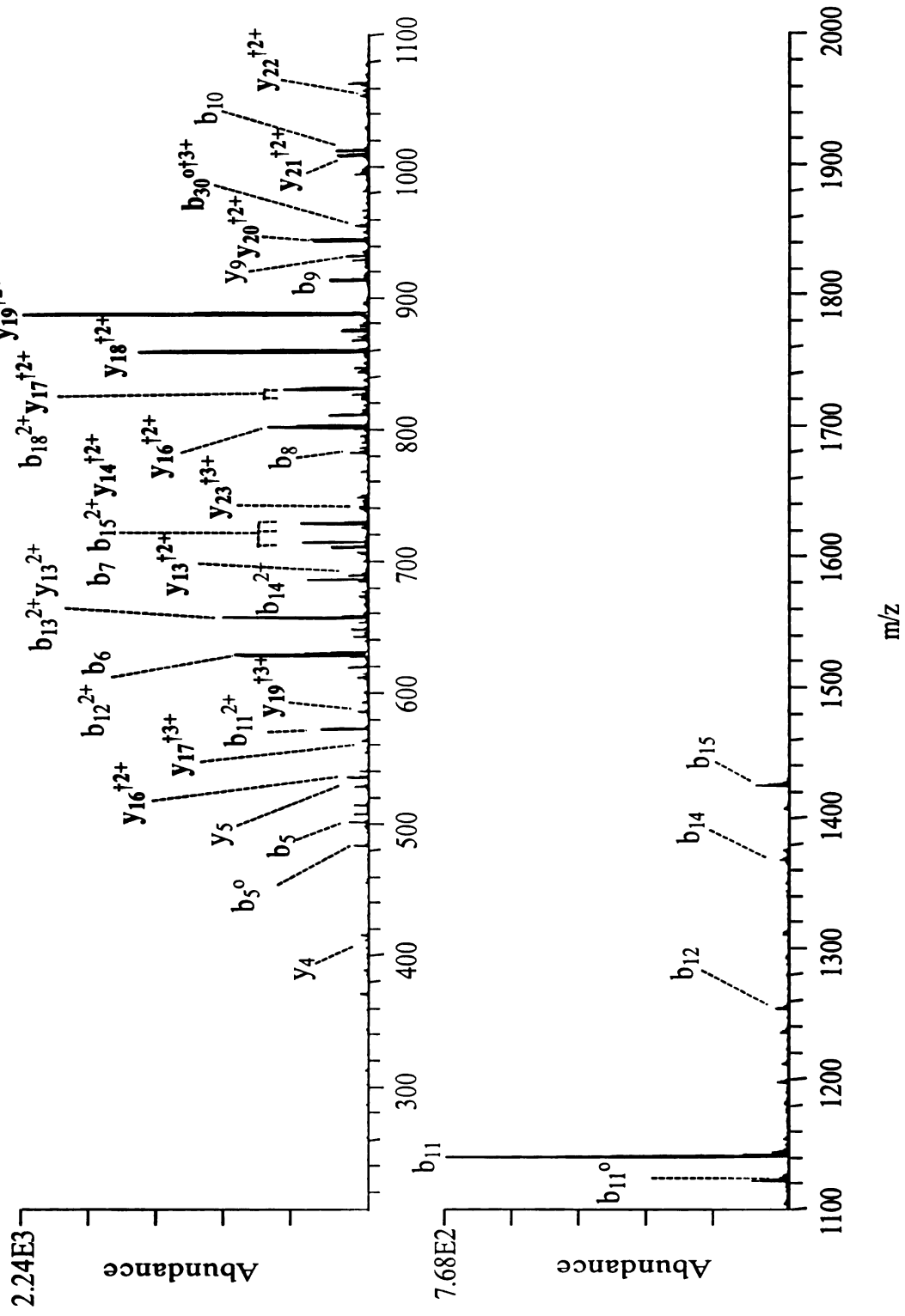

Figure S36: CID MS/MS Spectrum of the $[M+2H^{+}+Zn^{2}]^{4+}$ charge state (m/z = 757.0) of E3A

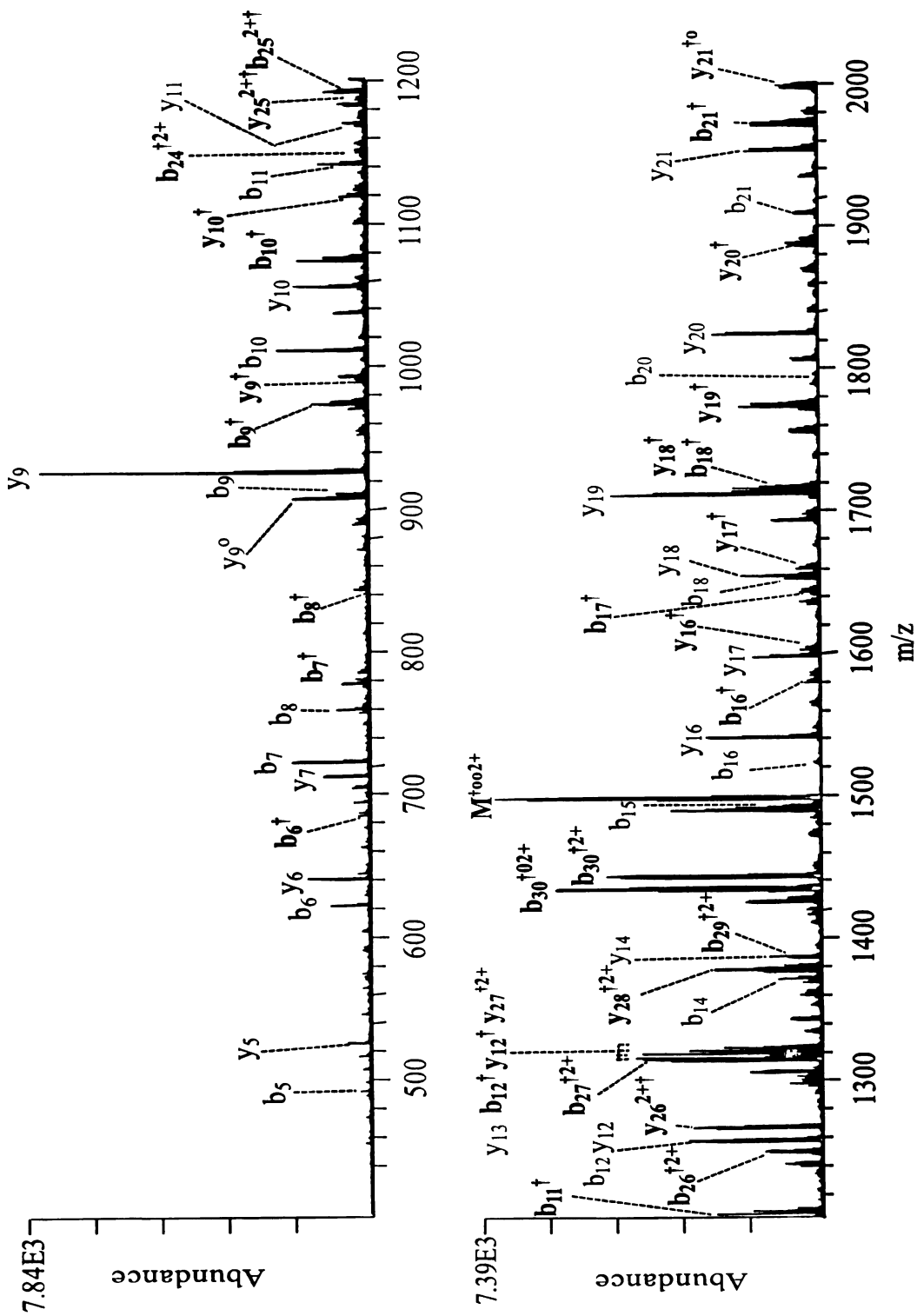

Figure S37: CID MS/MS Spectrum of the $[M+Zn^{2}]^{2+}$ charge state (m/z = 1513.38) of E1A

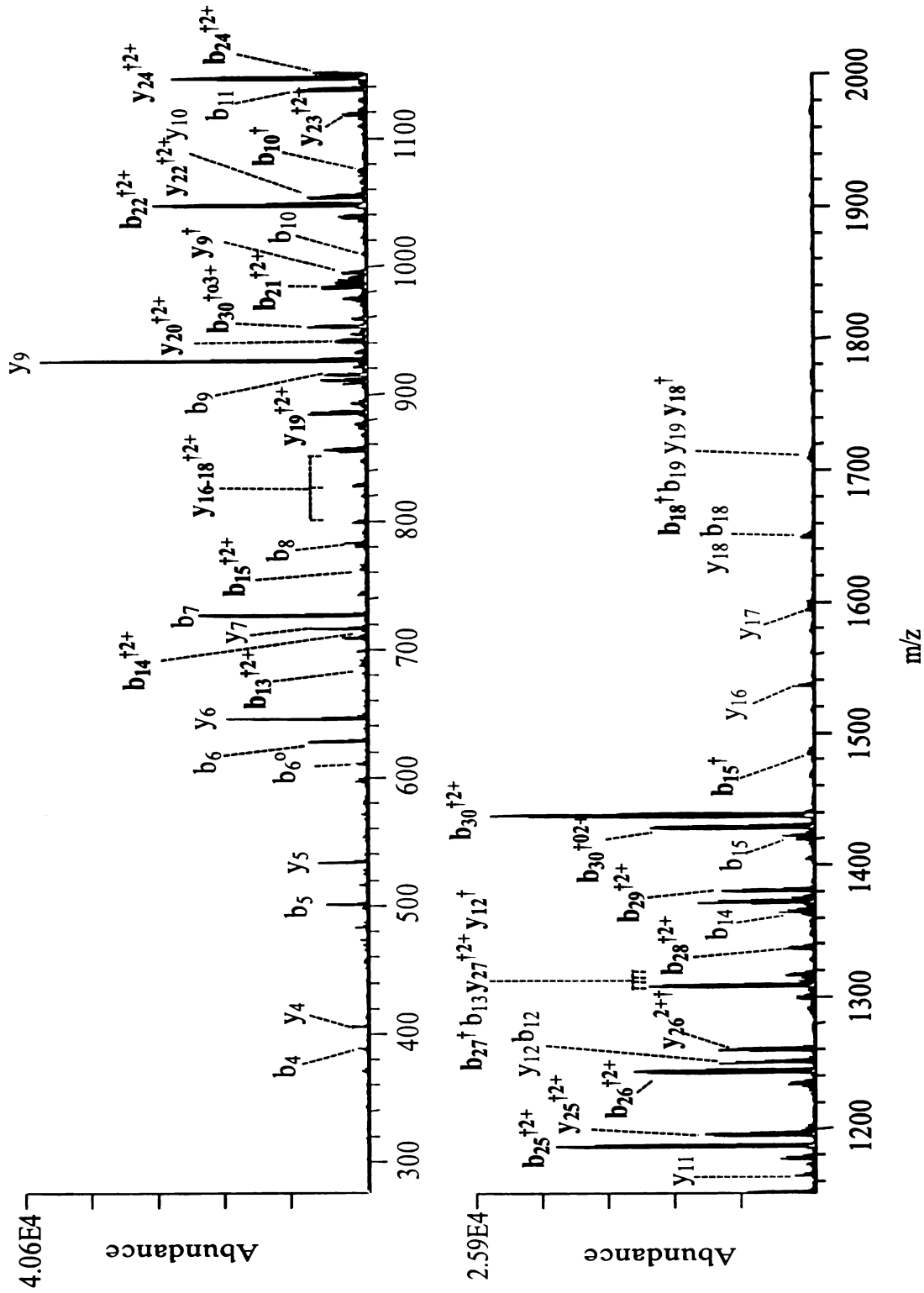

Figure S38: CID MS/MS Spectrum of the $[M+H^{+}+Zn^{2}]^{3+}$ charge state (m/z = 1009.9) of E1A

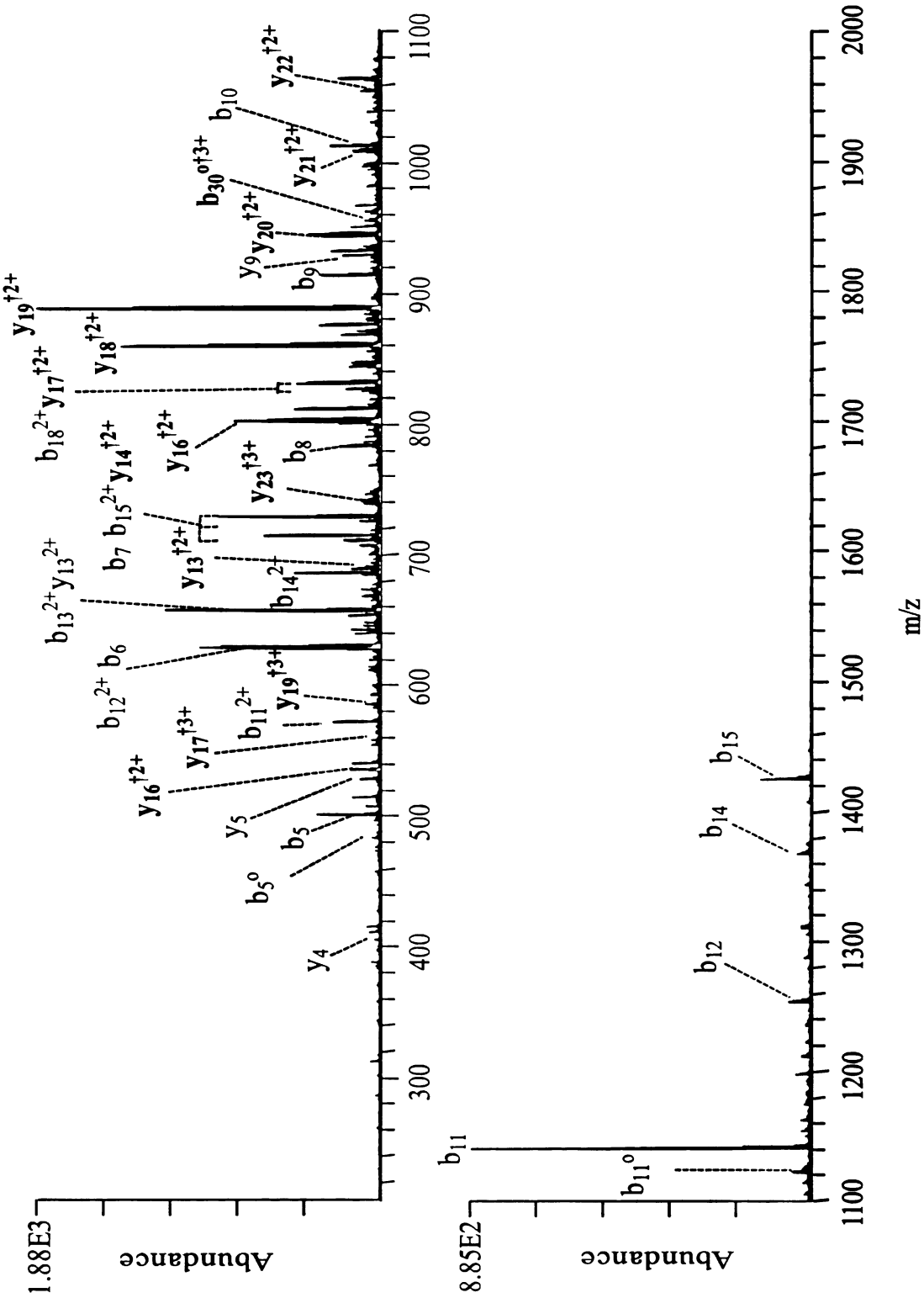

Figure S39: CID MS/MS Spectrum of the $[M+2H^+ + Zn^{2+}]^{4+}$ charge state (m/z = 757.8) of E1A

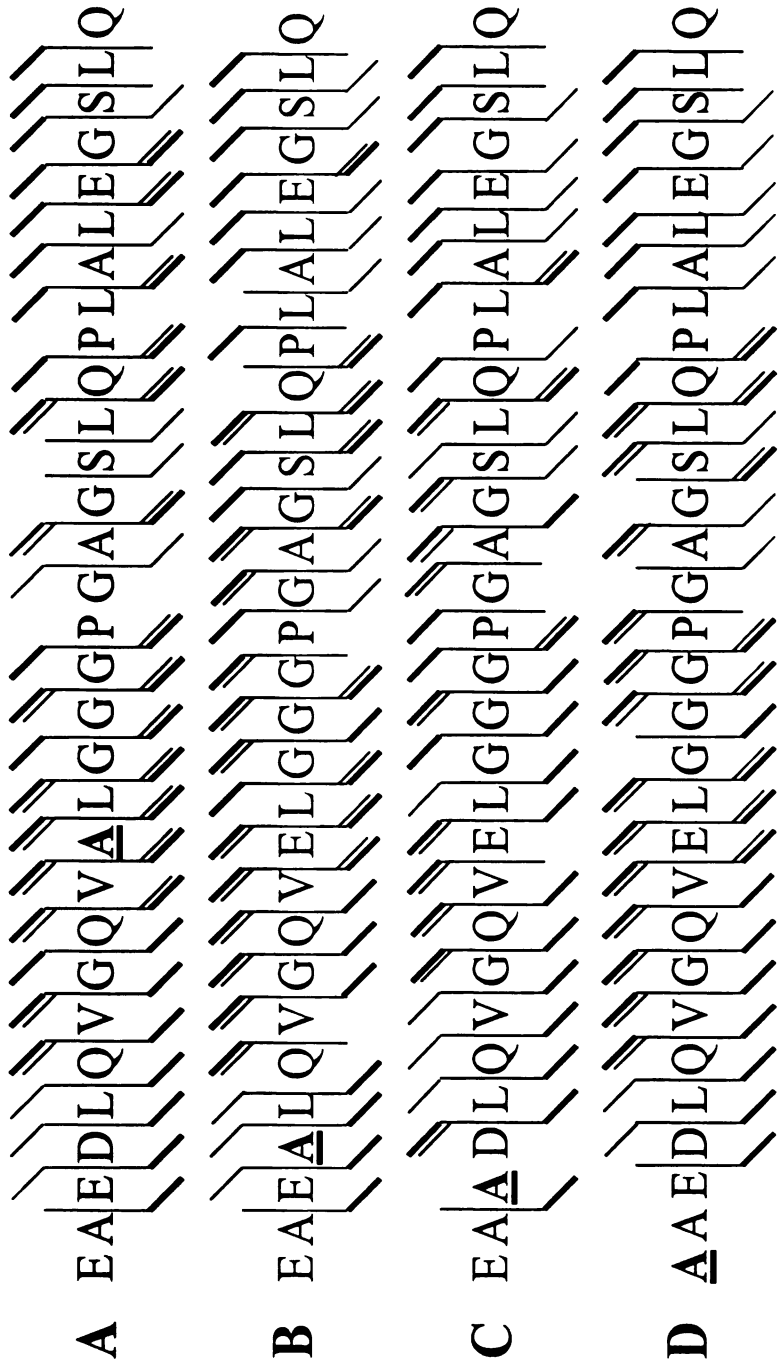

Figure S40: Overall Product ion and sequence coverage summaries obtained from the CID spectra of the $[M+Zn^{2+}]^{2+}$, $[M+H^{+}+Zn^{2+}]^{3+}$, and $[M+2H^{+}+Zn^{2+}]^{4+}$ charge states of A) E11A, B) D4A, C) E3A, D) E1A, mutants of C-peptide. \ indicates an unbound b or y ion, \ indicates only the Zn-bound fragment was found, and \\ indicates that both bound and unbound ions were identified.

REFERENCES

REFERENCES

1. Ahmed, N., Advanced glycation endproducts - role in pathology of diabetic complications. *Diabetes Research and Clinical Practice* **2005,** *67* (1), 3-21.

2. Baynes, J., Role of oxidative stress in development of complications in diabetes. *Diabetes* **1991,** *40* (4), 405-412.

3. Fullerto.Ww; Potter, R.; Low, B. W., Proinsulin - crystallization and preliminary X-Ray diffraction studies. *Proceedings of the National Academy of Sciences of the United States of America* **1970,** *66* (4), 1213-&.

4. Hua, Q. X.; Liu, M.; Hu, S. Q.; Jia, W. H.; Arvan, P.; Weiss, M. A., A conserved histidine in insulin is required for the foldability of human proinsulin - Structure and function of an Ala(B5) analog. *Journal of Biological Chemistry* **2006,** *281* (34), 24889-24899.

5. Klip, A.; Paquet, M., Glucose transport and glucose transporters in muscle and their metabolic regulation. *Diabetes Care* **1990,** *13* (3), 228-243.

6. Baldwin, S. A., Mammalian passive glucose transporters - members of an ubiquitous family of active and passive transport proteins. *Biochimica Et Biophysica Acta* **1993,** *1154* (1), 17-49.

7. Watson, R. T.; Kanzaki, M.; Pessin, J. E., Regulated membrane trafficking of the insulin-responsive glucose transporter 4 in adipocytes. *Endocrine Reviews* **2004,** *25* (2), 177-204.

8. Steinberg, H. O.; Brechtel, G.; Johnson, A.; Fineberg, N.; Baron, A. D., Insulin-Mediated Skeletal-Muscle Vasodilation Is Nitric-Oxide Dependent - a Novel Action of Insulin to Increase Nitric-Oxide Release. *Journal of Clinical Investigation* **1994,** *94* (3), 1172-1179.

9. Kim, F.; Gallis, B.; Corson, M. A., TNF-{alpha} inhibits flow and insulin signaling leading to NO production in aortic endothelial cells. *Am J Physiol Cell Physiol* **2001,** *280* (5), C1057-1065.

10. Traub, O.; Vanbibber, R., Role of nitric-oxide in insulin-dependent diabetes-mellitus related vascular complications. *Western Journal of Medicine* **1995,** *162* (5), 439-445.

11. Arthur S. C. Ko, D. G. S., Jan Markussen, Finn Sundby,, The amino acid sequence of the C-peptide of human proinsulin. *European Journal of Biochemistry* **1971,** *20* (2), 190-199.

12. Dodson, G.; Steiner, D., The role of assembly in insulin's biosynthesis. *Current Opinion in Structural Biology* **1998,** *8* (2), 189-194.

13. Bantle, J. P.; Laine, D. C.; Hoogwerf, B. J.; Goetz, F. C., The potential usefulness of postprandial urine C-peptide measurement in classifying diabetic-patients. *Diabetes Care* **1984,** *7* (2), 202-203.

14. Henriksson, M.; Nordling, E.; Melles, E.; Shafqat, J.; Stahlberg, M.; Ekberg, K.; Persson, B.; Bergman, T.; Wahren, J.; Johansson, J.; Jornvall, H., Separate functional features of proinsulin C-peptide. *Cellular and Molecular Life Sciences* **2005,** *62* (15), 1772-1778.

15. Henriksson, M.; Shafqat, J.; Liepinsh, E.; Tally, M.; Wahren, J.; Jornvall, H.; Johansson, J., Unordered structure of proinsulin C-peptide in aqueous solution and in the presence of lipid vesicles. *Cellular and Molecular Life Sciences* **2000,** *57* (2), 337-342.

16. Kunt, T.; Schneider, S.; Pfutzner, A.; Goitum, K.; Engelbach, M.; Schauf, B.; Beyer, J.; Forst, T., The effect of human proinsulin C-peptide on erythrocyte deformability in patients with Type I diabetes mellitus. *Diabetologia* **1999,** *42* (4), 465-471.

17. Fernqvistforbes, E.; Johansson, B. L.; Wahren, J., C-peptide improves nerve function in type-1 diabetic-patients with autonomic neuropathy. *Diabetologia* **1995,** *38*, A238-A238.

18. Ido, Y.; Vindigni, A.; Chang, K.; Stramm, L.; Chance, R.; Heath, W. F.; DiMarchi, R. D.; DiCera, E.; Williamson, J. R., Prevention of vascular and neural dysfunction in diabetic rats by C-peptide. *Science* **1997,** *277* (5325), 563-566.

19. Johansson, B. L.; Borg, K.; Fernqvist-Forbes, E.; Kernell, A.; Odergren, T.; Wahren, J., Beneficial effects of C-peptide on incipient nephropathy and neuropathy in patients with Type 1 diabetes mellitus. *Diabetic Medicine* **2000,** *17* (3), 181-189.

20. Johansson, B. L.; Borg, K.; FernqvistForbes, E.; Odergren, T.; Remahl, S.; Wahren, J., C-peptide improves autonomic nerve function in IDDM patients. *Diabetologia* **1996,** *39* (6), 687-695.

21. Samnegard, B.; Jacobson, S. H.; Jaremko, G.; Johansson, B. L.; Sjoquist, M., Effects of C-peptide on glomerular and renal size and renal function in diabetic rats. *Kidney International* **2001,** *60* (4), 1258-1265.

22. Forst, T.; Kunt, T., Effects of C-peptide on microvascular blood flow and blood hemorheology. *Experimental Diabesity Research* **2004,** *5* (1), 51-64.

23. Johansson, B. L.; Wahren, J.; Pernow, J., C-peptide increases forearm blood flow in patients with type 1 diabetes via a nitric oxide-dependent mechanism. *American Journal of Physiology-Endocrinology and Metabolism* **2003,** *285* (4), E864-E870.

24. Kitamura, T.; Kimura, K.; Jung, B. D.; Makondo, K.; Okamoto, S.; Canas, X.; Sakane, N.; Yoshida, T.; Saito, M., Proinsulin C-peptide rapidly stimulates mitogen-activated protein kinases in Swiss 3T3 fibroblasts: requirement of protein kinase C, phosphoinositide 3-kinase and pertussis toxin-sensitive G-protein. *Biochemical Journal* **2001,** *355*, 123-129.

25. Kitamura, T.; Kimura, K.; Jung, B. D.; Makondo, K.; Sakane, N.; Yoshida, T.; Saito, M., Proinsulin C-peptide activates cAMP response element-binding proteins through the p38 mitogen-activated protein kinase pathway in mouse lung capillary endothelial cells. *Biochemical Journal* **2002,** *366*, 737-744.

26. Rigler, R.; Pramanik, A.; Jonasson, P.; Kratz, G.; Jansson, O. T.; Nygren, P. A.; Stahl, S.; Ekberg, K.; Johansson, B. L.; Uhlen, S.; Uhlen, M.; Jornvall, H.; Wahren, J., Specific binding of proinsulin C-peptide to human cell membranes. *Proceedings of the National Academy of Sciences of the United States of America* **1999,** *96* (23), 13318-13323.

27. Lindahl, E.; Nyman, U.; Melles, E.; Sigmundsson, K.; Stahlberg, M.; Wahren, J.; Obrink, B.; Shafqat, J.; Joseph, B.; Jornvall, H., Cellular internalization of proinsulin C-peptide. *Cellular and Molecular Life Sciences* **2007,** *64* (4), 479-486.

28. Ekberg, K.; Rigler, R.; Pramanik, A.; Kratz, G.; Johansson, B. L.; Uhlen, M.; Jornvall, H.; Wahren, J., Specific binding of proinsulin C-peptide to human cell membranes. *Diabetologia* **1999,** *42*, A200-A200.

29. Forst, T.; De la Tour, D. D.; Kunt, T.; Pfutzner, A.; Goitom, K.; Pohlmann, T.; Schneider, S.; Johansson, B. L.; Wahren, J.; Lobig, M.; Engelbach, M.; Beyer, J.; Vague, P., Effects of proinsulin C-peptide on nitric oxide, microvascular blood flow and erythrocyte Na+,K+-ATPase activity in diabetes mellitus type I. *Clinical Science* **2000,** *98* (3), 283-290.

30. Ohtomo, Y.; Bergman, T.; Johansson, B. L.; Jornvall, H.; Wahren, J., Differential effects of proinsulin C-peptide fragments on Na+, K+-ATPase activity of renal tubule segments. *Diabetologia* **1998,** *41* (3), 287-291.

31. Pramanik, A.; Ekberg, K.; Zhong, Z.; Shafqat, J.; Henriksson, M.; Jansson, O.; Tibell, A.; Tally, M.; Wahren, J.; Jornvall, H.; Rigler, R.; Johnansson, J., C-peptide binding to human cell membranes: Importance of Glu27. *Biochemical and Biophysical Research Communications* **2001,** *284* (1), 94-98.

32. Koc, B.; Erten, V.; Yilmaz, M. I.; Sonmez, A.; Kocar, I. H., The relationship between red blood cell Na/K-ATPase activities and diabetic complications in patients with type 2 diabetes mellitus. *Endocrine* **2003,** *21* (3), 273-278.

33. Mares-Guia, T. R.; Maigret, B.; Martins, N. F.; Maia, A. L. T.; Vilela, L.; Ramos, C. H. I.; Neto, L. J.; Juliano, M. A.; dos Mares-Guia, M. L.; Santoro, M. M., Molecular dynamics and circular dichroism studies of human and rat C-peptides. *Journal of Molecular Graphics and Modelling* **2006,** *25* (4), 532-542.

34. Valko, M.; Rhodes, C. J.; Moncol, J.; Izakovic, M.; Mazur, M., Free radicals, metals and antioxidants in oxidative stress-induced cancer. *Chemico-Biological Interactions* **2006,** *160* (1), 1-40.

35. Dymock, I. W.; Cassar, J.; Pyke, D. A.; Oakley, W. G.; Williams, R., Observations on the pathogenesis, complications and treatment of diabetes in 115 cases of haemochromatosis. *The American Journal of Medicine* **1972,** *52* (2), 203-210.

36. Fernandez-Real, J. M.; Lopez-Bermejo, A.; Ricart, W., Iron stores, blood donation, and insulin sensitivity and secretion. *Clinical Chemistry* **2005,** *51* (7), 1201-1205.

37. Schafer, A. I.; Cheron, R. G.; Dluhy, R.; Cooper, B.; Gleason, R. E.; Soeldner, J. S.; Bunn, H. F., Clinical Consequences of Acquired Transfusional Iron Overload in Adults. *New England Journal of Medicine* **1981,** *304* (6), 319-324.

38. Mertz, W.; Roginski, E. E.; Schwarz, K., Effect of trivalent chromium complexes on glucose uptake by epididymal fat tissue of rats. *Journal of Biological Chemistry* **1961,** *236* (2), 318-&.

39. Schwarz, K.; Mertz, W., A Glucose tolerance factor and its differentiation from factor-3. *Archives of Biochemistry and Biophysics* **1957,** *72* (2), 515-518.

40. Mertz, W.; Schwarz, K., Relation of glucose tolerance factor to impaired intravenous glucose tolerance of rats on stock diets. *American Journal of Physiology* **1959,** *196* (3), 614-618.

41. Yamamoto, A.; Wada, O.; Ono, T., A Low-molecular-weight, chromium-binding substance in mammals. *Toxicology and Applied Pharmacology* **1981,** *59* (3), 515-523.

42. Yamamoto, A.; Wada, O.; Ono, T., Isolation of a biologically-active low-molecular-mass chromium compound from rabbit liver. *European Journal of Biochemistry* **1987,** *165* (3), 627-631.

43. Davis, C. M.; Vincent, J. B., Chromium in carbohydrate and lipid metabolism. *Journal of Biological Inorganic Chemistry* **1997,** *2* (6), 675-679.

44. Emdin, S. O.; Dodson, G. G.; Cutfield, J. M.; Cutfield, S. M., Role of zinc in insulin-biosynthesis - some possible zinc-insulin interactions in the pancreatic B-cell. *Diabetologia* **1980,** *19* (3), 174-182.

45. Chimienti, F.; Favier, A.; Seve, M., ZnT-8, a pancreatic beta-cell-specific zinc transporter. *Biometals* **2005,** *18* (4), 313-317.

46. Cunningham, J. J.; Fu, A. Z.; Mearkle, P. L.; Brown, R. G., Hyperzincuria in individuals with insulin-dependent diabetes-mellitus - concurrent zinc status and

the effect of high-dose zinc supplementation. *Metabolism-Clinical and Experimental* **1994,** *43* (12), 1558-1562.

47. Meyer, J. A.; Froelich, J. M.; Reid, G. E.; Karunarathne, W. K. A.; Spence, D. M., Metal-activated C-peptide facilitates glucose clearance and the release of a nitric oxide stimulus via the GLUT1 transporter. *Diabetologia* **2008,** *51* (1), 175-182.

48. Jennifer A. Meyer, W. S., Anders A. F. Sima, Zachary Keltner, Gavin E. Reid, David Daleke and Dana M. Spence, hyperglycemia-induced phosphatidylserine exernalization is associated with zinc-activated C-peptide resistance to the type 2 diabetic erythrocyte (manuscript in preparation).

49. Teesch, L. M.; Adams, J., Fragmentations of gas-phase complexes between alkali-mtal ions and peptides - metal-ion binding to carbonyl oxygens and other neutral functional-groups. *Journal of the American Chemical Society* **1991,** *113* (3), 812-820.

50. Teesch, L. M.; Orlando, R. C.; Adams, J., Location of the alkali-metal ion in gas-phase peptide complexes. *Journal of the American Chemical Society* **1991,** *113* (10), 3668-3675.

51. Hu, P. F.; Gross, M. L., Strong-interactions of anionic peptides and alkaline-earth metal-ions - metal-ion-bound peptides in the gas-phase. *Journal of the American Chemical Society* **1992,** *114* (23), 9153-9160.

52. Hu, P. F.; Gross, M. L., Strong-interactions of anionic peptides and alkaline-earth metal-ions - bis(peptide) complexes in the gas-phase. *Journal of the American Chemical Society* **1992,** *114* (23), 9161-9169.

53. Nemirovskiy, O. V.; Gross, M. L., Determination of calcium binding sites in gas-phase small peptides by tandem mass spectrometry. *Journal of the American Society for Mass Spectrometry* **1998,** *9* (10), 1020-1028.

54. Nemirovskiy, O. V.; Gross, M. L., Gas phase studies of the interactions of Fe2+ with cysteine-containing peptides. *Journal of the American Society for Mass Spectrometry* **1998,** *9* (12), 1285-1292.

55. Grese, R. P.; Cerny, R. L.; Gross, M. L., Metal-ion peptide interactions in the gas-phase - a tandem mass-spectrometry study of alkali-metal cationized peptides. *Journal of the American Chemical Society* **1989,** *111* (8), 2835-2842.

56. Yu, X. L.; Wojciechowski, M.; Fenselau, C., assessment of metals in reconstituted metallothioneins by electrospray mass-spectrometry. *Analytical Chemistry* **1993,** *65* (10), 1355-1359.

57. Loo, J. A.; Hu, P. F.; Smith, R. D., Interaction of angiotensin peptides and zinc metal-ions probed by electrospray-ionization mass-spectrometry. *Journal of the American Society for Mass Spectrometry* **1994,** *5* (11), 959-965.

58. Zirah, S.; Rebuffat, S.; Kozin, S. A.; Debey, P.; Fournier, F.; Lesage, D.; Tabet, J. C., Zinc binding properties of the amyloid fragment A beta(1-16) studied by electrospray-ionization mass spectrometry. *International Journal of Mass Spectrometry* **2003,** *228* (2-3), 999-1016.

59. Pu, D.; Vincent, J. B.; Cassady, C. J., The effects of chromium(III) coordination on the dissociation of acidic peptides. *Journal of Mass Spectrometry* **2008,** *43* **(6),** 773-781.

60. Roepstorff, P.; Fohlman, J., Proposal for a common nomenclature for sequence ions in mass-spectra of peptides. *Biomedical Mass Spectrometry* **1984,** *11* **(11),** 601-601.

61. Biemann, K.; Papayannopoulos, I. A., Amino-acid sequencing of proteins. *Accounts of Chemical Research* **1994,** *27* (11), 370-378.

62. Jernigan, R.; Raghunathan, G.; Bahar, I., Characterization of interactions and metal-ion binding-sites in proteins. *Current Opinion in Structural Biology* **1994,** *4* (2), 256-263.

63. Kaiser, E.; Colescot.Rl; Bossinge.Cd; Cook, P. I., Color Test for detection of free terminal amino groups in solid-phase synthesis of peptides. *Analytical Biochemistry* **1970,** *34* (2), 595-&.

64. Fenn, J.; Mann, M.; Meng, C.; Wong, S.; Whitehouse, C., Electrospray ionization for mass spectrometry of large biomolecules. *Science* **1989,** *246* (4926), 64-71.

65. Kebarle, P., A brief overview of the present status of the mechanisms involved in electrospray mass spectrometry. *J Mass Spectrom* **2000,** *35* (7), 804-17.

66. Gomez, A.; Tang, K., Charge and fission of droplets in electrostatic sprays. *Physics of Fluids* **1994,** *6* (1), 404-414.

67. Iribarne, J. V.; Thomson, B. A., Evaporation of small ions from charged droplets. *Journal of Chemical Physics* **1976,** *64* (6), 2287-2294.

68. Thomson, B. A.; Iribarne, J. V., Field-induced ion evaporation from liquid surfaces at atmospheric-pressure. *Journal of Chemical Physics* **1979,** *71* **(11),** 4451-4463.

69. Karas, M.; Bachmann, D.; Bahr, U.; Hillenkamp, F., Matrix-assisted ultraviolet-laser desorption of nonvolatile compounds. *International Journal of Mass Spectrometry and Ion Processes* **1987,** *78*, 53-68.

70. Karas, M.; Gluckmann, M.; Schafer, J., Ionization in matrix-assisted laser desorption/ionization: singly charged molecular ions are the lucky survivors. *Journal of Mass Spectrometry* **2000,** *35* (1), 1-12.

71. Zenobi, R.; Knochenmuss, R., Ion formation in MALDI mass spectrometry. *Mass Spectrometry Reviews* **1998,** *17* (5), 337-366.

72. March, R. E., An introduction to quadrupole ion trap mass spectrometry. *Journal of Mass Spectrometry* **1997,** *32* (4), 351-369.

73. de Hoffman, E. D. S., V., *Mass Spectrometry Principles and Applications*. John Wiley and Sons: New York, 1992.

74. Hager, J. W., A new linear ion trap mass spectrometer. *Rapid Communications in Mass Spectrometry* **2002,** *16* (6), 512-526.

75. Schwartz, J. C.; Senko, M. W.; Syka, J. E. P., A two-dimensional quadrupole ion trap mass spectrometer. *Journal of the American Society for Mass Spectrometry* **2002,** *13* (6), 659-669.

76. Reid, G. E.; McLuckey, S. A., 'Top down' protein characterization via tandem mass spectrometry. *Journal of Mass Spectrometry* **2002,** *37* (7), 663-675.

77. Scherperel, G.; Reid, G. E., Emerging methods in proteomics: top-down protein characterization by multistage tandem mass spectrometry. *Analyst* 2007, *132* (6), 500-506.

78. Reid, G. E.; Wu, J.; Chrisman, P. A.; Wells, J. M.; McLuckey, S. A., Charge-state-dependent sequence analysis of protonated ubiquitin ions via ion trap tandem mass spectrometry. *Analytical Chemistry* **2001,** *73* (14), 3274-3281.

79. Scherperel, G.; Yan, H. G.; Wang, Y.; Reid, G. E., 'Top-down' characterization of site-directed mutagenesis products of Staphylococcus aureus dihydroneopterin aldolase by multistage tandem mass spectrometry in a linear quadrupole ion trap. *Analyst* **2006,** *131* (2), 291-302.

80. Dongre, A. R.; Jones, J. L.; Somogyi, A.; Wysocki, V. H., Influence of peptide composition, gas-phase basicity, and chemical modification on fragmentation efficiency: Evidence for the mobile proton model. *Journal of the American Chemical Society* **1996,** *118* (35), 8365-8374.

81. Kapp, E. A.; Schutz, F.; Reid, G. E.; Eddes, J. S.; Moritz, R. L.; O'Hair, R. A. J.; Speed, T. P.; Simpson, R. J., Mining a tandem mass spectrometry database to determine the trends and global factors influencing peptide fragmentation. *Analytical Chemistry* **2003,** *75* (22), 6251-6264.

82. Paizs, B.; Suhai, S., Fragmentation pathways of protonated peptides. *Mass Spectrometry Reviews* **2005,** *24* (4), 508-548.

83. Dudev, T.; Lim, C., Tetrahedral vs octahedral zinc complexes with ligands of biological interest: A DFT/CDM study. *Journal of the American Chemical Society* **2000,** *122* (45), 11146-11153.